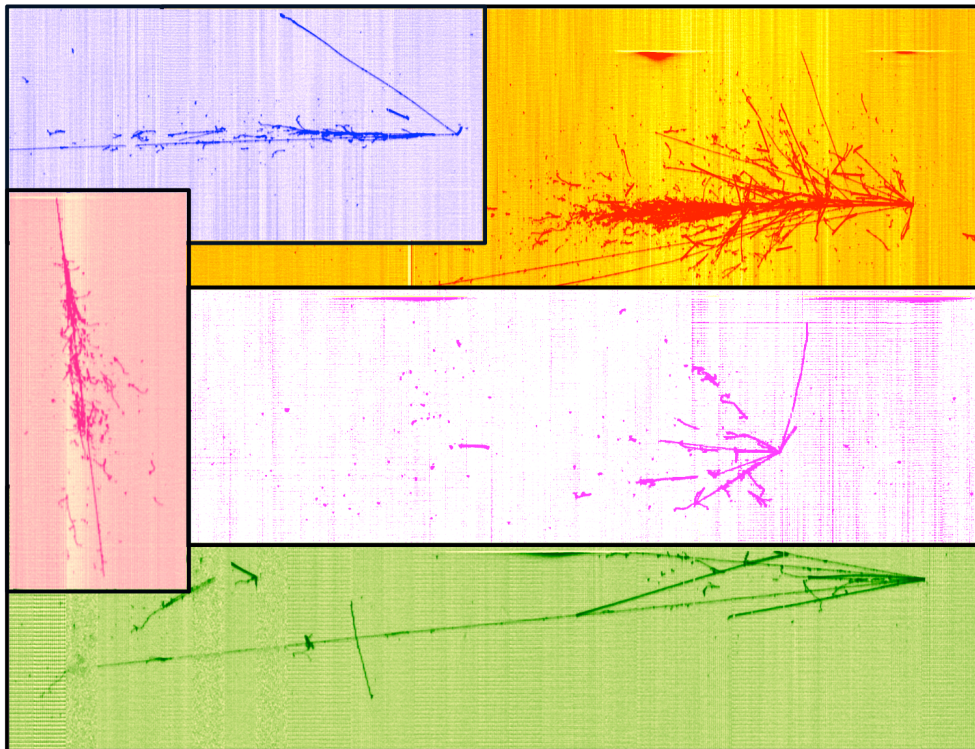


UNIVERSITÀ DEGLI STUDI DI PAVIA
DOTTORATO DI RICERCA IN FISICA – XXVIII CICLO

Studies and tests for
the new light collection system
of the ICARUS T600 detector

Andrea Falcone



Tesi per il conseguimento del titolo



Università
degli Studi
di Pavia



Istituto
Nazionale di
Fisica Nucleare

DOTTORATO DI RICERCA IN FISICA – XXVIII CICLO

Studies and tests for
the new light collection system
of the ICARUS T600 detector

Andrea Falcone

Submitted to the Graduate School of Physics in partial fulfilment of the
requirements for the degree of

DOTTORE DI RICERCA IN FISICA
DOCTOR OF PHILOSOPHY IN PHYSICS

at the

University of Pavia

Supervisors: Prof. Alessandro Menegolli (Università di Pavia– INFN Pavia)
Dott. Claudio Silverio Montanari (INFN Pavia)

Referees: Prof. Francesco Terranova (Università di Milano Bicocca - Italia)
Prof. Jon Urheim (Indiana University - USA)

Cover: *Events collected in the ICARUS T600 detector during the LNGS run.*

Studies and tests for the new light collection system of the ICARUS T600 detector

Andrea Falcone

PhD thesis - University of Pavia

Pavia, Italy, November 2015

ISBN: 978-88-95767-89-5

Contents

Table of contents	iv
List of Figures	v
Introduction and keywords	1
1 Neutrino oscillations	3
1.1 Neutrino oscillations theory	4
1.2 Hint for sterile neutrino	7
1.2.1 Short baseline experiment	7
1.2.2 Gallium experiment	10
1.2.3 Reactor experiment	11
1.2.4 Requirements for future experiments	14
2 ICARUS at Laboratori Nazionali del Gran Sasso	15
2.1 Configuration of the ICARUS T600 detector	16
2.1.1 Light collection system	19
2.1.2 PMT system performances	22
2.2 Events analysis	24
2.2.1 Search for LSND anomaly	27
2.2.2 Antineutrino analysis	30
3 Short Baseline Neutrino program	35
3.1 The Booster Neutrino Beam	36
3.2 LAr1-ND	37
3.3 MicroBooNE	37
3.4 ICARUS T600 at FNAL	38
3.4.1 TPC modifications	40
3.4.2 New electronics	41
3.4.3 Trigger and DAQ	41
3.4.4 New cryogenic and purification systems	42

4	New light collection system: Monte Carlo study	43
4.1	Monte Carlo simulation	44
4.2	Event position reconstruction	46
4.3	Trigger definition	51
4.4	Event identification	52
5	New light collection system: hardware activity	61
5.1	Tests on PMTs	62
5.1.1	Hamamatsu R5912 Mod	65
5.1.2	Hamamatsu R5912 - 02 Mod	72
5.1.3	ETL 9357 KFLB	77
5.1.4	PMT model final choice	79
5.2	PMTs induced noise	80
5.3	PMT acquisition and calibration system	81
6	ICARUS T600 with magnetic field	87
6.1	Magnetic field simulation	87
6.2	Tests on SiPMs	91
6.2.1	Breakdown voltage	94
6.2.2	Quenching resistance	95
6.2.3	Over-voltage dependence	96
6.2.4	Dark counts rate	96
6.2.5	Signal shape	97
6.2.6	SiPM response to VUV light	97
	Bibliography	103

List of Figures

1.1	Plot of the experimental results obtained in the neutrino oscillation sector till July 2015 [12].	8
1.2	The $(\sin^2 2\theta, \Delta m^2)$ oscillation parameter fit for the entire LSND data sample, $20 < E_{\bar{\nu}} < 200$ MeV [17].	9
1.3	The excess of ν_e (up) and $\bar{\nu}_e$ (down) candidate events observed by MiniBooNE in neutrino and antineutrino mode respectively. .	10
1.4	The MiniBooNE oscillation allowed region in antineutrino mode.	11
1.5	Weighted average (with correlations) of 19 measurements of reactor neutrino experiments operating at short baselines.	12
1.6	Allowed regions in the $\sin^2(2\theta_{e\mu}) - \Delta m_{41}^2$, $\sin^2(2\theta_{ee}) - \Delta m_{41}^2$ and $\sin^2(2\theta_{\mu\mu}) - \Delta m_{41}^2$ planes obtained in the 3+1-PrGLO global fit of short-baseline neutrino oscillation data compared with the 3σ allowed regions obtained from $\nu_\mu \rightarrow \nu_e$ short-baseline appearance data (APP) and the 3σ constraints obtained from ν_e short-baseline disappearance data (ν_e DIS), ν_μ short-baseline disappearance data (ν_μ DIS) and the combined short-baseline disappearance data (DIS). The best-fit points of the PrGLO and APP fits are indicated by crosses [29].	13
2.1	Left: schematic view of the whole ICARUS-T600 plant at LNGS. Right-top: photo of the detector installation. Right-bottom: details of the cryo-cooler plant.	17
2.2	Illustration of the ICARUS T600 working principle: a charged particle ionization path in LAr and its geometrical reconstruction.	18
2.3	Left: internal view of one of the West Module TPC, with a few PMTs clearly visible together with their sustaining structure. Right: PMTs deployment in the two ICARUS T600 cryostats. PMT coordinates in cm are related to the reference frame used in Hall B.	21
2.4	PMT electronics layout.	22
2.5	Example of recorded PMT waveform after integration of fast and slow light components.	23

2.6	Single PMT pulse-heights in the Right chamber of the West module as a function of the longitudinal distance of vertical tracks from the PMT when the cosmic muon is crossing the Right (left) and the Left (right) TPC [38].	23
2.7	PMT sum signal efficiencies of each TPC chamber in the West (left) and East (right) modules, as a function of the energy deposited by cosmic muons (top), the track distance from the PMT wall (center) and the track longitudinal position (bottom). The represented error bars account only for the statistical error [38].	25
2.8	Typical Monte Carlo generated ν_e event with $E_e = 11$ GeV and $p_T = 1.0$ GeV/c.	29
2.9	Experimental picture of an event with a clearly identified electron signature. Event has a total energy of 11.5 ± 1.8 GeV, and a transverse electron momentum of 1.8 ± 0.4 GeV/c. The single electron shower in the transverse plane is clearly opposite to the remaining of the event.	31
2.10	Display of the actual dE/dx along individual wires of the electron shower shown in Fig. 2.9, in the region ≥ 4.5 cm from primary vertex, where the track is well separated from other tracks and heavily ionizing nuclear prongs. As a reference, the expected dE/dx distribution for single and double minimum ionizing tracks are displayed and the dE/dx evolution from single ionizing electron to shower is shown.	32
2.11	Two dimensional plot with Δm^2 as a function of $\sin^2(2\theta)$ for the main experiments sensitive to the $\nu_\mu \rightarrow \nu_e$ anomalies and for the present ICARUS result (continuous red lines). The ICARUS limit on the $\nu_\mu \rightarrow \nu_e$ oscillation probability are $\langle P(\nu_\mu \rightarrow \nu_e) \rangle \leq 3.92 \times 10^{-3}$ and $\langle P(\nu_\mu \rightarrow \nu_e) \rangle \leq 7.83 \times 10^{-3}$ at 90% and 99% CL.	33
2.12	Two dimensional plot with Δm^2 as a function of $\sin^2(2\theta)$ for the main experiments sensitive to the $\bar{\nu}_\mu \rightarrow \bar{\nu}_e$ anomalies and for the present ICARUS result (continuous red lines). The ICARUS limit on the $\bar{\nu}_\mu \rightarrow \bar{\nu}_e$ oscillation probability is $\langle P(\bar{\nu}_\mu \rightarrow \bar{\nu}_e) \rangle \leq 0.32$ at 90% CL	34
3.1	Map of the Fermilab neutrino beam line area showing the axis of the BNB (yellow dashed line) and approximate locations of the SBN detectors at 110 m, 470 m and 600 m. The pink line indicates the axis of the NuMI neutrino beam for reference. . . .	36
3.2	(Left) The LAr1-ND detector building concept. The neutrino beam center is indicated by the orange dashed line and enters from the left. (Right) The LAr1-ND TPC conceptual design. . .	38

LIST OF FIGURES

3.3	The MicroBooNE detector. The high-voltage feedthrough enters on the right and supplies the voltage for the cathode plane. One side of the field cage can be seen on the face of the cut-away (supported by the X braces). The sense and induction wires are on the right, and behind them is the support structure for the PMT array.	39
3.4	The ICARUS-T600 detector building concept (left building). The neutrino beam center is indicated by the orange dashed line and enters from the right. The existing MiniBooNE (right building) and MicroBooNE (central building) buildings are also shown.	40
3.5	Scheme of ICARUS-T600 detector building. The 3 m concrete cup is enlightened in green. The neutrino beam center is indicated by the orange dashed line and enters from the left.	41
4.1	Drawings that show the different PMT layouts behind the wire planes. PMTs are depicted as dark circles.	47
4.2	Photo-edited image that shows the possibility to install till 90 8"-PMTs on the existing T600 mechanical structure, by adding further PMTs in addition to the existing ones (circled).	48
4.3	Evaluation of the precision on the localization of the correct position, along the beam direction z , for e.m. showers for the different PMT layouts. For the configuration C also the result obtained using only the PMTs with signal above 10 phe is shown (C2). The FWHM and the percentage of events localized with an error greater than 10, 20, 30 60 and 90 cm are indicated.	49
4.4	Actual position of the events localized with an error greater than 30 cm in the z direction.	50
4.5	Evaluation of the precision on the localization of the correct position, along the beam direction z , for e.m. showers obtained with the fake PMTs algorithm. The FWHM and the percentage of events localized with an error greater than 10, 20, 30 60 and 90 cm are indicated.	50
4.6	Evaluation of the precision on the localization of the correct position for e.m. showers, along the vertical direction x , with (left) and without (right) the PMTs weight correction. The FWHM and the percentage of events localized with an error greater than 10, 20, 30 60 and 90 cm are indicated.	51
4.7	Evaluation of the precision on the localization of the correct position, along the beam direction z , for e.m. showers obtained using only the fast component of the light. The FWHM and the percentage of events localized with an error greater than 10, 20, 30 60 and 90 cm are indicated.	52

4.8	Evaluation of the precision on the localization of the correct position, along the beam direction z , for e.m. showers with PMTs saturation at 400 phe (left) and 40 phe (right). The FWHM and the percentage of events localized with an error greater than 10, 20, 30 60 and 90 cm are indicated.	53
4.9	Evaluation of the precision on the localization of the correct position, along the beam direction z , with the 90 8"-PMTs layout, for muons, using all PMT signals (left) or only the PMTs with signal above 10 phe (right). The FWHM and the percentage of events localized with an error greater than 10, 20, 30 60 and 90 cm are indicated.	53
4.10	Residual ^{39}Ar rate as a function of the adopted phe threshold and PMT majority.	54
4.11	(Top) PMT activated from 100 MeV e.m. showers in proximity of the cathode, as a function of the adopted phe threshold, for the different PMT layouts. (Bottom) Detection efficiency for 100 MeV e.m. showers in proximity of the cathode, as a function of the phe threshold and PMT majority.	55
4.12	Light collected (left) and photons arrival time (right) patterns from a 200 MeV e.m. shower occurring in the centre of the TPC active volume (bottom) and for a vertical crossing muon again in the centre of the detector(top).	56
4.13	Schematic structure of a multilayer perceptron.	58
4.14	Subdivision of the PMT plane into 8 sections. Each section has the same PMT geometrical disposition. Red lines represent the centre of each section.	58
4.15	Result of the neural network trained with muons as signal. Setting 0.5 as threshold value, bad identified muons are $\sim 4\%$, while misidentified background is $\sim 7\%$	59
4.16	Result of the neural network trained with e.m. showers as signal. Setting 0.5 as threshold value, bad identified e.m. showers are $\sim 11\%$, while misidentified background is $\sim 19\%$	59
4.17	Result of the neural network trained with $\nu_\mu\text{CC}$ interactions as signal. Setting 0.5 as threshold value, bad identified $\nu_\mu\text{CC}$ are $\sim 19\%$, while misidentified background is $\sim 23\%$	59
5.1	Experimental setup used for measurements at cryogenic temperature.	64
5.2	Experimental setup for the evaluation of the response of PMTs to the VUV light.	64
5.3	Voltage divider used to test the Hamamatsu R5912 Mod.	66
5.4	Gain trends for Hamamatsu R5912 Mod (left up), R5912-02 Mod (right up) and ETL 9357 KFLB (down) at room and cryogenic temperature.	67
5.5	Support system used for photocathode uniformity measurements.	68

LIST OF FIGURES

5.6	Relative response as a function of the distance from the centre of the window, along different diameters, for Hamamatsu R5912 Mod (up) and ETL 9357 KFLB (down). Several measurements were performed for each position: error bars represent the statistical errors.	69
5.7	Relative response as a function of the orientation with respect to the Earth's magnetic field for Hamamatsu R5912 Mod (left up), R5912-02 Mod (right up) and ETL 9357 KFLB (down). The Hamamatsu PMTs were illuminated at the centre of the window, while ETL both at the centre of the window and 10 cm far from it.	70
5.8	Electron transit time of Hamamatsu R5912 Mod (left up), R5912-02 Mod (right up) and ETL 9357 KFLB (down), as a function of the orientation with respect to the Earth's magnetic field.	71
5.9	System for measurements of PMTs linearity. The acquisition system for the voltage mode measurements is also sketched. . .	72
5.10	Linearity of Hamamatsu R5912 Mod (left up), R5912-02 Mod (right up) and ETL 9357 KFLB (down) at room and cryogenic temperature.	73
5.11	Dark count spectra for Hamamatsu R5912 Mod (left up), R5912-02 Mod (right up) and ETL 9357 KFLB (down) at room and cryogenic temperature.	74
5.12	Quantum Efficiency for Hamamatsu R5912 (top) and ETL 9357 KFLB (bottom) for incident light wavelength from 120 to 220 nm. PMT windows were coated with TPB.	75
5.13	Voltage divider used to test the Hamamatsu R5912-02 Mod. . .	76
5.14	Linearity response of Hamamatsu R5912-02 for three different power supply. The anodic signal (Meas.phe) is normalized to the expected phe numbers for the ideal case (phe).	77
5.15	Gain of the R5912-02 with the low resistance voltage divider, for signal extracted from anode and last amplification stages (from 8 th dynode).	78
5.16	Linearity response of Hamamatsu R5912-02 for gain $\sim 10^8$ at the anode. Signals were picked up both from the anode and from the last multiplication electrodes (down to the 8 th dynode). Left: Response signals (Meas.phe) are normalized to the expected phe numbers for the ideal case (phe). Right: The relation between dynode signals and the corresponding response at the anode is presented.	82
5.17	Voltage divider used to test the ETL 9357 KFLB.	83
5.18	Example of noise induced on wires by PMTs in LNGS run of T600 detector.	84

5.19	Noise signal (blue line) induced on the wire grid by the PMT signal (green line) with the PMT screened by a Faraday cage.	84
5.20	Noise signal (green line) induced on the wire grid by the PMT signal (blue line) with the PMT not screened by the Faraday cage but with 20 nF instead of 10 nF capacitor on the voltage divider (see Fig. 5.3).	85
5.21	Voltage divider to be mounted on the R5912 for the installation in the detector.	86
6.1	Simulation of the configuration with a single set of coils. Full lines refer to the dimension of the active argon volume, dotted lines to the dimension of the coils, while dashed lines to the dimension of the iron yoke.	88
6.2	Maps of the absolute value $ B $ (up) and of the vertical component B_z (down) of the magnetic field, in the planes of symmetry parallel (left) and perpendicular (right) to the ones of the coils, in the configuration with a single set of coils. Mean values in the active argon volume are $ B = 0.92 \pm 0.12$ T and $B_z = 0.92 \pm 0.12$ T, with a spread of 13%.	89
6.3	Vertical (up) and horizontal (down) component of the force on long (left) and short (right) sides of the coils. Both the components point to the outside, due to the presence of the iron yoke. The irregularity of the force values are due to the finite elements structure of the software.	90
6.4	Simulation of the configuration with two set of coils. For clarity, only the lengths of components modified with respect to previous configuration are shown. Full lines refer to the dimension of the active argon volume, dotted lines to the dimension of the coils, while dashed lines to the dimension of the iron yoke.	91
6.5	Maps of the vertical component B_z of the magnetic field, in the planes of symmetry parallel (left) and perpendicular (right) to the ones of the coils, in the configuration with two sets of coils. Mean intensities in the active argon volume are $ B = 1.23 \pm 0.16$ T and $ B_z = 1.22 \pm 0.15$ T in both chambers, with a spread of 13%.	92
6.6	Intensity of the magnetic field outside the iron yoke for the configurations with one (left) and two (right) sets of coils. At distance $d=0$ from the joke the residual field is $ B = 0.54$ T and $ B = 0.16$ T respectively, while at $d=2$ m these values decrease to $ B = 0.38$ T and $ B = 0.12$ T.	92
6.7	Schematic structure of a SiPM.	93
6.8	Layout of the acquisition system used to test SiPMs in cryogenic environment.	94
6.9	I-V reverse characteristic curves for the AdvanSiD (left) and Hamamatsu (right) devices at room and cryogenic temperature.	95

LIST OF FIGURES

6.10	Absolute amplitude of the peak as a function of the over-voltage for the AdvanSiD (left) and Hamamatsu (right) devices, at room and cryogenic temperature.	96
6.11	DCR at room and cryogenic temperature for the AdvanSiD (left) and Hamamatsu (right) devices. Errors are statistical. . .	97
6.12	Superposition of signals of the AdvanSiD (left) and Hamamatsu (right) devices recorded at 300 K and 77 K: for easier comparison the signals are normalized to their peak value. SiPMs are biased at 1 V of over-voltage.	98
6.13	Responses of the AdvanSiD (left) and Hamamatsu (right) SiPMs to the VUV light, normalized to their maximum.	98

Introduction

Liquid argon detectors have been widely used in the field of neutrino physics and dark matter search. In particular, many new liquid argon time projection chambers (LAr-TPCs) are foreseen to be constructed in the next 10-20 years.

The ICARUS T600 detector, although assembled in Pavia more than 10 years ago (2001), is so far the biggest LAr-TPC ever built. From 2010 to 2012 it was placed in the Gran Sasso laboratory (LNGS), exposed to the CNGS (CERN Neutrinos to Gran Sasso). The CNGS was a ν_μ beam, and ICARUS aim was to study oscillations to both ν_τ and ν_e states. In 2012 the CNGS beam was shot down. After a few-months of data taking with cosmic rays, the T600 was de-commissioned and transferred to CERN, where now it is under refurbishing.

At CERN the detector will be prepared for a new experimental phase: after the refurbishing, the T600 will be transported to Fermilab, in order to become the Far Detector of the Short Baseline Neutrino (SBN) experiment. Other two smaller LAr TPCs, LAr1-ND and MicroBooNE will be exposed, together with the T600, to a ν_μ and then $\bar{\nu}_\mu$ beam, aligned at distances ranging from 110 m of LAr1-ND to 479 m of MicroBooNE and 600 m T600. The SBN experiment wants give a definitive answer to the LSND-anomaly, to confirm or reject the possible presence of a fourth neutrino state, the sterile neutrino, that some experimental results have suggested.

The ICARUS Collaboration is also involved in a long time project, called DUNE (Deep Underground Neutrino Experiment): it will be a long baseline experiments, with a modular kilotons LAr-TPC, to be built in the next 20 years in a South Dakota mine. The goal is to study all the fundamental properties of neutrinos, such as CP violation, mass hierarchy and so on. The T600 could be used as Near Detector in this future experiment, once provided with a magnetic field for precise particle momentum measurements and with light collection devices able to work in magnetic environment.

In my Ph.D activities I actively contributed to all of these experimental steps, from the analysis of the data collected in Gran Sasso to the design, tests and realization of the new light collection system for the SBN experiment and to the first tests at cryogenic temperatures on SiPMs, to be used as light

detectors in DUNE experiment.

This thesis is organized as follows. In chapter 1, a brief review of the neutrino oscillations theory is presented, as well as the main experimental results that suggest the possible presence of a fourth sterile neutrino state. Chapter 2 is dedicated to the description of the T600 detector as it worked at LNGS: after a brief apparatus characterization, with a particular attention on the light detection system, the data analysis method and the principal physical results obtained will be showed. In chapter 3 the new experimental phase at Fermilab will be presented by exposing all the changes necessary to the present detector. The most important of these changes is the renovation of the light detection system: chapters 4 and chapter 5 will be devoted to the description of its design and implementation. In particular, chapter 4 is dedicated to the illustration of the Monte Carlo simulation used to design a PMT configuration able to trigger, localize and perform a first classification of the events; in chapter 5 tests performed to select the best PMT model and the operation for testing and mounting the final collection system will be displayed. Finally, in chapter 6, the studies for the possible far future application of the detector, with the presence of a magnetic field surrounding it and SiPMs as alternative photon detectors are presented.

Chapter 1

Neutrino oscillations

In the Standard Model of Glashow [3], Weinberg [4] and Salam [5], neutrinos are massless, and described by left-handed Weyl spinors. The non existence of right-handed neutrino fields is assumed: they are necessary in order to generate Dirac neutrino masses, with the same Higgs mechanism that generates the Dirac masses of quarks and charged leptons. Three generations of neutrinos are assumed, as part of the lepton doublets

$$L_l = \begin{pmatrix} \nu_{lL} \\ l_L \end{pmatrix} \quad (1.1)$$

where $l = e, \mu, \tau$. The standard neutrino interactions are described by the leptonic charged current

$$j_{W,L}^\rho = 2 \cdot \sum_{\alpha=e,\mu,\tau} \bar{\nu}_{\alpha,L} \gamma^\rho l_{\alpha,L} = \sum_{\alpha=e,\mu,\tau} \bar{\nu}_\alpha \gamma^\rho (1 - \gamma^5) l_\alpha, \quad (1.2)$$

and by the neutrino part of the leptonic neutral current

$$j_{Z,\nu}^\rho = \sum_{\alpha=e,\mu,\tau} \bar{\nu}_{\alpha,L} \gamma^\rho \nu_{\alpha,L} = \frac{1}{2} \sum_{\alpha=e,\mu,\tau} \bar{\nu}_\alpha \gamma^\rho (1 - \gamma^5) \nu_\alpha, \quad (1.3)$$

which enter respectively into the leptonic charged-current weak interaction Lagrangian

$$\mathcal{L}_l^{(CC)} = -\frac{g}{2\sqrt{2}} \left(j_{W,L}^\rho W_\rho + j_{W,L}^{\rho\dagger} W_{\rho\dagger} \right), \quad (1.4)$$

and the neutrino part of the leptonic neutral-current weak interaction Lagrangian

$$\mathcal{L}_\nu^{(NC)} = -\frac{g}{2 \cos \vartheta_W} j_{Z,\nu}^\rho Z_\rho, \quad (1.5)$$

where g is the SU(2) gauge coupling constant, ϑ_W is the Weinberg angle, W_ρ and Z_ρ are fields of charged W^\pm and neutral Z^0 vector bosons. This theoretical structure describes, with impressive accuracy, neutrino interactions: so

far, no deviation from the standard neutrino interactions have been found in experimental data [1].

On the other hand, experiments revealed a strange neutrinos behavior: they seem to change their flavor from creation to revelation [1]. This characteristic can be explained with the mechanism of neutrino oscillations, first proposed by Pontecorvo in 1958 [2]; this mechanism supposes massive neutrinos, being so a theory beyond the standard model.

1.1 Neutrino oscillations theory

In the standard theory of neutrino oscillations [6][7][8], a neutrino with flavor α is described by the flavor state

$$|\nu_\alpha\rangle = \sum_k U_{k\alpha} |\nu_k\rangle \quad (1.6)$$

where $|\nu_k\rangle$ are the mass eigenstates, while $U_{k\alpha}$ is an unitary matrix, which describes the neutrino mixing. The massive neutrino states $|\nu_k\rangle$ are eigenstates of the Hamiltonian,

$$\mathcal{H} |k\rangle = E_k |\nu_k\rangle, \quad (1.7)$$

with energy eigenvalues

$$E_k = \sqrt{\mathbf{p}^2 + m_k^2}. \quad (1.8)$$

The Schrödinger equation

$$i \frac{d}{dt} |\nu_k(t)\rangle = \mathcal{H} |\nu_k(t)\rangle, \quad (1.9)$$

implies that the massive neutrino states evolve in time as plane waves:

$$|\nu_k(t)\rangle = e^{-iE_k t} |\nu_k\rangle. \quad (1.10)$$

Let's consider now a beam composed of neutrinos of a well-defined flavor α . In the following the three momentum \mathbf{p} of the different components in the beam will be assumed the same; differences in energy will derive from the masses differences. The neutrino, created with the flavor α at time $t = 0$, is described by Eq. 1.6. After a time t , the evolution of the initial beam gives

$$|\nu_\alpha(t)\rangle = \sum_k U_{\alpha k} e^{-iE_k t} |\nu_k\rangle. \quad (1.11)$$

Since all E_k are not equal if the masses are not, Eq. 1.11 represents a different superimposition of the physical eigenstates ν_k compared to Eq. 1.6. In general, this state has not only the properties of a ν_α , but also of other flavor states. The amplitude of finding a ν_β in the original ν_α beam is

$$\begin{aligned}
 \langle \nu_\beta | \nu_\alpha(t) \rangle &= \sum_{k,j} \langle \nu_j | U_{j\beta}^\dagger e^{-iE_k t} U_{\alpha k} | \nu_k \rangle \\
 &= \sum_k e^{-iE_k t} U_{\alpha k} U_{\beta k}^*, \tag{1.12}
 \end{aligned}$$

using the fact that the mass eigenstates are orthonormal ($\langle \nu_k | \nu_j \rangle = \delta_{kj}$). At $t = 0$, as expected, the amplitude is just $\delta_{\alpha\beta}$, using the unitarity of the matrix U . At any time t , the probability of finding a ν_β in an originally ν_α beam is

$$\begin{aligned}
 P_{\nu_\alpha \nu_\beta}(t) &= |\langle \nu_\beta | \nu_\alpha(t) \rangle|^2 \\
 &= \sum_{k,j} |U_{\alpha k} U_{\beta k}^* U_{\alpha j}^* U_{\beta j}| \cos[(E_k - E_j)t - \phi_{\alpha\beta jk}], \tag{1.13}
 \end{aligned}$$

where

$$\phi_{\alpha\beta jk} = \arg(U_{\alpha k} U_{\beta k}^* U_{\alpha j}^* U_{\beta j}). \tag{1.14}$$

In all practical situations, neutrinos are extremely relativistic. The energy-momentum relation (Eq. 1.8) can be approximated as

$$E_k \sim |\mathbf{p}| + \frac{m_k^2}{2|\mathbf{p}|}, \tag{1.15}$$

and also the time t can be replaced by the distance x traveled by the beam. Thus one obtains

$$P_{\nu_\alpha \nu_\beta}(x) = \sum_{k,j} |U_{\alpha k} U_{\beta k}^* U_{\alpha j}^* U_{\beta j}| \cos\left(\frac{2\pi x}{L_{kj}} - \phi_{\alpha\beta jk}\right), \tag{1.16}$$

where, writing $|\mathbf{p}| = E$ for sake of brevity, one defines

$$L_{kj} \equiv \frac{4\pi E}{\Delta m_{kj}^2}, \tag{1.17}$$

where

$$\Delta m_{kj}^2 \equiv m_k^2 - m_j^2. \tag{1.18}$$

The quantities $|L_{kj}|$ are called oscillation lengths; they give a distance scale over which the oscillation effects can be appreciable. It has to be noticed that if the distance x is an integral multiple of all L_{kj} , then $P_{\nu_\alpha \nu_\beta} = \delta_{\alpha\beta}$, as in the original beam. But at distances where this condition is not satisfied, non trivial effects can be seen.

In the simplest assumption of an oscillation between two neutrinos only, the matrix U takes a particularly simple form:

$$\begin{pmatrix} \cos \vartheta & \sin \vartheta \\ -\sin \vartheta & \cos \vartheta \end{pmatrix}. \quad (1.19)$$

Eq. (1.16) now reduces to

$$\begin{aligned} P_{conv}(x) &= \sin^2 2\vartheta \sin^2 \left(\frac{1.27\Delta m^2}{E} x \right) \\ P_{surv}(x) &= 1 - \sin^2 2\vartheta \sin^2 \left(\frac{1.27\Delta m^2}{E} x \right), \end{aligned} \quad (1.20)$$

where the numerical constant 1.27 applies if $\Delta m^2 = |m_1^2 - m_2^2|$ is expressed in $(\text{eV}/c^2)^2$, while the distance from the neutrino source x is expressed in meters and the energy E in MeV. The subscripts *conv* and *surv* on the left sides of these equations denote the conversion and the survival probabilities of a particular neutrino flavor. The experimental data thus restrict Δm^2 as a function of $\sin^2 2\vartheta$ from the limits of the observed probabilities.

In the case of three neutrinos, instead, the mixing matrix became more complex, with three mixing angle and a phase. Its most common parametrization is:

$$U = \begin{pmatrix} 1 & 0 & 0 \\ 0 & c_{23} & s_{23} \\ 0 & -s_{23} & c_{23} \end{pmatrix} \begin{pmatrix} c_{13} & 0 & s_{13}e^{-i\delta} \\ 0 & 1 & 0 \\ -s_{13}e^{+i\delta} & 0 & c_{13} \end{pmatrix} \begin{pmatrix} c_{12} & s_{12} & 0 \\ -s_{12} & c_{12} & 0 \\ 0 & 0 & 1 \end{pmatrix} \quad (1.21)$$

where $c_{jk} = \cos(\theta_{jk})$ and $s_{jk} = \sin(\theta_{jk})$. This form of the matrix turns out to be very useful when considering experimental data, since the first matrix contains the parameters relevant for atmospheric and accelerator neutrino oscillations, the second one contains the parameters accessible to short distance reactor experiments and the CP violating phase δ , while the third matrix depends upon the parameters involved in solar neutrino oscillations.

The exposed theory is valid for neutrinos traveling in vacuum. When neutrinos propagate in matter, as for solar neutrino inside the Sun, oscillations are modified by the coherent interactions with the medium, which produce effective potentials that are different for different neutrino flavors [9]. In particular ν_e can have both NC and CC interactions with matter electrons, while $\nu_{\mu,\tau}$ are susceptible only to NC interactions. Neutrino oscillations in matter, as neutrino oscillations in vacuum, depend again on the differences of the squared neutrino masses, not on the absolute value of neutrino masses, with an effective mixing angle in matter ϑ_M . For a particular electron number density the effective mixing angle is equal to 45° , i.e. the mixing is maximal, leading to the possibility of total transitions between the two flavors if the resonance region is wide enough [10]. This mechanism is referred as Mikheev-Smirnov-Wolfenstein (MSW) effect.

1.2 Hint for sterile neutrino

The theory exposed before is confirmed by many experimental results. All the mixing angle of the matrix U (Eq. 1.21) have been measured, as well as the difference of the squared masses; value are summarized in Tab. 1.1 [11] and plotted in Fig. 1.1 [12]. The preferred value of the CP-violing phase lies around $\delta \simeq \pi$, although with low statistical significance [13].

Parameter	Best Fit ($\pm 1 \sigma$)
Δm_{21}	$7.54_{-0.22}^{+0.26} \times 10^{-5} \text{ eV}^2$
$\Delta m_{23} \simeq \Delta m_{13}$	$2.46 \pm 0.06 \text{ (} 2.38 \pm 0.06 \text{)} \times 10^{-3} \text{ eV}^2$
$\sin^2 \theta_{12}$	0.308 ± 0.017
$\sin^2 \theta_{23}, \Delta m_{13} > 0$	$0.437_{-0.023}^{+0.033}$
$\sin^2 \theta_{23}, \Delta m_{13} < 0$	$0.455_{-0.031}^{+0.039}$
$\sin^2 \theta_{13}, \Delta m_{13} > 0$	$0.0234_{-0.0019}^{+0.0020}$
$\sin^2 \theta_{13}, \Delta m_{13} < 0$	$0.0240_{-0.0022}^{+0.0019}$

Table 1.1: The best-fit values of the 3-neutrino oscillation parameters, derived from a global fit of the current neutrino oscillation data [11]. The values (values in brackets) correspond to $m_1 < m_2 < m_3$ ($m_3 < m_1 < m_2$), i.e. $\Delta m_{13} > 0$ ($\Delta m_{13} < 0$).

However a lot of questions about neutrinos remain unresolved. Up to now, direct or kinematic searches have not revealed any indication for non vanishing neutrino masses, and also the neutrino mass hierarchy remains unknown. Even the mechanism that gives mass to neutrinos remains object of discussion, such as their Majorana or Dirac character (see [1] for detailed description). Some experimental results, in addition, suggest that also the number of neutrinos should not be three as accepted until now.

Result from LEP on the Z-boson decay width [14], implies that there are only three neutrinos which interact weakly, but sets no limits on the number of *sterile* neutrinos. A sterile neutrino is defined as a neutral particle, singlet of SU(2), thus being sensible to the gravitational force only. The only way to detect them is then studying how their existence should influence the active neutrino oscillation probability. Measures of anisotropies of the Cosmic Microwave Background, sensible to the number of neutrino families, do not exclude $N_\nu > 3$; in particular $N_\nu = 4$ is also consistent with 95% C.L [15], also if tensions remain between cosmogenic results and the possible presence of light sterile neutrino.

1.2.1 Short baseline experiment

The first evidence in favor of oscillations beyond the three-flavor framework came from the LSND (Liquid Scintillator Neutrino Detector) experiment [16].

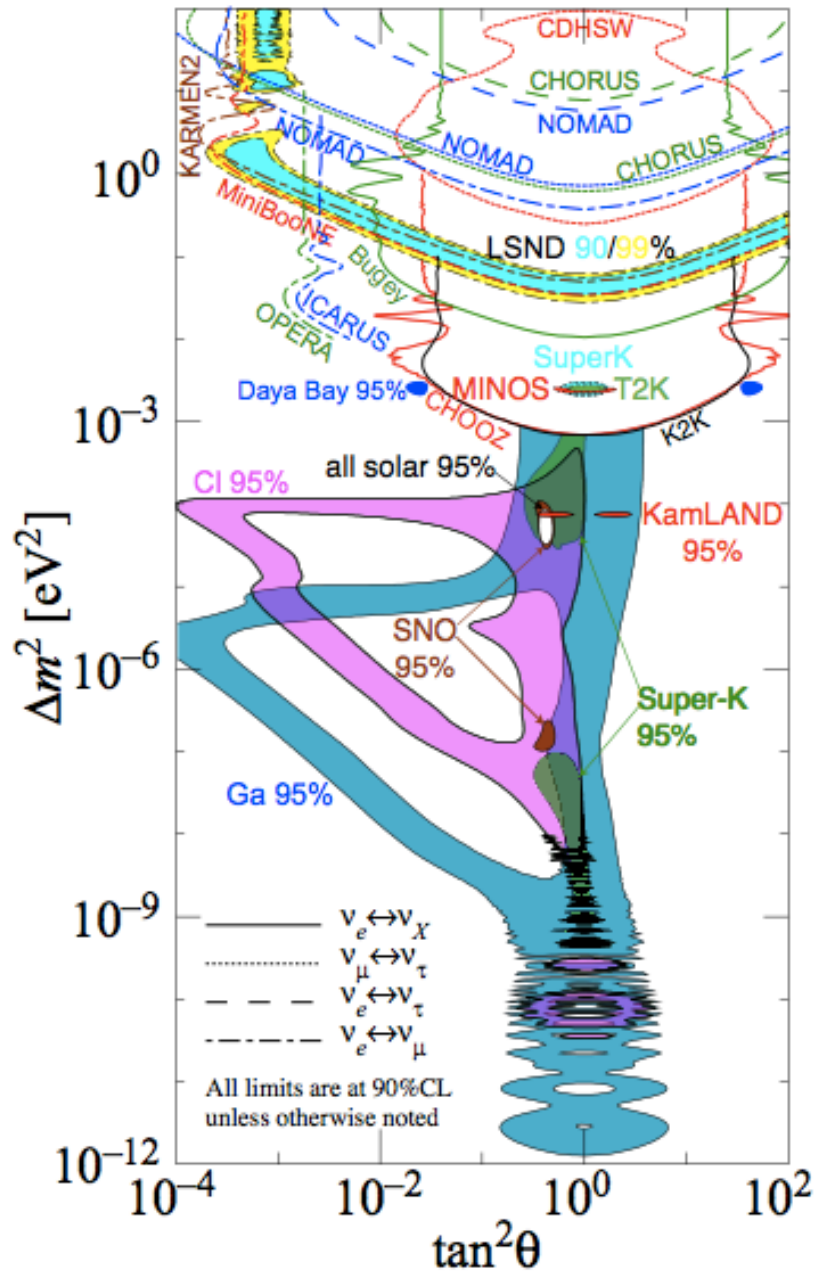


Figure 1.1: Plot of the experimental results obtained in the neutrino oscillation sector till July 2015 [12].

1.2. Hint for sterile neutrino

It was a scintillation and Cherenkov light detector, installed at Los Alamos National Laboratory, 30 m distant from an accelerator $\bar{\nu}_\mu$ source, with $20 < E_{\bar{\nu}} < 200$ MeV, to search for $\bar{\nu}_\mu \rightarrow \bar{\nu}_e$ oscillations with high sensitivity. An excess of $\bar{\nu}_e$ over the expected from background and standard oscillation was found, with an oscillation probability of $(0.264 \pm 0.067 \pm 0.045)\%$, leading to a $> 3\sigma$ evidence for $\bar{\nu}_\mu \rightarrow \bar{\nu}_e$ oscillation with $\Delta m^2 > 0.2 \text{ eV}^2$, much higher than the standard Δm^2 . In the $(\sin^2 2\theta, \Delta m^2)$ parameter space, the most favored allowed region is in the band of Δm^2 from 0.2 to 2.0 eV^2 (see Fig. 1.2) [17].

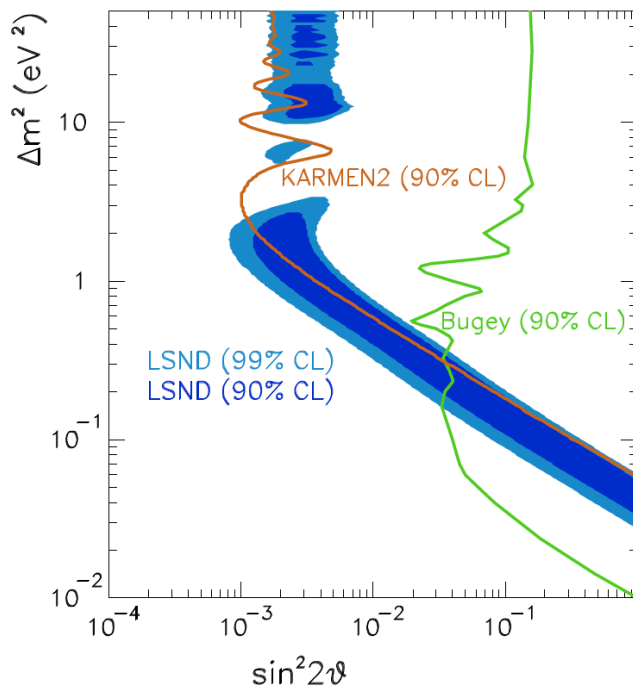


Figure 1.2: The $(\sin^2 2\theta, \Delta m^2)$ oscillation parameter fit for the entire LSND data sample, $20 < E_{\bar{\nu}} < 200$ MeV [17].

The KARMEN (KARlsruhe Rutherford Medium Energy Neutrino) experiment [18], very similar to LSND, observed no such an excess. It rules out a part of the mass-mixing parameters region allowed by LSND, but, due to the smaller baseline (17.5 m vs 30 m), in the region $< 2 \text{ eV}^2$ and around 7 eV^2 KARMEN result is compatible with the LSND oscillation evidence (see Fig. 1.2) [19].

To test the LSND anomaly, the experiment MiniBooNE (Booster Neutrino Experiment) [20] was developed at Fermilab. It was placed 541 m from the beam source. It studied both $\bar{\nu}_\mu \rightarrow \bar{\nu}_e$ and $\nu_\mu \rightarrow \nu_e$. It found an excess of ν_e events both in antineutrino and neutrino analysis (see Fig. 1.3) [21][22]. In antineutrino mode this excess is very similar to what is expected from neutrino oscillation based on the LSND signal (see Fig. 1.4); in neutrino mode, instead, the data in the energy range sensitive to LSND oscillations are consistent with the background oscillation, while a 3σ excess at low energy could

correspond to a significantly different L/E distribution than that suggested by LSND anomaly.

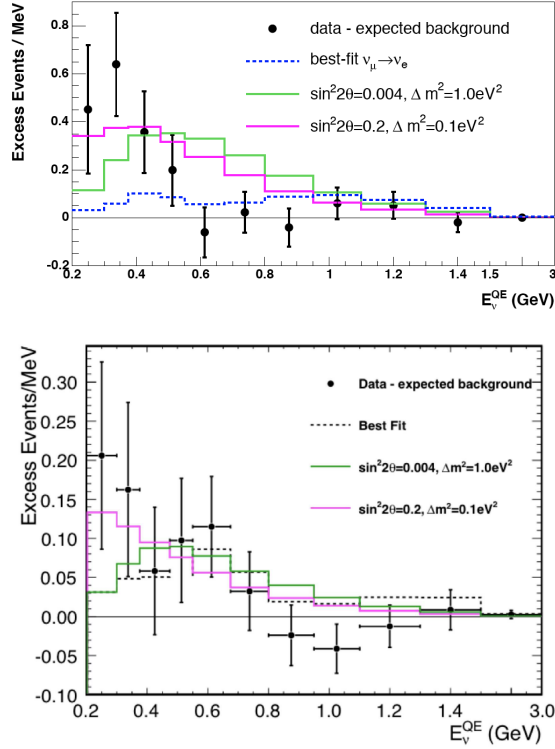


Figure 1.3: The excess of ν_e (up) and $\bar{\nu}_e$ (down) candidate events observed by MiniBooNE in neutrino and antineutrino mode respectively.

1.2.2 Gallium experiment

The GALLEX (GALLium EXperiment) [23] and SAGE (Soviet–American Gallium Experiment) [24] solar neutrino detectors are two example of the so-called Gallium radioactive source experiments. Their aim is the revelation of electron neutrinos produced by intense artificial ^{51}Cr and ^{37}Ar radioactive sources, placed inside the detectors. The radioactive nuclei decay through electron capture ($e^- + X \rightarrow Y + \nu_e$); the emitted neutrino is then detected through the reaction

$$\nu_e + {}^{71}\text{Ga} \rightarrow {}^{71}\text{Ge} + e^-, \quad (1.22)$$

which has a low neutrino energy threshold, $E_\nu^{th}({}^{71}\text{Ga}) = 0.233 \text{ MeV}$. The value of the ratio R between measured and predicted ${}^{71}\text{Ge}$ production rate, averaged between the two experiment, is

$$R = 0.86 \pm 0.05. \quad (1.23)$$

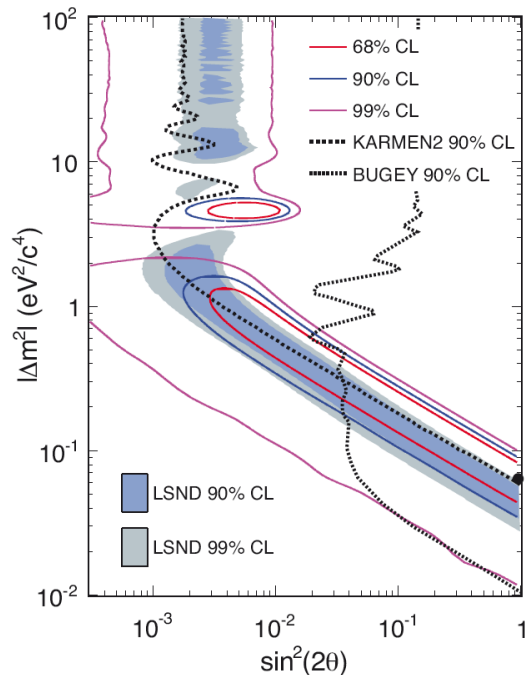


Figure 1.4: The MiniBooNE oscillation allowed region in antineutrino mode.

Thus, the number of measured events is about 2.8σ smaller than the prediction: in terms of neutrino oscillations this indicates an oscillation amplitude of $\sin^2 2\theta \geq 0.07$ and a squared-mass difference $\Delta m^2 \geq 0.35 \text{ eV}^2$ at 99% C.L. [25].

1.2.3 Reactor experiment

Nuclear reactors are very intense sources of neutrinos, produced along the β -decay chains of the fission products, that have been used all along the neutrino history, from its discovery up to the most recent oscillation studies. Since unstable fission products are neutron-rich nuclei, all β -decays are of β^- type and the neutrino flux is an actually pure electronic antineutrinos one. The neutrino oscillation search at a reactor is always based on a disappearance measurement: the observed neutrino spectrum at a distance L from the reactor is compared to the expected spectrum. If a deficit is measured it can be interpreted in terms of disappearance probability. Until late 2010, all data from reactor neutrino experiments appeared to be fully consistent with the standard oscillation theory. The measured rate of $\bar{\nu}_e$ was in reasonable agreement with that predicted from the reactor antineutrino spectra, though slightly lower than expected, with a measured/expected ratio of 0.980 ± 0.024 [26].

In preparation for the Double Chooz reactor experiment, the Saclay reactor neutrino group re-evaluated the specific reactor antineutrino flux. In 2011, they reported their results [27], which correspond to a flux a few per-

cent higher than the previous prediction. This also necessitated a re-analysis of the ratio between observed event rate and predicted rate for old published experiments with reactor-detector distances below 100 m. In Fig. 1.5 a general systematic shift more or less significantly below unity can be observed. These re-evaluations unveil a reactor antineutrino anomaly [28].

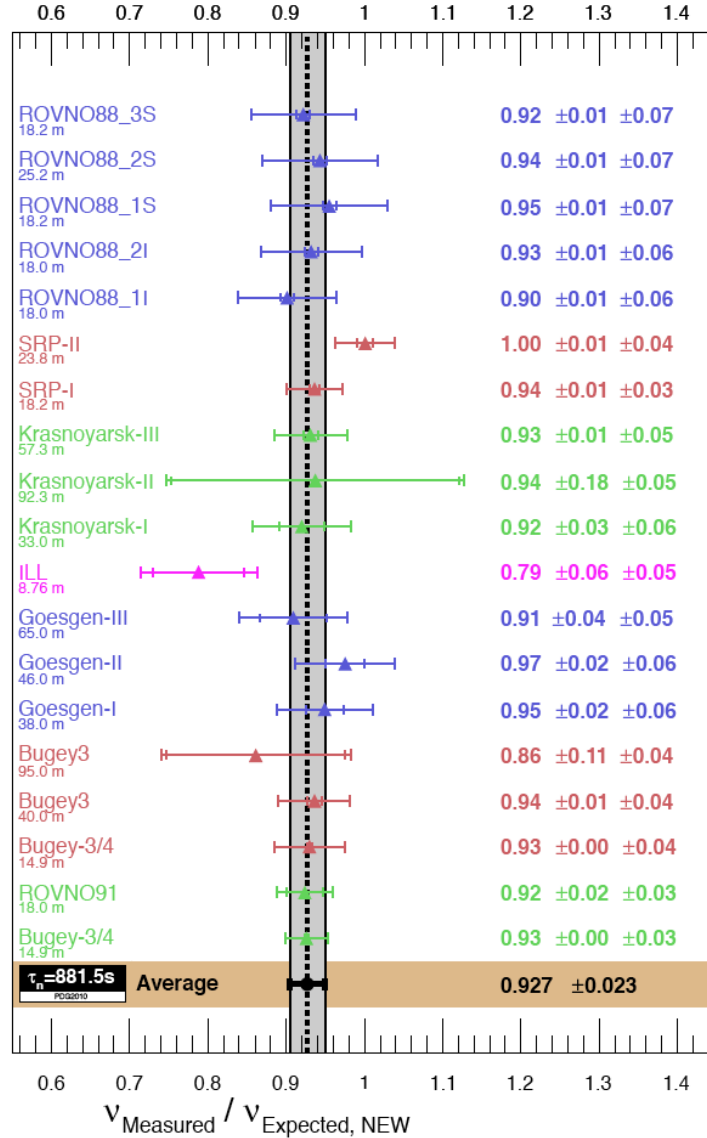


Figure 1.5: Weighted average (with correlations) of 19 measurements of reactor neutrino experiments operating at short baselines.

The average ratio is now 0.927 ± 0.023 , leading to a significance at the 3σ confidence level of the reactor antineutrino anomaly. The best fit point is at $\Delta m^2 = 2.4 \text{ eV}^2$ and $\sin(2\theta) \sim 0.14$ [28].

A global fit of the presented short-baseline neutrino oscillation data has been performed by various authors. The results exposed in [29] are showed in

1.2. Hint for sterile neutrino

Fig. 1.6, in the hypothesis of a 3+1 neutrino scheme, i.e. with only one sterile neutrino. The allowed regions in the $\sin^2(2\theta_{e\mu}) - \Delta m_{41}^2$, $\sin^2(2\theta_{ee}) - \Delta m_{41}^2$ and $\sin^2(2\theta_{\mu\mu}) - \Delta m_{41}^2$ planes are shown, obtained with a fit that does not include the low-energy excess of MiniBooNE, the PrGLO global fit in the picture. These regions are relevant, respectively, for $\nu_\mu \rightarrow \nu_e$ appearance, ν_e disappearance and ν_μ disappearance searches. The figure shows also the region allowed by $\nu_\mu \rightarrow \nu_e$ appearance data and the constraints from ν_e disappearance and ν_μ disappearance data. It can be seen that the combined disappearance constraint in the $\sin^2(2\theta_{e\mu}) - \Delta m_{41}^2$ plane excludes a large part of the region allowed by $\nu_\mu \rightarrow \nu_e$ appearance data, leading to a well-known appearance-disappearance tension.

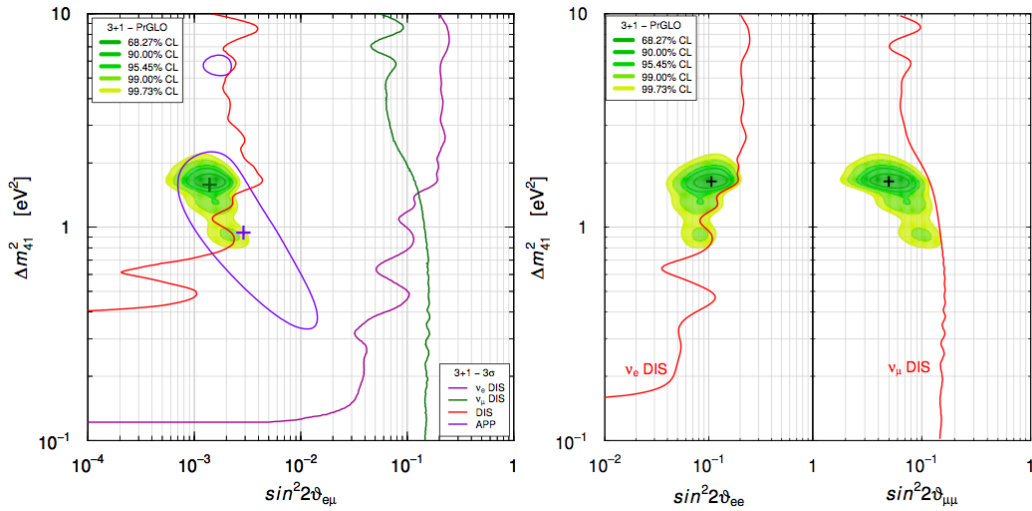


Figure 1.6: Allowed regions in the $\sin^2(2\theta_{e\mu}) - \Delta m_{41}^2$, $\sin^2(2\theta_{ee}) - \Delta m_{41}^2$ and $\sin^2(2\theta_{\mu\mu}) - \Delta m_{41}^2$ planes obtained in the 3+1-PrGLO global fit of short-baseline neutrino oscillation data compared with the 3σ allowed regions obtained from $\nu_\mu \rightarrow \nu_e$ short-baseline appearance data (APP) and the 3σ constraints obtained from ν_e short-baseline disappearance data (ν_e DIS), ν_μ short-baseline disappearance data (ν_μ DIS) and the combined short-baseline disappearance data (DIS). The best-fit points of the PrGLO and APP fits are indicated by crosses [29].

A tension is also indicated by cosmological data, between the necessity to have a sterile neutrino mass at the eV scale and the expected full thermalization of the sterile neutrinos through active-sterile oscillations in the early Universe [29].

Hence, the possible existence of light sterile neutrinos at the eV scale remains a hot topic of research and discussions.

1.2.4 Requirements for future experiments

The LSND experiment stands perhaps as the first possible evidence of new physics, beyond the Standard Model, showing an excess $\bar{\nu}_e$ signal indicative of the existence of one or more sterile neutrinos. The nature of the signal is however limited to a rate, with some energy information. The MiniBooNE experiment did not see a direct evidence in ν_e appearance, though a low energy excess in their data could potentially accommodate the existence of sterile neutrinos. Their antineutrino data, though statistically limited, appear instead to show consistency with the original LSND signal. The latest results from a re-analysis of the neutrino reactor data, which reflects a rate dependence as well, appear consistent with this sterile oscillation picture. Finally, calibration data from Gallex and Sage also suggest a deficit which hints at the existence of sterile neutrinos.

To proceed forward with a program whose goal is to establish or refute the existence of sterile neutrinos, multiple and possibly orthogonal approaches are advisable, in the same spirit as employed for neutrino oscillations. Future short-baseline experiments, such as the ICARUS involved one, can provide measurements of the energy and rate dependence using charged current reactions. A multiple detector approach will suppress the systematics, significantly increasing the sensitivity to sterile neutrinos.

Chapter 2

ICARUS at Laboratori Nazionali del Gran Sasso

Imaging detectors have always played a crucial role in particle physics. In the past century successive generations of detectors realized new ways to visualize particle interactions. This led to great progresses of physical knowledge and to the discovery of unpredicted phenomena, even on the basis of single fully reconstructed events. In particular, bubble chamber detectors were an incredibly fruitful tool, permitting to visualize and study particle interactions, that provided fundamental contributions to particle physics discoveries. Huge bubble chambers, like Gargamelle [30], were extraordinary achievements, successfully employed in particular in neutrino physics. In 1977, C.Rubbia [31] conceived the idea of a Liquid Argon Time Projection Chamber (LAr TPC), to perform the calorimetric measurement of particle energy together with the three-dimensional track reconstruction, from electrons drifting in an electric field in sufficiently pure liquid argon. The LAr TPC successfully reproduces the extraordinary imaging features of a bubble chamber, its medium and its spatial resolution being similar to those of heavy liquid bubble chambers, with the further feature of being a fully electronic detector, potentially scalable to huge masses (several kiloton). In addition the LAr TPC provides excellent calorimetric measurements and has the great advantage of being continuously sensitive and self-triggering.

The ICARUS (Imaging Cosmic And Rare Underground Signals) T600 cryogenic detector is the biggest LAr TPC ever realized, with the cryostat containing 760 tons of LAr (476 tons active mass). Its construction finalized many years of R&D studies by the ICARUS Collaboration [32][33][34][35][36], with prototypes of growing mass developed both in laboratory and with industry involvement. Nowadays, it represents the state of the art of this technique and it marks a major milestone in the practical realization of large-scale LAr detectors.

The ICARUS T600 detector operated with a remarkable detection efficiency from October 2010 to December 2012, accomplishing a three years physics pro-

gram. It was placed in the Hall B of the Laboratori Nazionali del Gran Sasso (LNGS), 1400 m (3800 m.w.e) deep and 730 km far from the source of the CNGS (CERN Neutrinos to Gran Sasso) beam, an almost pure ν_μ beam [37]. Collected neutrino events correspond to 8.6×10^{19} protons on target, with an efficiency exceeding 93%; a total of about 3000 CNGS neutrino events was collected and actively analyzed [49]. Additional data were also collected with cosmic rays, to study atmospheric neutrinos and proton decay. From the technological point of view, the T600 run was a complete success, featuring a smooth operation, high live time, and high reliability. The T600 decommissioning process started in June 2013; after the emptying and warming-up phase, the cryostats were opened, to recover the internal TPC detectors and the cryogenic plant and electronics to be re-used in future projects. The two T300 modules were moved to CERN, where a complete overhauling (CERN WA104 project) is ongoing, preserving most of the existing operational equipment, while upgrading some components with up-to-date technology in view of the T600 future non-underground operation at FNAL.

In this chapter the configuration of the ICARUS T600 at LNGS, with particular attention to the light detection system, will be described, together with the technical and physical results obtained in the LNGS run. The upgrade of the detector for the the future phase of the experiment will be treated in the next chapters.

2.1 Configuration of the ICARUS T600 detector

The ICARUS T600 detector (see Fig. 2.1) consisted of a large cryostat split into two identical, adjacent modules, with internal dimensions $3.6 \times 3.9 \times 19.6$ m³ each, filled with about 760 tons of ultra-pure LAr; each module housed two TPCs separated by a common cathode, made of punched inox sheets with 58% transparency to light. The modules will be referred in the text as West module (the oldest one) and East module (the newest one), with respect to CNGS beam coming from the North.

One thermal insulation vessel surrounded the two modules: between the insulation and the aluminum containers a thermal shield was placed, with boiling nitrogen circulating inside to intercept the heat load and to maintain the cryostat bulk temperature uniform (within 1 K) and stable at 89 K. To keep the electronegative impurities in LAr at a very low concentration level, each module was equipped with two gaseous argon (GAr) and one LAr recirculation/purification systems [37]. Argon gas was continuously drawn from the cryostat ceiling and, once re-condensed, let it pass through OxysorbTM filters and finally rejected into the LAr containers. LAr instead was recirculated by means of an immersed cryogenic pump and it was purified through standard HydrosorbTM / OxysorbTM filters before being re-injected into the cryostats.

2.1. Configuration of the ICARUS T600 detector

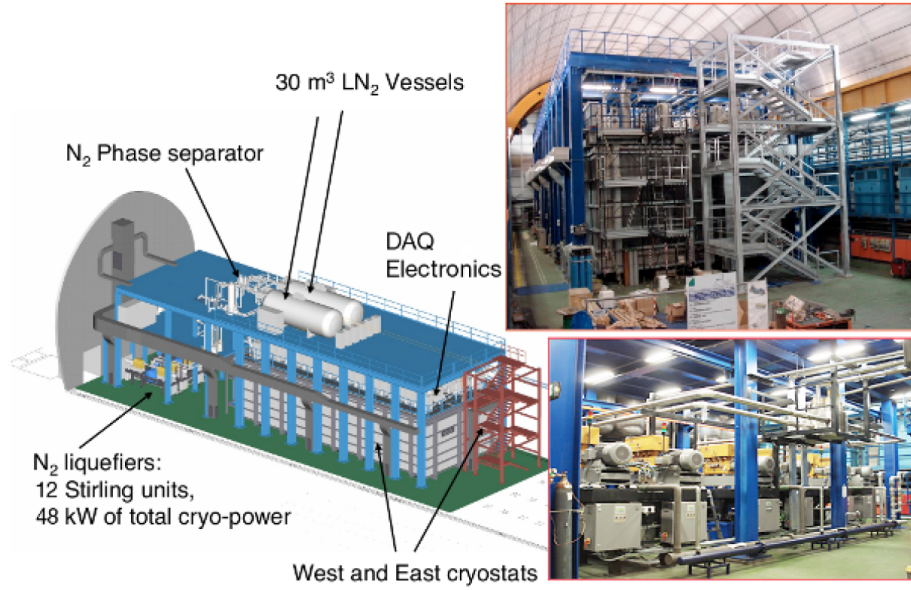


Figure 2.1: Left: schematic view of the whole ICARUS-T600 plant at LNGS. Right-top: photo of the detector installation. Right-bottom: details of the cryo-cooler plant.

Convective motions induced by heat losses from the module walls ensured a fast and almost complete LAr mixing, minimizing the fluctuations of the relevant parameters, such as LAr density, temperature and purity. This solution permitted to reach an impressive result in terms of argon purity, with a corresponding free electron lifetime exceeding 15 ms [39].

A uniform electric field ($E_{drift} = 500 \text{ V/cm}$) was applied to the LAr bulk. Charged particles, generated for example by a neutrino interaction in LAr, produced ionization along their path. Thanks to the low transverse diffusion of charge in LAr, the images of the tracks, produced by ionization electron clouds, were preserved and, drifting along the electric field lines, were projected onto the anode, as illustrated in Fig. 2.2.

The TPC anode was made of three parallel planes of wires, 3 mm apart, facing the 1.5 m drift path. Globally, 53248 wires with length up to 9 m were installed in the detector. By appropriate voltage biasing, the ionization charge induced signals in non-destructive way on the first two planes (Induction-1 and Induction-2), then it was finally collected by the last one (Collection plane). Wires were oriented on each plane at a different angle (0° , $+60^\circ$, -60°) with respect to the horizontal direction. Therefore, combining the wire/drift coordinates on each plane at a given drift time, a three-dimensional reconstruction of the ionizing event could be obtained. A remarkable resolution of about 1 mm^3 was uniformly achieved over the whole detector active volume (340 m^3 corresponding to 476 t). The measurement of the absolute time of the ionizing event, combined with the electron drift velocity information ($v_{drift} \sim 1.6 \text{ mm}/\mu\text{s}$ at

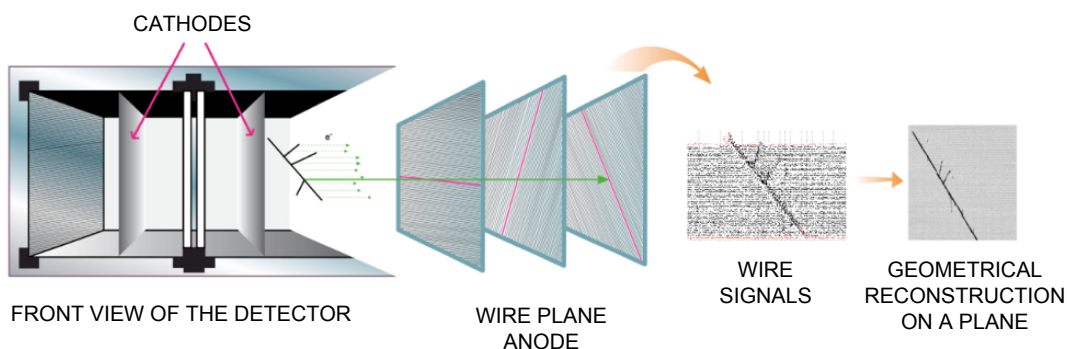


Figure 2.2: Illustration of the ICARUS T600 working principle: a charged particle ionization path in LAr and its geometrical reconstruction.

$E_{drift} = 500 \text{ V/cm}$), provided the absolute position of the track along the drift coordinate.

The determination of the absolute time of the ionizing event was accomplished by the prompt detection of the scintillation light produced in LAr by charged particles. To this purpose, arrays of cryogenic Photo Multiplier Tubes (PMTs), coated with wavelength shifter to allow the detection of Vacuum Ultra-Violet (VUV) scintillation light, were installed behind the wire planes.

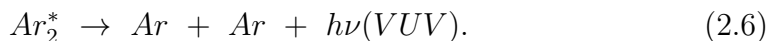
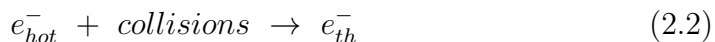
The electronics was designed to allow continuous read-out, digitization and independent waveform recording of signals from each wire of the TPC. The read-out chain was organized on a 32-channel modularity. Signals of the charge sensitive front-end amplifiers were digitized with 10-bits ADCs with 400 ns sampling channels. The overall gain was about 1000 electrons for each ADC count, setting the signal of minimum ionizing particles (m.i.p.) to ~ 15 ADC counts. The average electronic noise was 1500 electrons, compared with the ~ 15000 free electrons produced by a m.i.p. in 3 mm, leading to a signal to noise ratio $S/N \sim 10$. The gain uniformity was measured with an accuracy of about 5%, determined by the uncertainties on the capacitances adopted for calibration [50].

Stored data were read out by the DAQ every time a trigger occurred. The main ICARUS T600 trigger for detecting CNGS beam related events required the coincidence of the PMT local trigger in at least one of the four TPC chambers with a $60 \mu\text{s}$ gate opened in correspondence of the proton spill extraction, delayed for the $\sim 2.44 \text{ ms}$ CERN-to-LNGS neutrino time-of-flight. The PMT local trigger was obtained, separately for each TPC, as the linear sum of the collected PMT signals, properly discriminated in order to account for the different number of devices deployed in the two modules [38] (see par. 2.1.1). The analysis of the performance of the PMT trigger systems demonstrated an almost full PMT trigger efficiency for CNGS neutrino events above 300 MeV energy deposition on the full T600 active volume. Efficiency remained at $\sim 98.5\%$ down to 100 MeV (see par. 2.1.1). The stability of the trigger system was verified within the measurement uncertainty, comparing different data sets collected

during the CNGS run [38]. A second source of triggers, the S-Daedalus system, was gradually implemented, starting from the end of 2011, to increase the efficiency of the ICARUS T600 detector for low energy events down to few MeV and to provide a reference for measuring the PMT trigger performances; this was based on a new algorithm that detected the ionizing tracks through a digital filter of each TPC wire signal, allowing the trigger on charge deposition [38].

2.1.1 Light collection system

An interaction in argon produces both atomic excitation and ionization, leading to a narrow band 128 nm luminescence emission [60][61][62]. As experimentally measured the scintillation light exhibits two different components: the so-called recombination luminescence and self-trapped exciton luminescence (excitation luminescence). The recombination luminescence, L_r , in the VUV range, originates from the following processes [63]:



In the previous processes the symbol Ar stands for an argon atom, Ar^+ for an atomic ion, Ar^* for an excited atom, Ar^{**} for a highly excited atom, Ar_2^+ for a molecular ion (dimer), Ar_2^* for an excited molecule, e_{hot} for a sub-excitation electron and e_{th} for a thermalized electron. As suggested by the name this process is essentially driven by the presence of a free electron-ion pair. On the other hand the excitation luminescence, L_{ex} , produced by the simpler process [63]



is prompted by the presence of the excited argon atom. Both processes, ending up with the same radiative reaction, induce the emission of a 128 nm VUV photon ($E \simeq 9.7$ eV). The analysis of the light emission spectrum shows that atomic de-excitation photon emission by Ar^* is strongly suppressed: in average, the Ar^* atom captures an Ar atom and forms a Ar_2^* bound state before atomic de-excitation occurs. Scintillation light, coming from the recombination of electron-ion pairs, is inversely proportional to the strength of the electric field applied to the detector active volume. As a consequence, free-electron yield

rises with the field value while photon yield decreases. In both cases saturation occurs, for minimum ionizing particles, at $E_{drift} \geq 10$ kV/cm. At the nominal drift field applied in ICARUS T600, approximately the same amount of photons (~ 4000 γ /mm) and free electrons (~ 5000 ion-electron pairs per mm) are produced for minimum ionizing particles (m.i.p.) [40].

Both L_r and L_{ex} are characterized by a double time emission scale: carrying out measurements at different field conditions, it can be demonstrated that both excitation and recombination luminescence show two different components, one with a decay time $\tau_f \simeq 6$ ns, the other with $\tau_s \simeq 1.5$ μ s [60]. This feature, common to many scintillating materials, can be attributed, in this case, to the fact that Ar_2^* , before decaying to the fundamental dissociate state $^1\Sigma_g^+$, can be formed in three different states: two singlets ($^1\Sigma_u^+$ and $^1\Sigma_u^-$) and one triplet ($^3\Sigma_u^+$) state [64]. While the second singlet state cannot decay radiatively due to parity conservation, the other two can, although the triplet-to-ground state transition should be in principle forbidden by the selection rule $\Delta S = 0$, thus resulting in two different decay constants, the latter much larger than the former. This quite large difference is unique in argon among other noble gases. The relative intensity of the two components, fast (c_f) and slow (c_s), depends on the dE/dx of the interacting particle, ranging from $c_f : c_s \simeq 1 : 3$ in case of m.i.p. up to $c_f : c_s \simeq 3 : 1$ in case of high ionizing particle, such as α , allowing in some particular cases a particle discrimination [41].

This isotropic light signal propagates with negligible attenuation throughout LAr volume. Indeed, LAr is fully transparent to its own scintillation light, with measured attenuation length in excess of several meters and Rayleigh scattering length of ~ 90 cm [40]. Because their short wavelength, the scintillation photons are absorbed by all detector material without reflection, leaving time and amplitude information unaffected during the photon path to the light detectors. So they keep information about the time of generation, i.e. the ionizing particle interaction time and the time evolution of the interaction event in LAr.

The T600 light collection system, in the LNGS configuration, was based on the large surface Photo-Multiplier 9357 FLA Electron Tube, a 12-stage dynode PMT, with hemispherical glass window, 200 mm (8") diameter, manufactured to work at cryogenic temperatures [42]. The main physical and electric characteristics of the devices can be summarized as: 300 \div 500 nm spectral response; 5 ns rise time and 8 ns FWHM; 5×10^7 maximum gain with 18% maximum quantum efficiency (blue) with platinum under-layer.

The PMT sensitivity to VUV photons (128 nm) was achieved by coating the glass window with Tetra-Phenyl-Butadiene (TPB), which acts as fluorescent wavelength shifter from VUV wavelengths to the PMT sensitive spectrum. A TPB coating of thickness 0.2 mg/cm² on sand-blasted glass guaranteed a conversion efficiency better than 90% and good adhesion after immersion in LAr, resulting in a PMT response with 4% overall quantum efficiency [43].

PMTs, directly immersed in LAr, were located in the 30 cm space behind

2.1. Configuration of the ICARUS T600 detector

the wire planes of each TPC, at 5 mm distance from the Collection wires, with a dedicated sustaining structure specially designed to compensate the thermal stresses occurring during the cooling of the T600 cryostat (Fig. 2.3 Left). Three rows of 9 PMTs, spaced by 2 m, found place in the East module behind each wire chamber for a total amount of 27+27 photo-devices. In the West module only the two central rows were deployed; two additional PMTs were placed in the top and bottom positions in the Right chamber at the center of the longitudinal direction, for an overall amount of 20 PMTs (Fig. 2.3 Right) [50].

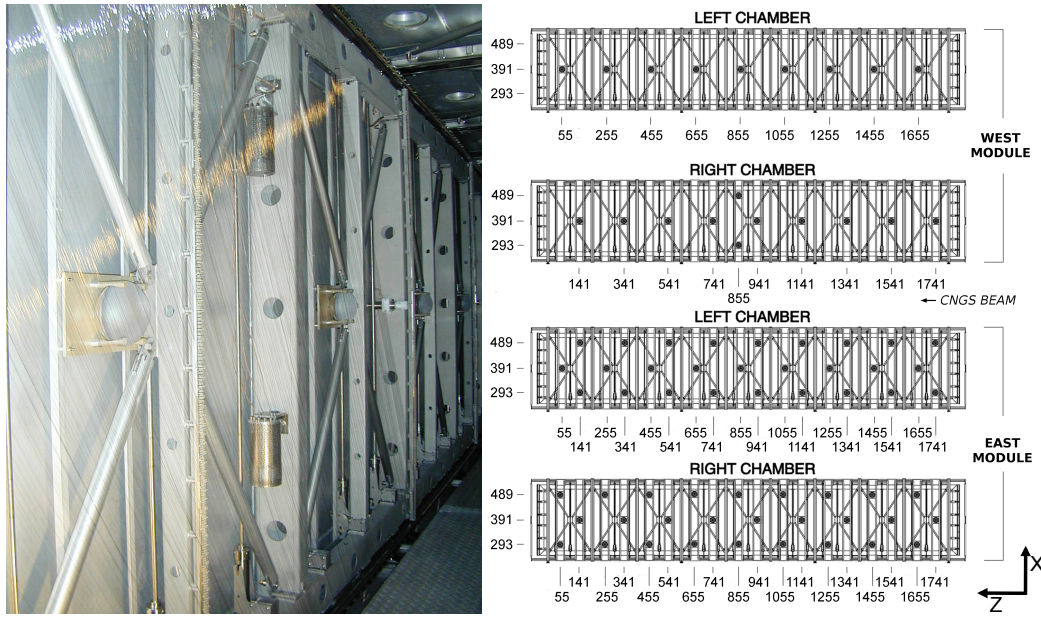


Figure 2.3: Left: internal view of one of the West Module TPC, with a few PMTs clearly visible together with their sustaining structure. Right: PMTs deployment in the two ICARUS T600 cryostats. PMT coordinates in cm are related to the reference frame used in Hall B.

The electronic scheme associated to each PMT is shown in Fig. 2.4. A voltage divider, designed to work at low temperatures and welded directly on the PMT output leads, was internally connected through RG316 cables to dedicated HV feedthroughs on the top of the detector. A single RG58 cable was used to provide each PMT with the proper power supply and to pick-up the anode signal. For this purpose, custom circuits were realized hosting the HV distribution, the decoupling boards and a custom-made low-noise integrating preamplifier. The integration time constant, $\sim 30 \mu\text{s}$, was adjusted to collect both the fast and the slow scintillation light component, with a gain of 5 mV/pC.

The PMT gains were equalized at the LAr temperature to about 10^6 , corresponding to a Single Electron Response (SER) of $\sim 0.2 \text{ pC}$, obtained by measuring each PMT response to single photon excitation through a calibrated charge preamplifier. The electronic chain gain and linearity were determined

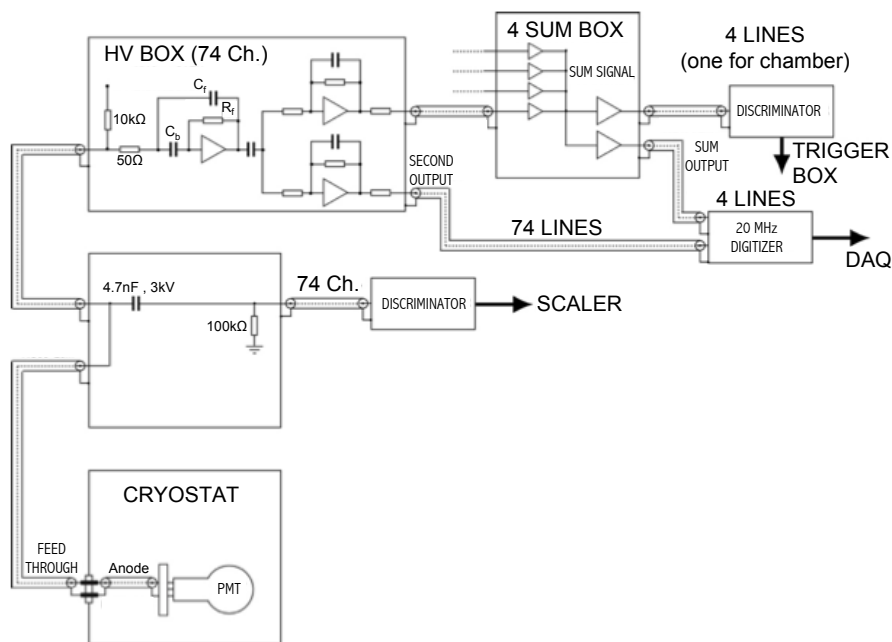


Figure 2.4: PMT electronics layout.

by means of charge calibrated test pulses. The resulting overall gain was ~ 1 mV/phe at the pre-amplifiers output, with a $\sim 5\%$ stability over the entire data taking. For each device the corresponding SER counting rate was $\sim 10^4$ Hz, due to PMT noise and to single photons from low energy radioactivity in LAr, mainly ^{39}Ar . Preamplifier outputs were connected to 4 analogue-adder electronic circuits, which provided the linear sum of the input signals with adjustable gain, to account for the different number of PMT deployed in the two modules. The overall gains, measured using test pulses, resulted to be 0.38 mV/phe and 0.12 mV/phe for the West and East module chambers, respectively. Since July 2012, for each triggered event the PMT waveforms (see Fig. 2.5) were sampled and recorded by 19 digitizers CAEN-V791PM (10-bit ADC, 1 mV/ADC count and 20 MHz sampling rate), providing a useful tool for measuring the PMT trigger efficiency. The adopted DAQ settings allowed recording PMT waveforms without saturation for signal amplitudes up to ~ 750 mV. The PMT trigger electronics was completed with a monitoring system of the single PMT counting rate.

2.1.2 PMT system performances

The angular acceptance of the single PMT in terms of collected light was evaluated with a sample of 440 almost vertical ($\delta < 10^\circ$) cosmic muons, spanning all the detector length with a deposited energy peaked around 750 MeV with a small width distribution. The number of fired devices for each muon track was determined through the distribution of the signal pulse-height as a function of

2.1. Configuration of the ICARUS T600 detector

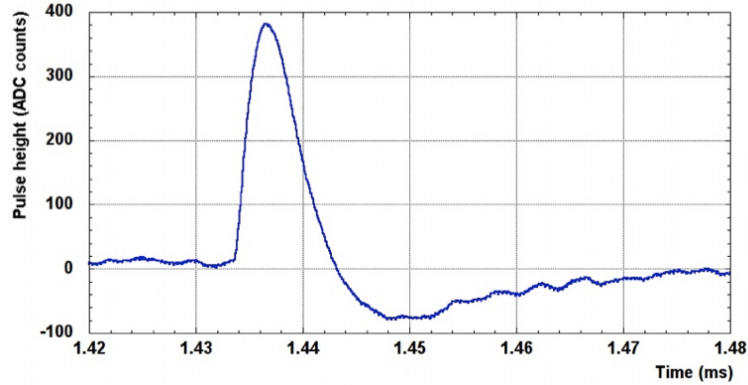


Figure 2.5: Example of recorded PMT waveform after integration of fast and slow light components.

the longitudinal distance of the track from the PMT in the Right chamber of West module (see Fig. 2.6). Photons emitted by tracks crossing the detector at a distance greater than the 2 m PMT spacing, are also detected by the single PMTs; this guarantees an almost full coverage of the LAr active volume. Signals from tracks crossing the adjacent chamber were also recorded, although with a reduced intensity due to the 58% cathode transparency. Because of the large amount of light production, the pulse-height of the sum signals from the PMT walls exceeded the ADC dynamic range ($\sim 2000/6000$ phe for the West/East module) for cosmic tracks crossing the TPC chamber close to the wire plane [38].

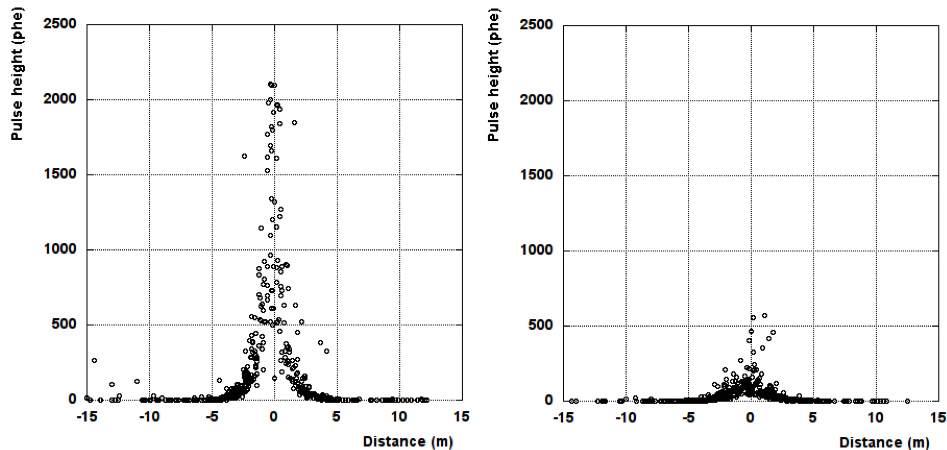


Figure 2.6: Single PMT pulse-heights in the Right chamber of the West module as a function of the longitudinal distance of vertical tracks from the PMT when the cosmic muon is crossing the Right (left) and the Left (right) TPC [38].

The efficiency of each PMT sum signal in detecting charged tracks ϵ was evaluated on a sample of cosmic muons crossing a single TPC, recorded in 2012

with a minimum bias trigger based on the TPC wire signal. Events were triggered with the S-Daedalus system, requiring signal from at least 12 over 16 consecutive Collection wires, corresponding to ~ 4 cm track length. The efficiency ϵ , determined looking for events with PMT sum signal above threshold, was studied as a function of deposited energy E_{dep} , of the track distance from PMT wall and of the position of the track along the detector longitudinal axis. As expected, it increased with the energy deposition (Fig. 2.7 -top), reaching 90% and 100% values in the East module for $E_{dep} > 300$ MeV, while slightly lower values were reached in the West module due to the smaller number of deployed PMTs. The rise of the detection efficiency with the track distance from the PMT wall in the West module (Fig. 2.7 - center) was due to the poor PMT solid angle coverage for tracks close to wires. The detection efficiency was almost optimal along all the 20 m detector length, except for the downstream region of the Right chamber in the West module where 2 PMTs were switched off (Fig. 2.7 - bottom). The associated systematic error ranged from 3.5% (2%) in the lowest energy bin for the West(East) module down to less than 1% in the highest energy bin for both modules, according to the overall 6.4% uncertainty in the threshold level obtained combining the stability of each PMT gain with the tolerance of the PMT sum signal discriminator [38]. A remarkable stability of the PMT system detection efficiency, well within the measurement uncertainty, was verified by comparing different data subsets of the 2012 run [38]. The comparison of the pulse-height of the PMT sum signals with the corresponding energy deposited by cosmic muons allowed an estimation of the quantum efficiency of the light collection system (PMTs + TPB). For each PMT wall only tracks crossing the chamber beyond the cathode were considered, in order to avoid dealing with saturated ADC. A quantum efficiency Q.E.=[4.9 ± 0.1 (stat) ± 0.7 (sys)]% was determined for the East module [38], roughly in agreement with the laboratory measurements performed before the PMTs deployment in the T600 [42].

2.2 Events analysis

The CNGS neutrino facility [44][45][46] provided an almost pure ν_μ beam peaked in the range $10 \leq E_\nu \leq 30$ GeV, with a spectral contamination from $\bar{\nu}$ of about 2% and a ν_e component of slightly less than 1% [52].

From October 1st 2010 to December 3rd 2012 ICARUS T600 collected 19990 triggered events (see Tab. 2.1) [49].

Empty events inside the recorded CNGS sample were rejected through a dedicated automatic filter based on charge deposition, whose efficiency close to 100% was checked on a sample of few thousands visually scanned events. A few neutrino interactions/day with vertex in the fiducial volume were recorded, as expected. The classification of the events was performed visually, through a two level scanning [47]. The first level scanning was meant to identify [47]:

- neutrino interaction, by looking for neutral particle interaction vertices

2.2. Events analysis

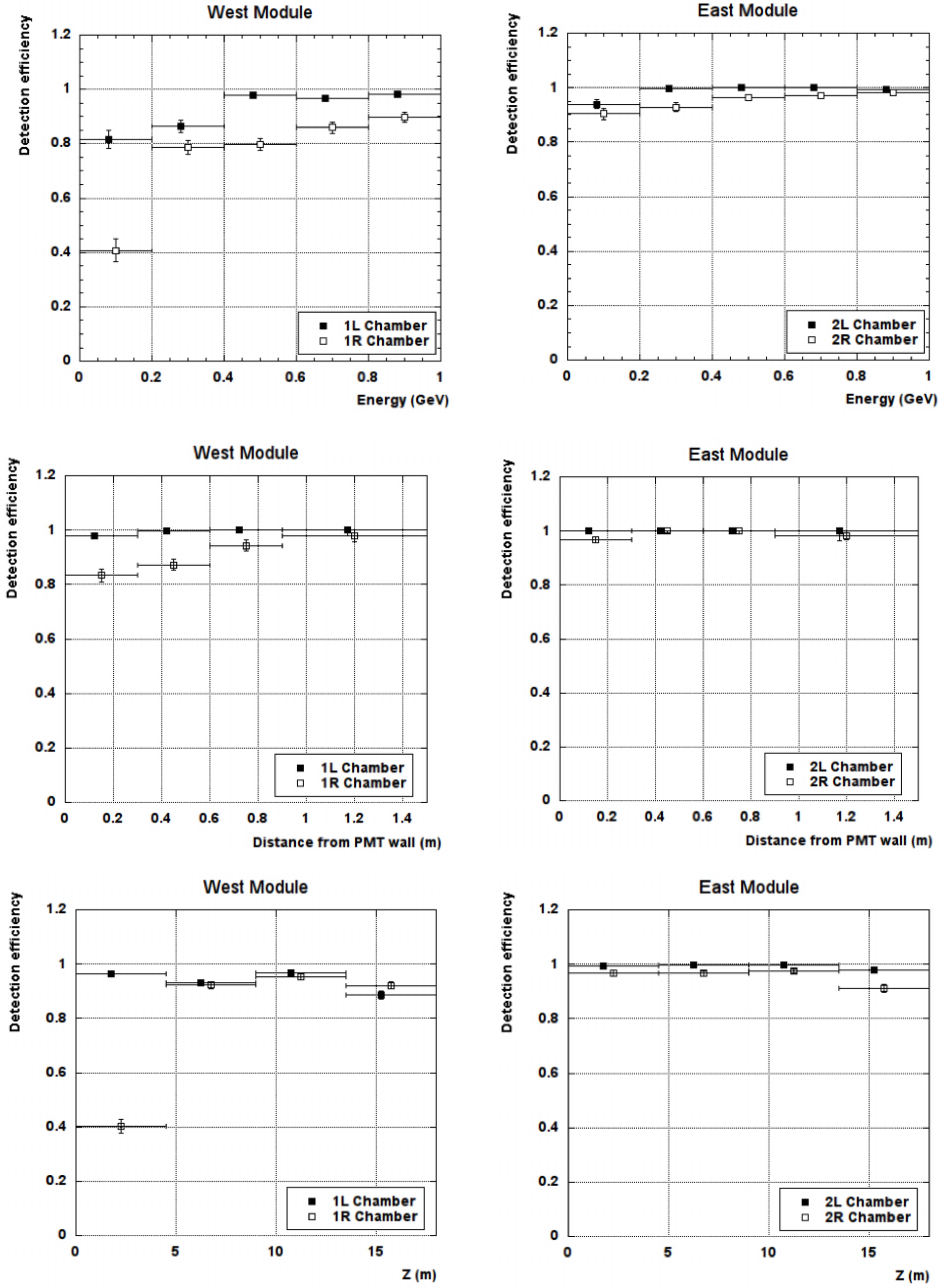


Figure 2.7: PMT sum signal efficiencies of each TPC chamber in the West (left) and East (right) modules, as a function of the energy deposited by cosmic muons (top), the track distance from the PMT wall (center) and the track longitudinal position (bottom). The represented error bars account only for the statistical error [38].

Event type	Number of events
ν	2650
Rock μ	9245
External	3568
Empty	4527
Total	19990

Table 2.1: Classification of the CNGS events among neutrinos, μ from the rock, external interaction and empty [49].

inside the detector active volume;

- muons from the rock (rock muons), i.e. μ from ν_μ interaction with the upstream rock, by looking for straight muon tracks along the beam directions entering the detector walls;
- residual of ν interaction with vertex outside the instrumented volume, by looking for events with physical activity close to the detector walls and without an interaction vertex clearly visible.

Furthermore, a preliminary classification of neutrino events was attempted by means of a visual scanning on the basis of simple criteria [47]:

- muon candidate if a long or isolated muon track exits from the vertex without re-interactions;
- NC candidate if neither electromagnetic shower close to the vertex nor muon tracks are clearly visible;
- e.m. candidate if an electromagnetic shower is recognized close to the interaction vertex;
- doubt between muon and NC (XC) in all the other cases.

The results of this scanning was inserted in a dedicated event database where the main characteristics of events, like run and event numbers, event classification and interaction vertex coordinates, were recorded. This represented a key tool, as the only repository of the list and of the primary features of the CNGS events: any information was available at any time, shared with the analysis staff and continuously updated thanks to the feedback of the subsequent steps of the analysis.

A second level scanning was then performed focusing on the neutrino interactions only, to better define the data sample. For this purpose a Scanning Fiducial Volume (SFV) was defined by subtracting from the instrumented volume of each TPC chamber 20 cm in the longitudinal beam direction (5 cm

2.2. Events analysis

upstream and 15 cm downstream) and 3 cm in the drift and vertical dimension (1.5 cm per side). The ν induced event with vertex inside the SFV are then classified as [47]:

- ν_μ CC candidate if a muon track, longer than 2.5 m, exits from the vertex without re-interactions;
- ν_e CC candidate if an electromagnetic shower is recognized with a distance from the vertex lower than 2 wires both in Collection and Induction 2 views;
- NC candidate if neither electromagnetic shower close to the vertex nor muon track are clearly visible and if the event is not well balanced in the drift and vertical dimension;
- doubt between ν CC or NC (XC) event in all the other cases.

Results are reported in Tab. 2.2 [49].

Event type	Number of events
ν_μ candidates	1517
ν_e candidates	407
NC candidates	413
XC	313
Total	2650

Table 2.2: Second classification of the CNGS neutrino interactions [49].

The identification of the primary vertex of two-dimensional objects, like tracks and showers, was performed visually. The obtained clusters and reference points were fed to the three dimensional reconstruction algorithm described in detail in [51]. The collected charge was calculated for each "hit" (a point in the wire-drift projection) in the Collection view after automatic hit finding and hit fitting [50][51]. Each hit was corrected for the signal attenuation along the drift, according to the purity value as continuously monitored with cosmic muons.

Stopping tracks were processed for particle identification through specific ionization [51]. The total deposited energy was obtained by calibrated sum of hit charges in the region spanned by the event, with an average correction factor for signal quenching in LAr. In order to reproduce the signals from the actual events, a sophisticated simulation package dedicated to the ICARUS T600 detector was developed [52].

2.2.1 Search for LSND anomaly

The search for $\nu_\mu \rightarrow \nu_e$ events due to the LSND anomaly was based on 168 neutrino events collected in 2010 (0.58×10^{19} pot), 1340 events collected in 2011 (4.11×10^{19} pot) and 1142 events collected in 2012 (3.24×10^{19} pot), leading to a total of 2650 observed neutrino events and 7.93×10^{19} pot, in good agreement, within 6%, with the Monte Carlo expectation [49]. To this initial sample, a more stringent fiducial volume cut was applied, compared with the SFV: the interaction vertex position was required to be at a distance of at least 5 cm from each side of the active volume and at least 50 cm from its downstream wall. These cuts allowed for the identification of electron showers, but are neither stringent enough for the reconstruction of neutrino energies, nor for the identification of ν_μ CC vs NC events. Furthermore, only events with a deposited energy smaller than 30 GeV were included in the analysis, in order to optimize the signal over background ratio. Indeed, the oscillated events were expected to have energies in the 10-30 GeV range, like the bulk of the muon neutrino spectrum, while the beam ν_e contamination extends to higher energies.

The radiation length of LAr is 14 cm (≈ 45 readout wires), corresponding to a γ -conversion length of 18 cm. The ionization information of the early part, i.e. before the occurrence of the e.m. track showering, was examined wire by wire in order to tag the presence of an initial electron emitted in the neutrino interaction, as a powerful eliminator of γ -converting pairs, which are generally separated from the vertex and generate double minimum ionizing tracks. The rejection factor based on ionization increased dramatically with the photon energy increase, while the electron identification efficiency was almost constant. Indeed, the possible photon misidentification was essentially due to photons undergoing Compton scattering, whose cross section becomes negligible with respect to the pair production above a few hundreds MeV. Monte Carlo studies indicated a residual contamination of about 0.18% for the energy spectrum of photons from pion decays in CNGS events, rising to a few percent in the sub-GeV energy region. The loss in efficiency for electron showers was only 10% [52][53].

In the analysis the electron signature was so defined by the following requirements [52][53]:

- vertex of the event inside the new fiducial volume;
- visible event energy smaller than 30 GeV, in order to reduce the beam ν_e background;
- presence of a charged track starting directly from the vertex, fully consistent, over at least 8 wire hits, with a minimum ionizing relativistic particle, i.e. average dE/dx lower than 3.1 MeV/cm after removal of visible delta rays, and subsequently building up into a shower;
- visible spatial separation from other ionizing tracks within 150 mrad in the immediate proximity of the vertex in at least one of the two trans-

2.2. Events analysis

verse views ($\pm 60^\circ$), except for short proton like recoils due to nuclear interactions.

In order to determine the electron selection efficiency η , MC ν_e events were generated according to the ν_μ CC spectrum. A simulated event is shown in Fig. 2.8.

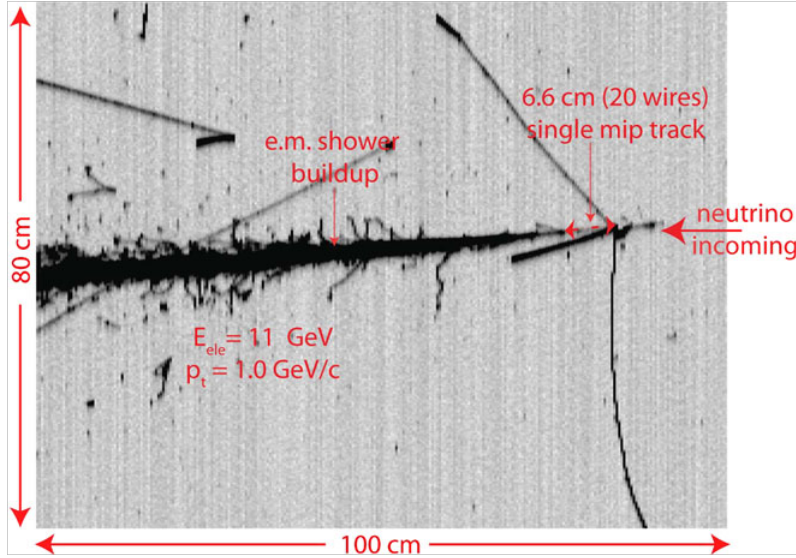


Figure 2.8: Typical Monte Carlo generated ν_e event with $E_e = 11$ GeV and $p_T = 1.0$ GeV/c.

Out of an initial sample of 171 $\nu_\mu \rightarrow \nu_e$ reconstructed MC events, 146 events had a visible energy smaller than 30 GeV, 122 of which satisfy the fiducial volume cuts. These events were visually and independently examined by three different people. An excellent agreement was found with differences in less than 3% of the sample. As a result, the average number of positively identified electron-like neutrino events was 90, corresponding to a selection efficiency $\eta = 0.74 \pm 0.05$. The same analysis was carried out on a sample of 300 simulated event induced by the intrinsic ν_e contamination, giving the slightly lower value $\eta = 0.65 \pm 0.06$, as contamination events generate an harder spectrum with respect to the above considered anomalies. An agreement better than 2.5% was found between the measured and the predicted scale of the dE/dx for muons in ν_μ CC; then the systematic error on η , induced by the dE/dx cut, resulted to be smaller than 1%. A similar analysis on 800 MC neutral current events showed no presence of apparent $\nu_\mu \rightarrow \nu_e$ events, consistent with an estimated upper limit of 0.3 events, including possibly misidentified ν_μ events [52][53].

An example of ν_e is shown in Fig. 2.9. The event has a total energy of 11.5 ± 2.0 GeV and an electron of 10 ± 1.8 GeV, taking into account a partially missing component of the e.m. shower. The single electron shower in the transverse plane is opposite to the remaining of the event, with the electron

transverse momentum of 1.8 ± 0.4 GeV/c. Fig. 2.10 displays the actual dE/dx of the electron shower along individual wires, in the region ≥ 4.5 cm from primary vertex, where the track is well separated from other tracks and heavily ionizing nuclear prongs.

The expected number of ν_e events due to conventional sources in the energy range and fiducial volumes defined before and for the total analyzed statistics was:

- 4.9 ± 0.7 events due to the estimated ν_e beam contamination;
- 2.2 ± 0.4 ν_e events due to the presence of θ_{13} oscillations from $\sin(\theta_{13}) = 0.0234 \pm 0.002$ [54];
- 1.3 ± 0.1 ν_τ with $\tau \rightarrow e$ from the three neutrino mixing standard model predictions [55],

giving a total of 8.4 ± 1.1 expected events, where the uncertainty on the NC and CC contaminations has been included and the selection efficiency reduction has been applied.

Given the smallness of the number of electron like signal expected in absence of LSND anomaly, the estimated systematic uncertainty on the predicted number is clearly negligible with respect to its statistical fluctuation. In the recorded experimental sample, 7 events, in which a ν_e signature have been identified, were found, to be compared with the above expectation of 8.4 ± 1.1 events from conventional sources [49]; the probability to observe a statistical under-fluctuation resulting in 7 or less ν_e events is $\simeq 33\%$.

Within the range of ICARUS observations, the result is then compatible with the absence of a LSND anomaly. Following the statistical analysis of [56], at confidence levels of 90% and 99% and taking into account the detection efficiency η , the limits due to the LSND anomaly are respectively 5.7 and 11.4 events. According to the above described experimental sample and the number of recorded events, the corresponding limits on the oscillation probability are $\langle P(\nu_\mu \rightarrow \nu_e) \rangle \leq 3.92 \times 10^{-3}$ and $\langle P(\nu_\mu \rightarrow \nu_e) \rangle \leq 7.83 \times 10^{-3}$, respectively. The exclusion area of the ICARUS experiment referred to neutrino-like events is shown in Fig. 2.11, in terms of the two dimensional plot of $\sin^2(2\theta_{new})$ and Δm_{new}^2 [49].

In the interval $\Delta m_{new}^2 \simeq 0.1$ to $\Delta m_{new}^2 > 10$ eV² the exclusion area is independent from Δm_{new}^2 with $\sin^2(2\theta_{new}) = 2.0 \langle P(\nu_\mu \rightarrow \nu_e) \rangle$. In the Δm_{new}^2 interval from $\simeq 0.1$ to $\simeq 0.01$ eV², the oscillation is progressively growing and averages to about the above value of twice $\langle P(\nu_\mu \rightarrow \nu_e) \rangle$. For even lower values of Δm_{new}^2 , the longer baseline strongly enhances the oscillation probability with respect to the one of the previous short baseline experiments.

2.2.2 Antineutrino analysis

The LSND result was based on antineutrino events. A small $\simeq 2\%$ antineutrino event contamination is also present in the CNGS beam as experimentally

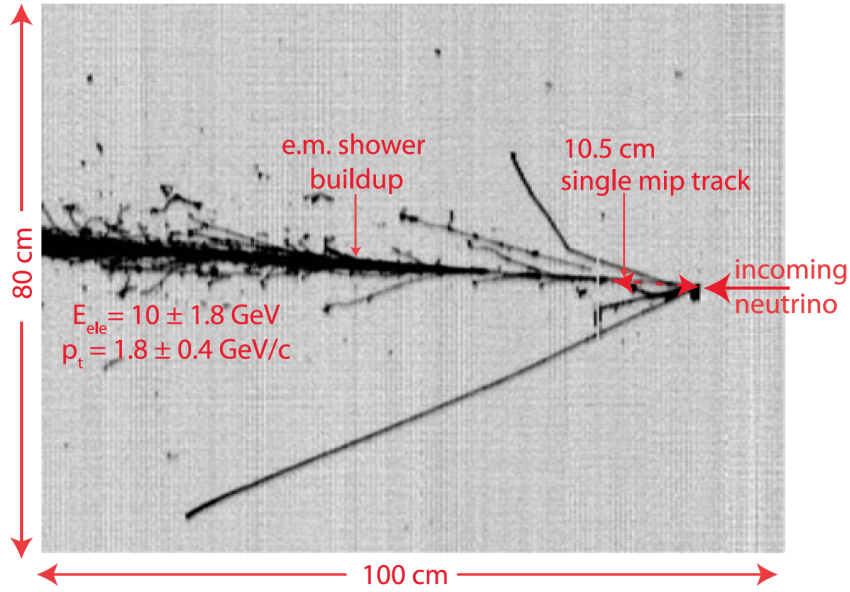


Figure 2.9: Experimental picture of an event with a clearly identified electron signature. Event has a total energy of $11.5 \pm 1.8 \text{ GeV}$, and a transverse electron momentum of $1.8 \pm 0.4 \text{ GeV}/c$. The single electron shower in the transverse plane is clearly opposite to the remaining of the event.

observed [57]. According to a detailed neutrino beam calculation, the $\bar{\nu}_\mu$ CC event rate is $(1.2 \pm 0.25)\%$ for $E_\nu < 30 \text{ GeV}$, where a 20% uncertainty has been conservatively assumed. In the limiting case in which the whole effect is due to $\bar{\nu}_\mu \rightarrow \bar{\nu}_e$, the absence of an anomalous signal registered gives a limit of 4.2 events at 90% CL. The corresponding limit on the oscillation probability is $\langle P(\bar{\nu}_\mu \rightarrow \bar{\nu}_e) \rangle \leq 0.32$. The resulting (small) exclusion area is shown in Fig. 2.12.

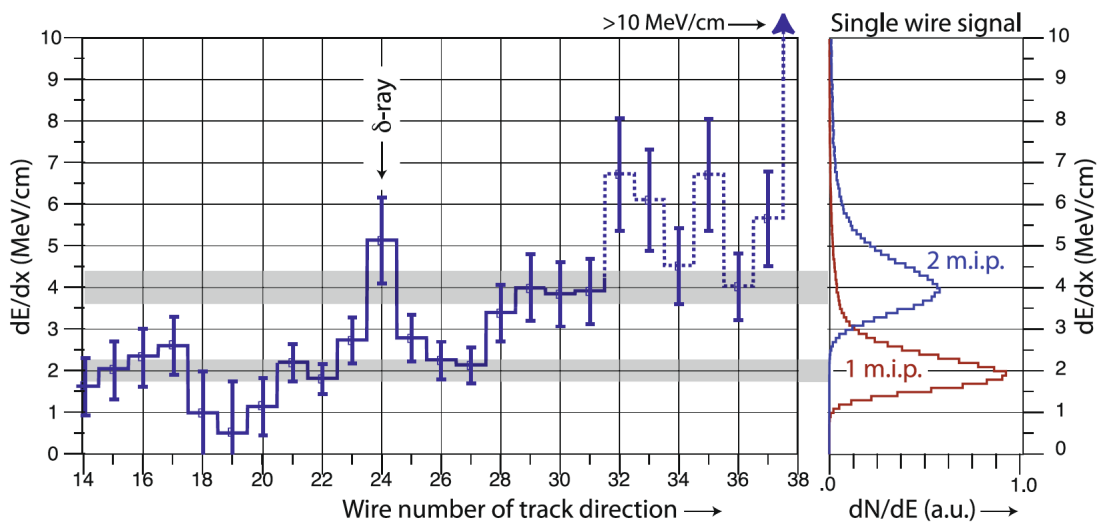


Figure 2.10: Display of the actual dE/dx along individual wires of the electron shower shown in Fig. 2.9, in the region ≥ 4.5 cm from primary vertex, where the track is well separated from other tracks and heavily ionizing nuclear prongs. As a reference, the expected dE/dx distribution for single and double minimum ionizing tracks are displayed and the dE/dx evolution from single ionizing electron to shower is shown.

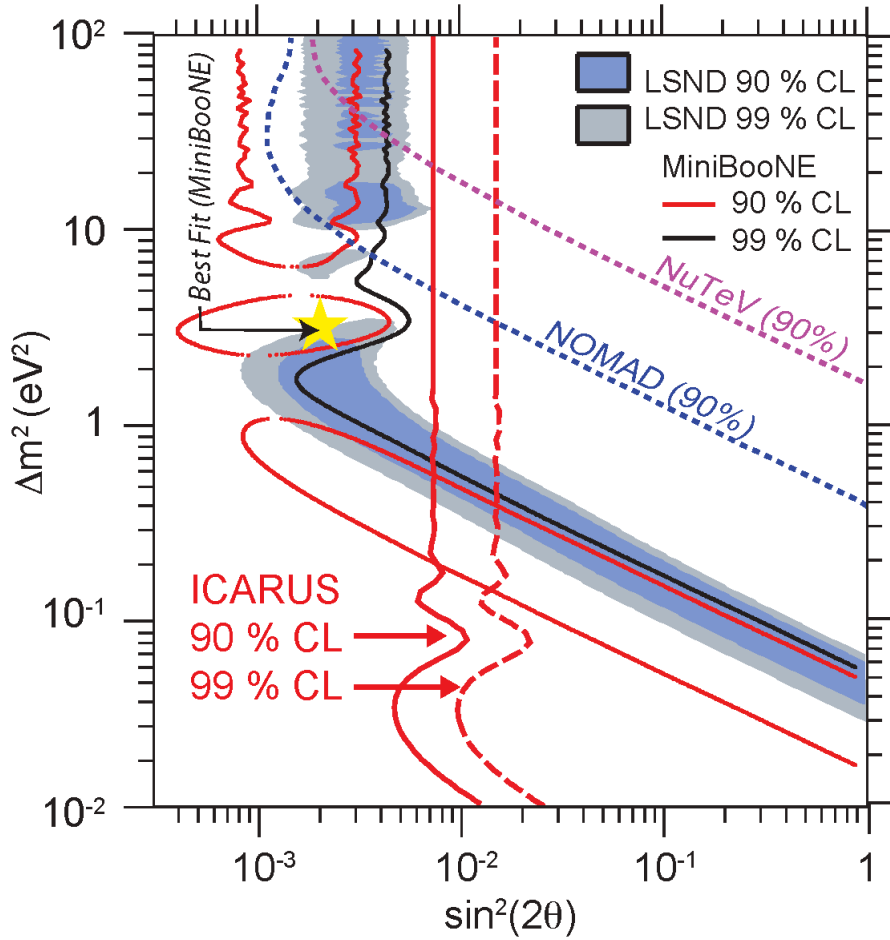


Figure 2.11: Two dimensional plot with Δm^2 as a function of $\sin^2(2\theta)$ for the main experiments sensitive to the $\nu_\mu \rightarrow \nu_e$ anomalies and for the present ICARUS result (continuous red lines). The ICARUS limit on the $\nu_\mu \rightarrow \nu_e$ oscillation probability are $\langle P(\nu_\mu \rightarrow \nu_e) \rangle \leq 3.92 \times 10^{-3}$ and $\langle P(\nu_\mu \rightarrow \nu_e) \rangle \leq 7.83 \times 10^{-3}$ at 90% and 99% CL.

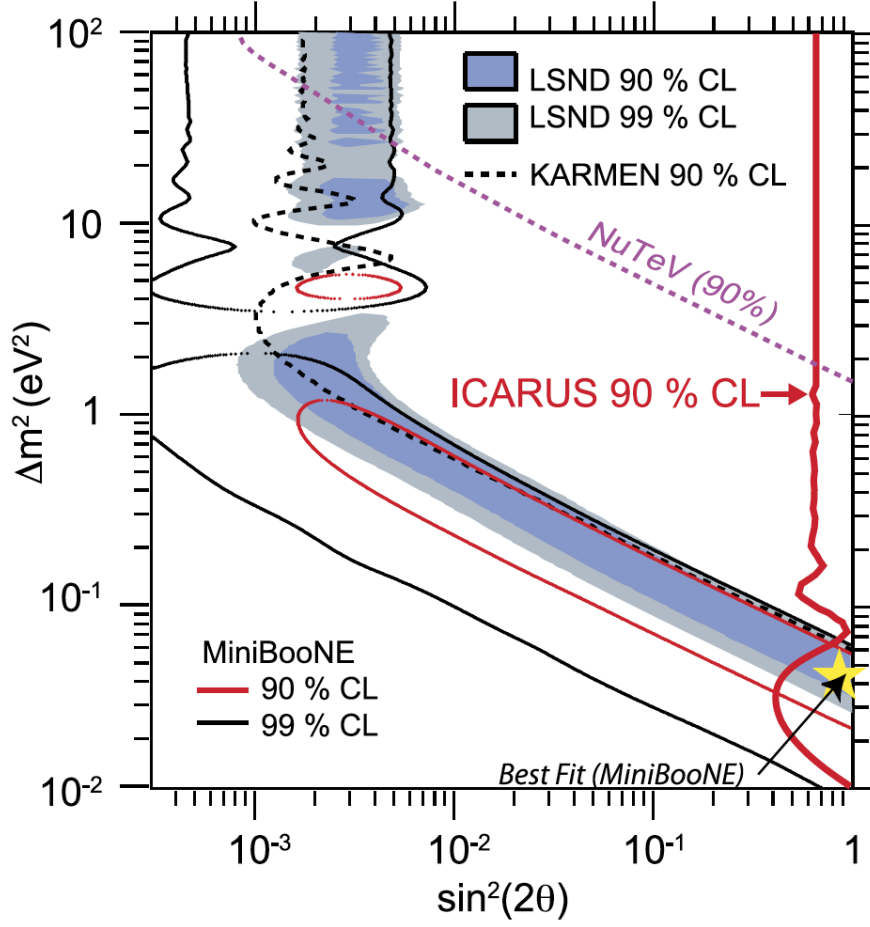


Figure 2.12: Two dimensional plot with Δm^2 as a function of $\sin^2(2\theta)$ for the main experiments sensitive to the $\bar{\nu}_\mu \rightarrow \bar{\nu}_e$ anomalies and for the present ICARUS result (continuous red lines). The ICARUS limit on the $\bar{\nu}_\mu \rightarrow \bar{\nu}_e$ oscillation probability is $\langle P(\bar{\nu}_\mu \rightarrow \bar{\nu}_e) \rangle \leq 0.32$ at 90% CL .

Chapter 3

Short Baseline Neutrino program

A new experimental phase of the ICARUS T600 detector will start with its transportation to the United States, at Fermi National Laboratory (FNAL). Here it will be part of two, consecutive in time, experiments: the first is the Short Baseline Neutrino (SBN) program and the second is the Deep Underground Neutrino Experiment (DUNE). This second experiment is a long time program, and it will be describe in chapter 6; in this chapter the SBN program and the role of the T600 detector will be explained.

SBN program scientific goal is a 5-sigma analysis of the possible sterile neutrino existence in the parameter space suggested by LSND (see Cap. 1). It is proposed to include three LAr-TPC detectors located on-axis in the Booster Neutrino Beam (BNB), as shown in Fig. 3.1. The near one (LAr1-ND) will be located at 110 m from the BNB target while the MicroBooNE apparatus will be located at 470 m. The far detector will be the improved ICARUS-T600, located at 600 m from the BNB target. The different locations have been chosen to optimize sensitivity to neutrino oscillations and to minimize the impact of flux systematic uncertainties [59]. A summary of the three locations and masses can be found in Table 3.1.

After a brief description of the BNB beam and a presentation of the two smallest detectors, the ICARUS refurbishing will be exposed.

Detector	Distance from BNB Target	LAr Total Mass	LAr Active Mass
LAr1-ND	110 m	220 t	112 t
MicroBooNE	470 m	170 t	89 t
T600	600 m	760 t	476 t

Table 3.1: Summary of the SBN detector locations and masses (total LAr masses and active ones).

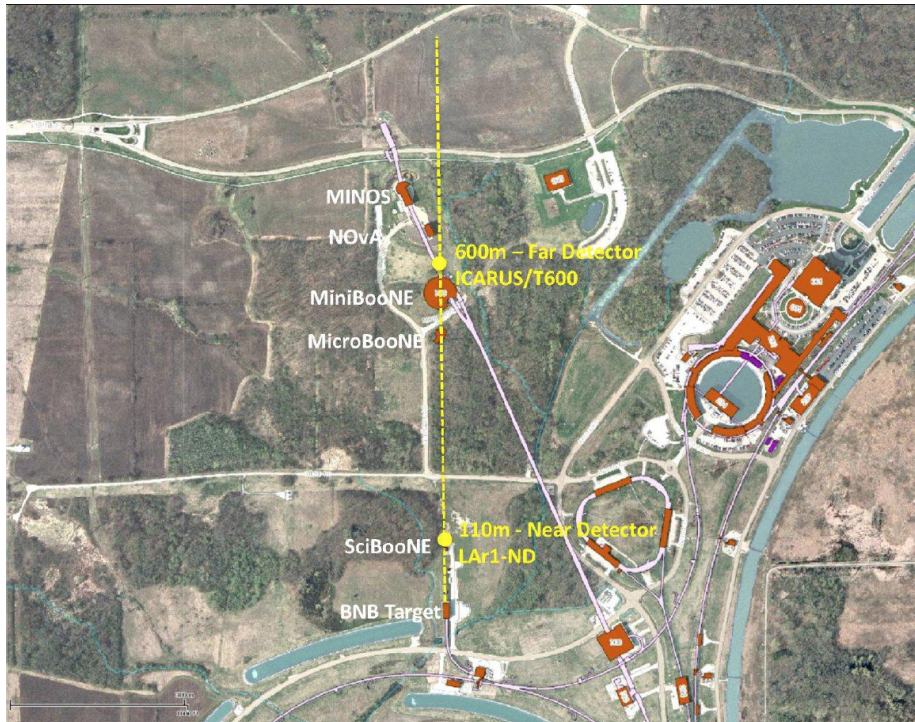


Figure 3.1: Map of the Fermilab neutrino beam line area showing the axis of the BNB (yellow dashed line) and approximate locations of the SBN detectors at 110 m, 470 m and 600 m. The pink line indicates the axis of the NuMI neutrino beam for reference.

3.1 The Booster Neutrino Beam

The Booster Neutrino Beam is created by extracting protons from the Booster accelerator at 8 GeV kinetic energy and 8.89 GeV/c momentum, and impacting them on a 1.7λ beryllium target to produce a secondary beam of hadrons, mainly pions. Charged secondaries are focused by a single toroidal aluminum alloy focusing horn that surrounds the target. The horn is supplied with 174 kA in 143 μs pulses coincident with proton delivery. The horn can be pulsed with either polarity, thus focusing either positives or negatives and de-focusing the other. Focused mesons are allowed to propagate down a 50 m long, 0.91 m radius air-filled tunnel where the majority will decay to produce muon and electron neutrinos. The remainder are absorbed into a concrete and steel absorber at the end of the 50 m decay region. Suspended above the decay region, at 25 m, are concrete and steel plates which can be deployed to reduce the available decay length, thus systematically altering the neutrino fluxes. The Booster spill length is 1.6 μs with nominally $\sim 5 \times 10^{12}$ protons per spill delivered to the beryllium target. The main Booster RF is operated at 52.8 MHz, with 81 buckets filled out of 84. The beam is extracted into the BNB using a fast-rising kicker that extracts all of the particles in a single turn. The resulting structure is a series of 81 bunches of protons each ~ 2 ns wide and

19 ns apart. While the operating rate of the Booster is 15 Hz, the maximum allowable average spill delivery rate to the BNB is 5 Hz, set by the design of the horn and its power supply.

The composition of the flux in neutrino mode (focusing positive hadrons) is energy dependent, but is dominated by ν_μ ($\sim 93.6\%$), followed by $\bar{\nu}_\mu$ ($\sim 5.9\%$), with an intrinsic $\nu_e/\bar{\nu}_e$ contamination at the level of 0.5% at energies below 1.5 GeV. Neutrino energy is peaked at ~ 1 GeV, with tail till to 3 GeV. The majority of the ν_μ flux originates from pion decay in flight, except above ~ 2 GeV where charged kaon decay is the largest contributor. A substantial portion of the intrinsic ν_e flux, 51%, originates from the pion to muon decay chain, with the remaining portion from K^+ and K^0 decays [59].

3.2 LAr1-ND

The Liquid Argon Near Detector, or LAr1-ND, will house a CPA (Cathode Plane Assembly) and four APAs (Anode Plane Assemblies) to read out ionization electron signals (see Fig. 3.2). The active TPC volume will be 4.0 m \times 4.0 m \times 5.0 m, containing 112 tons of LAr. The two APAs located near the beam-left and beam-right walls of the cryostat will each hold 3 planes of wires with 3 mm wire spacing. TPC signals will be read out with banks of cold electronics boards at the top and two outer vertical sides of each detector half. The total number of readout channels will be 2816 per APA (11264 in the entire detector). The CPA will have the same dimensions as the APAs and it will be centered between them. It will be made of a stainless-steel framework, with an array of stainless steel sheets mounted over the frame openings. Each pair of facing CPA and APA hence will form an electron-drift region. The open sides between each APA and the CPA will be surrounded by 4 FCAs (Field Cage Assemblies), constructed from FR4 printed circuit panels with parallel copper strips, to create a uniform drift field. The drift distance between each APA and the CPA will be 2 m, such that the cathode plane will need to be biased at -100 kV for a nominal 500 V/cm field. The LAr1-ND design will additionally include a light collection system for detecting scintillation light produced in the LAr volume [59].

3.3 MicroBooNE

The Micro Booster Neutrino Experiment (MicroBooNE) detector is a 170 ton total mass (89 ton active mass) LAr TPC contained within a conventional cryostat. It started the data taking in August 2015, like stand alone detector, to verify the excess of ν_e induced events in LNSD and MiniBooNE data.

The active region of the TPC is a rectangular volume of dimensions 2.33 m \times 2.56 m \times 10.37 m (see Fig. 3.3). The TPC cathode plane forms the vertical boundary of the active volume on the left side of the detector when viewed

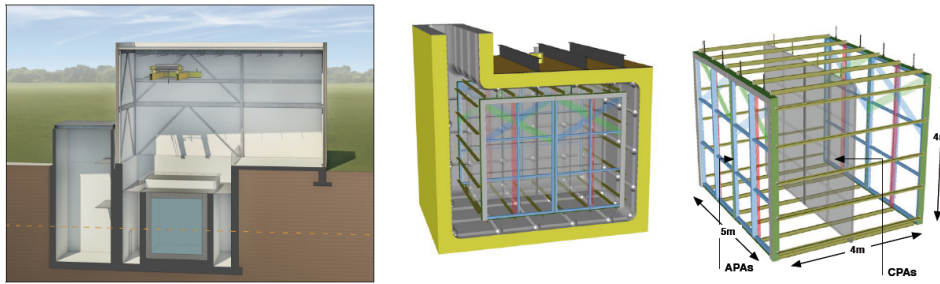


Figure 3.2: (Left) The LAr1-ND detector building concept. The neutrino beam center is indicated by the orange dashed line and enters from the left. (Right) The LAr1-ND TPC conceptual design.

along the neutrino beam direction (beam left side). The MicroBooNE TPC design allows ionization electrons from charged particle tracks in the active liquid argon volume to drift up to 2.56 m to a three-plane wire chamber. Three readout planes, spaced by 3 mm, form the beam right side of the detector, with 3456 wires arrayed vertically and two planes of 2400 wires oriented at ± 60 degrees with respect to vertical. An array of 32 PMTs are mounted behind the wire planes on the beam right side of the detector to collect prompt scintillation light produced in LAr. MicroBooNE is approved to receive an exposure of 6.6×10^{20} protons on target in neutrino running mode from the BNB. It will also record interactions from an off-axis component of the NuMI neutrino beam [59].

3.4 ICARUS T600 at FNAL

Once moved to FNAL the ICARUS T600 detector will be placed at a distance of 600 m from the target of the BNB, on-axis (see Fig. 3.4). It will also collect interactions from an off-axis component of the NuMI beam [59].

In the present configuration, as it worked at LNGS, the T600 detector is already well suited for sterile neutrino searches at FNAL. Nonetheless, it was designed for the low background, deep underground conditions of LNGS laboratory, where the single prompt trigger has always ensured the unique timing connection to the main image of the event. However, the situation will be substantially different for a detector of this magnitude if placed at shallow depth, i.e. a few meters deep with a 3m concrete cup to shield the soft cosmic radiation (see Fig. 3.5): several additional and uncorrelated tracks, due to cosmic rays, will be generally occurring continuously and at different times during the ~ 1 ms duration of the T600 readout window. This represents a new problem since, to reconstruct the true position of the track, it is necessary to precisely associate the different timings of each element of the image to their own specific delay with respect to the trigger.

The specific investigation of the oscillation anomalies at shallow depths is based

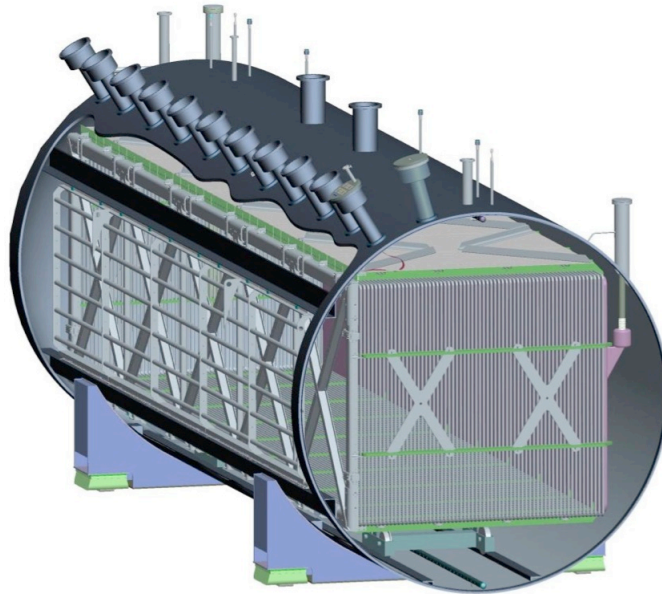


Figure 3.3: The MicroBooNE detector. The high-voltage feedthrough enters on the right and supplies the voltage for the cathode plane. One side of the field cage can be seen on the face of the cut-away (supported by the X braces). The sense and induction wires are on the right, and behind them is the support structure for the PMT array.

on the search of a signal with the presence of a neutrino-induced, single ionizing electron (or positron). High energy cosmic muons, creating secondary showers, may also produce single ionizing background electrons or positrons with similar energies. At the neutrino energies of the FNAL Booster Beam (\sim GeV), the intrinsic ν_e CC contamination occurs at the very low rate of $\sim 500 \nu_e$ CC/y, while a possible LSND-like oscillation signal will produce a few hundred ν_e CC/y. On the other hand the cosmic ray background is very prolific of events: in a pit covered by 3 m of concrete, i.e. the condition of T600 at FNAL, cosmic muon rates in coincidence with the beam trigger window of $1.6 \mu\text{s}$, will produce the huge rate of 0.83×10^6 cosmics per year (c/y) [59]. Moreover, during the 1 ms long duration of each readout window, ~ 12 cosmic ray tracks are expected over the full T600, in agreement with the ICARUS measurements at surface carried out in 2001 test run [50]. It can be concluded that in its original configuration the ICARUS LAr TPC detector can not perform a practical search for LSND-like anomalies at shallow depths, since the cosmic trigger events are too much frequent.

To overcome this problem, a complete overhauling of the ICARUS T600 detector is ongoing at CERN with the project name WA104 [59]. During this refurbishing, most of the existing operational equipment will be preserved, while some components with up-to-date technology are being upgraded in view of future non-underground operation. The refurbishing include the following

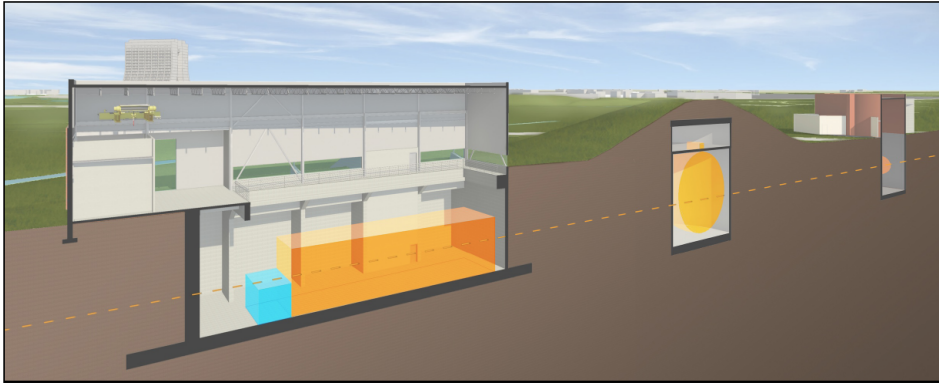


Figure 3.4: The ICARUS-T600 detector building concept (left building). The neutrino beam center is indicated by the orange dashed line and enters from the right. The existing MiniBooNE (right building) and MicroBooNE (central building) buildings are also shown.

main activities:

- implementation of a new light collection system, to allow a more precise event localization and disentangle beam events from the background induced by cosmic rays;
- implementation of new readout electronics;
- substitution of the present cathodes with new ones of improved planarity;
- other internal TPC updating: slow control system and cabling;
- realization of new vessels for LAr containment and new thermal insulation;
- complete review and maintenance of the cryogenics and purification systems.

The implementation of the new light collection system is the most demanding activity; the full description of the studies on its configuration and realization will be presented in details in the next two chapters. Other ongoing activities will be here briefly described.

3.4.1 TPC modifications

For what concerns the T600 TPC internal structure, minor changes are being implemented. Small deviations from the linearity of the drift field have been found in the region close to the cathode plane on both modules. This is due to the not perfect planarity of the cathodes, owing to their pierced structure. Thus it has been decided to change the present cathodes with new ones of

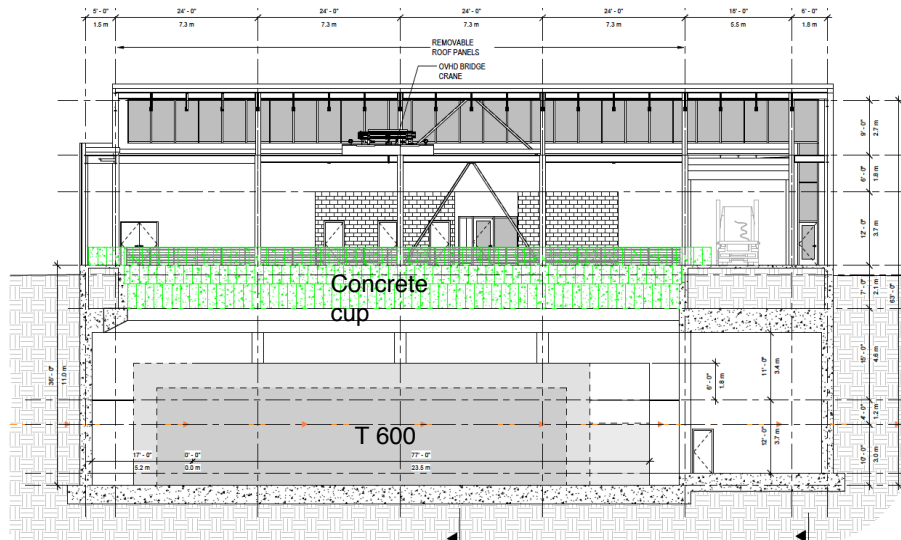


Figure 3.5: Scheme of ICARUS-T600 detector building. The 3 m concrete cup is enlightened in green. The neutrino beam center is indicated by the orange dashed line and enters from the left.

improved planarity, again transparent to the scintillation light. Other activities on the T600 TPCs concern the updating of the slow control system for temperature, pressure and cryostat wall deformation monitor, as well as the design of new cabling for internal wires, PMTs and slow control sensors [59].

3.4.2 New electronics

The preset ICARUS T600 electronics was designed starting from an analogue low noise warm front-end amplifier followed by a multiplexed (16 to 1) 10-bit AD converter and by a digital VME module that provided local storage, data compression and trigger information. The analogue front-end amplifier, used in the T600 LNGS configuration, is perfectly adequate: the only change will be the adoption of a smaller package for the BiCMOS custom amplifier, dual channel. A relevant change concerns the adoption of serial ADCs (one per channel) in place of the multiplexed ones used at LNGS. The main advantage is the synchronous sampling time (400 ns) of all channels of the whole detector. Performance, in terms of throughput of the read-out system, will be improved replacing the VME (8-10 MB/s) and the sequential order single board access mode inherent to the shared bus architecture, with a modern switched I/O. Such I/O transaction is carried over optical Gigabit/s serial links [59].

3.4.3 Trigger and DAQ

The trigger system of the T600 detector will exploit the coincidence of the prompt signals from the scintillation light in the LAr TPC, recorded by the PMT system, with the proton spill extraction of the BNB within a $1.6 \mu\text{s}$

gate. PMT digitized pulses will be sent to a front end dedicated board to be processed by FPGA modules, requiring a logic on multiple PMT signals for the generation of the trigger. The PMT trigger signal will be then sent to the T600 Trigger Manager, where it will be combined with the time information from the beam spill to initiate the readout of all the TPCs. A multi-buffer event recording will be adopted with a 3-level veto, as for the CNGS beam exploitation, able to give different priorities to different trigger sources, thus minimizing DAQ dead-time.

The system will consist of a Real Time (RT) controller and FPGA boards, communicating with the DAQ in handshake mode. The RT controller will monitor the number of available buffers in the digital boards, preventing the generation of new triggers in case they are full. The FPGA boards will implement time critical processes, like the opening of Booster Beam gate and the time stamp of each trigger. FPGA boards are also expected to record the trigger source and mask, to monitor the trigger rates and to control the overall system stability [59].

3.4.4 New cryogenic and purification systems

New cryostats will host the refurbished T600 detector. LAr will be contained in two mechanically independent vessels, of about 270 m³ each. They will be parallelepipedal in shape with internal dimensions 3.6 m × 3.9 m × 19.6 m. Aluminum welded extruded profiles will be used: they are requested to be high vacuum tight and to stand a 1.5 bar maximal operating internal overpressure. Use of aluminum LAr vessels is particularly attractive as it offers very good shielding against external electronic noises, and it provides large thermal conductivity that improves the temperature uniformity inside the LAr. Walls will be double-layered and with the possibility to be evacuated, leading to efficient leak detection and repair. The cold vessels will be enclosed inside a common heat exchanger (thermal shield) in which two-phase, gas and liquid, nitrogen will be circulated. As in the past run, a mass ratio less than 5:1 will be kept between the liquid and the gas phases, which ensures temperature uniformity all along the shield. A purely passive polyurethane foam is chosen for insulation, based on the membrane tanks technology. An insulation thickness of 600 mm will be used for the bottom and lateral sides; for the top-side a maximum thickness of about 400 mm will be used. With this configuration, the expected average thermal losses will be of around 10 W/m², resulting in a heat loss through the insulation of ~ 6.6 kW. All the external heat contributions (cables, pumps, transfer lines, etc.) can be accounted for a value not exceeding 5.4 kW, leading to a total heat load of about 12 kW. The scheme of ICARUS T600 cryogenics and LAr purification systems will be preserved, with the difference that the cooling circuit will be operated in open loop, instead of using re-liquefaction [59].

Chapter 4

New light collection system: Monte Carlo study

As previously explained, the future operation of the ICARUS LAr TPC on the FNAL BNB at shallow depth requires an improved light collection system, able to detect with full efficiency the prompt scintillation light from events with energy depositions down to ~ 100 MeV.

The renovated T600 photo-detector arrangement should again collect the VUV scintillation signal which is present in the LAr simultaneously to the ionization, converting it to visible light. The detection process in the LAr TPC is initiated by the trigger signal opening a long imaging readout window, in which tracks are recorded in a time sequence, collected serially by the readout planes, while the electrons travel towards the end of the drift path. The full image of the event is therefore progressively extracted from the drift time distributions and from the many readout wires. The scintillation light signal must be put in coincidence with the $1.6 \mu\text{s}$ beam trigger gate, giving the huge coincidence rate of $\sim 0.83 \times 10^6$ per year [59].

Moreover, during the long duration of each readout window, there will be on average 44 cosmic ray-induced scintillation light signals spread over the whole T600 [59]. This is two-plus-two times the number of the cosmic tracks collected in a drift time, two times because the time interval during which a light signal can be linked to a charge deposition is twice the maximum drift time and two times because the cathode is transparent.

The new light collection system has to be able to localize the track associated with every light pulse along the ~ 20 m of the longitudinal detector direction, with an accuracy better than 1 m, which is smaller than the expected average spacing between cosmic muons in each TPC image. In this way, the light collection system would be able to provide unambiguously the absolute timing for each track, and to identify, among the several tracks in the LAr TPC image, the event in coincidence with the neutrino beam spill.

MiniBooNE/SciBooNE collaborations were able to reconstruct the bunched beam structure of the BNB, lasting 1.15 ns (FWHM ~ 2.7 ns) every 19 ns [67].

The time accuracy of the incoming event with the new light collection system is expected to be at 1 ns level, allowing the exploitation of this bunched beam structure, to reject cosmic events induced triggers out of bunch [58]. An overall time resolution of 1.3 ns would then allow a background reduction of a factor ~ 4 by rejecting cosmic events occurring outside the RF buckets with a 2σ accuracy [59].

The Monte Carlo simulation produced to select the best PMT layout and the results obtained in terms of trigger definition, localization of events and their identification will be described in this chapter. The hardware tests carried out on the different components of the light collection system will be presented in the next one.

4.1 Monte Carlo simulation

A dedicated Monte Carlo simulation was realized in order to identify the best light collection system for the refurbished T600 detector. This simulation permits to study the performances of different PMT configurations, in order to select the most suited for the experiment purposes. The active volume of a single TPC ($18 \times 3 \times 1.5 \text{ m}^3$) is considered.

The simulation geometrical, very fast and performed with a series of C++ routines. Three different event topologies are considered:

- electromagnetic (e.m.) showers, that simulate NC and ν_e CC interactions;
- muons generated from ν_μ CC interactions;
- crossing cosmic muons, that represent the most important source of noise.

Fine details of physical events, such as e.m. shower shape or particle multiple scattering, are not taken into account, because they are on a smaller scale with respect to the light spatial resolution achievable with 10-20 cm diameter devices, spaced of ~ 0.5 -1 m.

Muons are schematized as straight line, while e.m events as clusters of points. Muons generated from ν_μ CC interactions are a superposition of the other two event topologies. From each simulated event point the photons originates isotropically; due to the short wavelength, LAr scintillation light is absorbed by all the detector material, so no reflection is assumed. Rayleigh scattering length of 90 cm is instead considered.

Muons are simulated as sequences of aligned points, 1 cm apart. Each of these points represents 2 MeV of deposited energy and 42k VUV photons start from it. These values of energy and emitted light are those measured for a m.i.p. interacting in LAr, with an electric field of 500 V/cm [40], that is the nominal electric field value in the T600. To take into account the presence of δ -rays, small e.m. clusters are generated randomly along the track, 1 every

4.1. Monte Carlo simulation

3 cm, within a 15 cm radius cylinder around the muon; they have random orientation, an energy ranging from 1 to 10 MeV and a spatial dimension proportional to the deposited energy. Muons are generated from both the upper and the lateral surfaces of the active volume, with a $\cos^2\theta$ distribution. No muons are simulated starting from less than 1 m from the bottom of the detector, due to the shallow depth condition. Muons propagates till they exit from the simulated volume. There are no cuts on the energy.

E.m. clusters are simulated as boxes of points, with a released energy of 1 MeV each. From every point, 21k VUV photons starts. Showers energy spans from 100 MeV to 1 GeV, to cover all the expected energy range in the SBN configuration [59]. Box dimensions are calculated in order to contain the 95% of a real event: as transversal dimensions two Moliere radius, energy independent and equal to 9 cm for LAr, are used, while as longitudinal dimension a parameter connected to the radiation length (14 cm in LAr) and increasing logarithmic with energy is utilized. The showers are generated uniformly in all the TPC active volume.

Muons generated from ν_μ CC interactions are simulated as a superposition of a muon, with the initial point generated uniformly in all the TPC active volume and random direction, and an e.m. shower, with energy ranging from 20 to 250 MeV and box centre coincident with the initial point of the muon. Muons have an energy ranging from 100 MeV to 1 GeV so they can stop also inside the TPC.

Both muons and e.m. showers present the same ratio between fast and slow component of the induced scintillation light ($c_f : c_s \simeq 1 : 3$). A third of the photons are so generated with $\tau = 7$ ns, while the remaining with $\tau = 1500$ ns. The arrival time of photons on a PMT is calculated from the distance between the emission point and the PMT, divided by the light velocity in LAr ($n_{Ar} \cong 1.22$ [66]); for the muons the additional particle transit time is also considered ($v_\mu \cong c$). An error of ± 1 ns on the arrival time is set to take into account the foreseen instrumental error.

PMTs are simulated as circles of different diameters on a lateral surface (plane zx) of the TPC volume, just in front of the LAr volume; the number of photons collected by every PMT is calculated according to the subtended solid angle. To take into account the systematic error, a $\pm 10\%$ uncertainty is simulated on the number of collected photons. A 5% overall Quantum Efficiency (Q.E.) is assumed for the PMTs; this values is in agreement with the experimental measurements (see chapter 5 and [42]). The value includes both TPB wavelength conversion efficiency and a geometrical factor due to the isotropic TPB emission. The effect of shielding on the light from the anode wires is not considered, because only the averaged result, i.e. a reduction of $\sim 15\%$ on the collected light can be computed. The consequence on the performed analysis will be however negligible: PMTs with $\sim 6\%$ of Q.E. permit to obtain the exposed results. The first PMT activated is the one that first collects 20 photons, i.e. 1 photoelectron (phe) with 5% of Q.E.. It has an

activation time set to 1 ns, and other PMTs are referred to it. No activated PMTs have activation time equal to 0 ns.

Different layouts were considered, with both 8" and 5" diameter window PMTs:

- A) 8" PMTs, 27 devices, 3 rows of 9 unit, 1.5% cathode coverage (present set-up of the East Module);
- B) 8" PMTs, 54 devices, 3 rows of 18 unit, 3% cathode coverage;
- C) 8" PMTs, 90 devices, 5 rows of 18 unit, 5% cathode coverage;
- D) 5" PMTs, 132 devices, 3 rows of 26 unit and 2 rows of 27 units, 3% cathode coverage;
- E) 5" PMTs, 210 devices, 7 rows of 30 unit, 5% cathode coverage.

The different configuration schemes are showed in Fig. 4.1. The cathode coverage represents the fraction of the wire plane surface covered by the PMT windows. The particular choice of the different layouts is due to the existing mechanical structure of the T600: the idea is not to change it, exploiting the free spaces already available. As shown in Fig. 4.2, it is quite easy to install PMTs till 90 8" devices (configuration C). Using instead 5" tubes, configuration with almost the same cost (D) and the same cathode coverage (E) have been exploited.

4.2 Event position reconstruction

First tests have been carried out to demonstrate the possibilities of the different configurations to localize the e.m. showers, mainly along the 18 m of the beam direction (z axis). The error on the event position reconstruction is calculated as the difference between the effective geometrical centre of the event and the one derived from the average on the PMT coordinates, weighted on the light collected by each PMT. For each configuration 10k e.m. showers are simulated. A reconstruction precision better than 1 m would reduce of a factor $\sim 1/20$ the number of light signal collected in a drift time, with a segmentation of the active volume in cells containing 1 or 2 tracks at most; this would allow the proper assignment of the time of occurrence (t_0) for every track.

As shown in Fig. 4.3, the distribution of the errors is not Gaussian in shape, so the full width at half of the maximum (FWHM) is used to evaluate the precision of the reconstruction. It can be seen that all configurations with a number of PMTs larger than the present set-up, show performances better than 25 cm.

The best results are obtained by the geometries with higher numbers of PMTs, but the difference are not so impressive. Besides, performance improvements can be also obtained just refining the reconstruction algorithm: just considering

4.2. Event position reconstruction

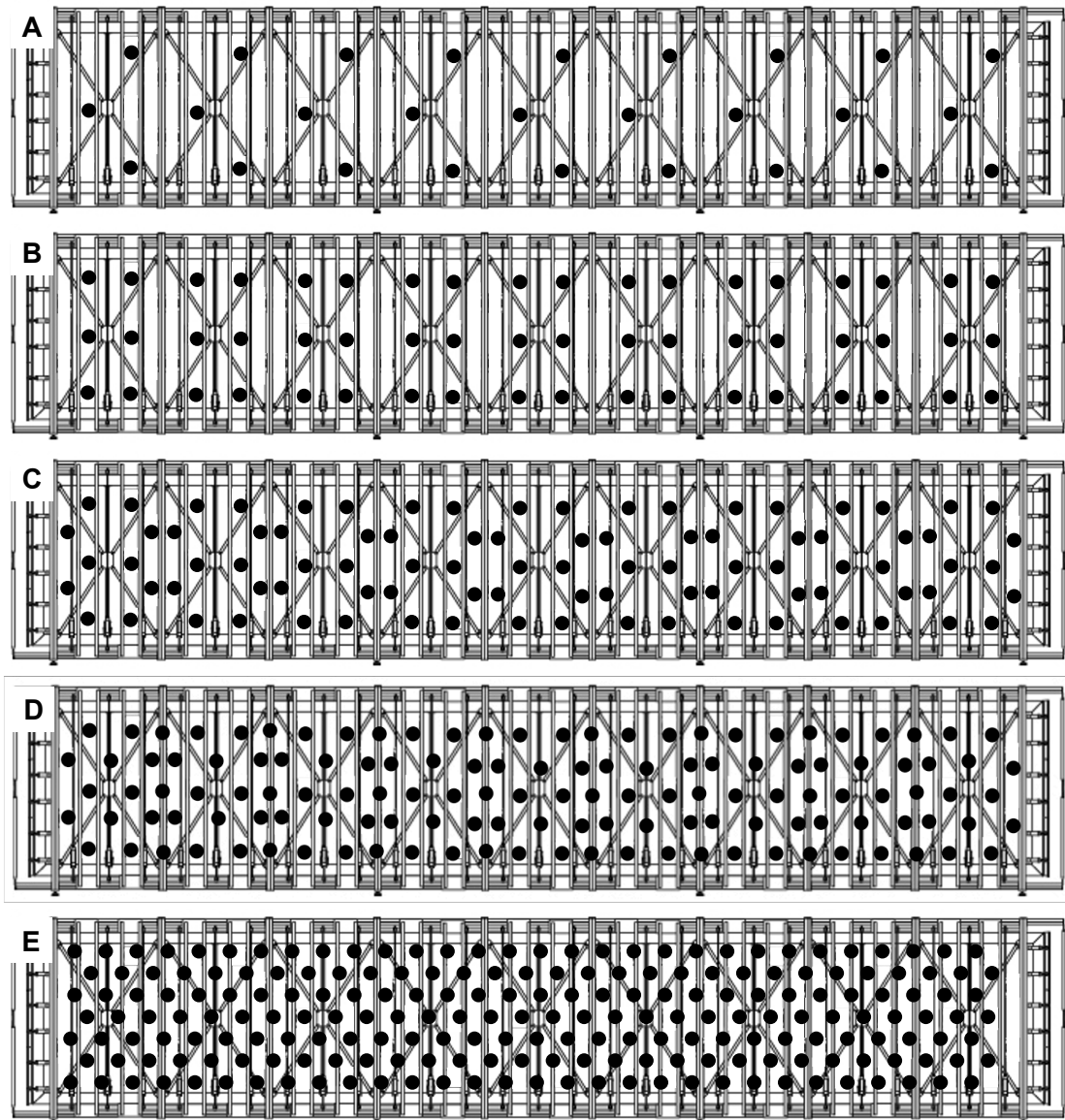


Figure 4.1: Drawings that show the different PMT layouts behind the wire planes. PMTs are depicted as dark circles.



Figure 4.2: Photo-edited image that shows the possibility to install till 90 8''-PMTs on the existing T600 mechanical structure, by adding further PMTs in addition to the existing ones (circled).

in the average on the PMT position only those devices with a signal above 10 phe, the 90 8''-PMTs configuration shows a localization capability which is better than the one obtained with the 210 5''-PMTs configuration (see Fig. 4.3). Thus, the layout with 90 8''-PMTs for each TPC is found adequate.

Events localized with an error exceeding 30 cm are verified (see Fig 4.4) to be events occurring near the limits of the sensitive volume. An increase of the number of PMTs does not improve the localization precision for these events. In fact, the not so good localization of this class of events is due to the finite extension of the PMT plane: for border events, a good fraction of the light emitted will be not collected by PMTs, thus moving the light-weighted coordinate towards the central regions of the detector.

Again the solution is an improvement of the reconstruction algorithm: in the configuration with 90 8''-PMTs, two columns of fake PMTs have been simulated on both sides of PMTs plane, next to the real ones. Signals equal to those of their specular real PMTs are assigned to the fake ones; they are then included in the reconstruction algorithm. As can be seen in Fig. 4.5, this improves the localization precision for the border events, leaving unaltered the central part of the error distribution. Events with a localization error greater than 30 and 60 cm are now the 5% and 0.8% respectively, to be compared with the 17% and 7% obtained without the fake PMTs.

The localization along the vertical direction (x axis) is also evaluated; it presents the same problem highlighted before, due to the finite extension of the PMT, and more pronounced. In this case, however, the solution is more

4.2. Event position reconstruction

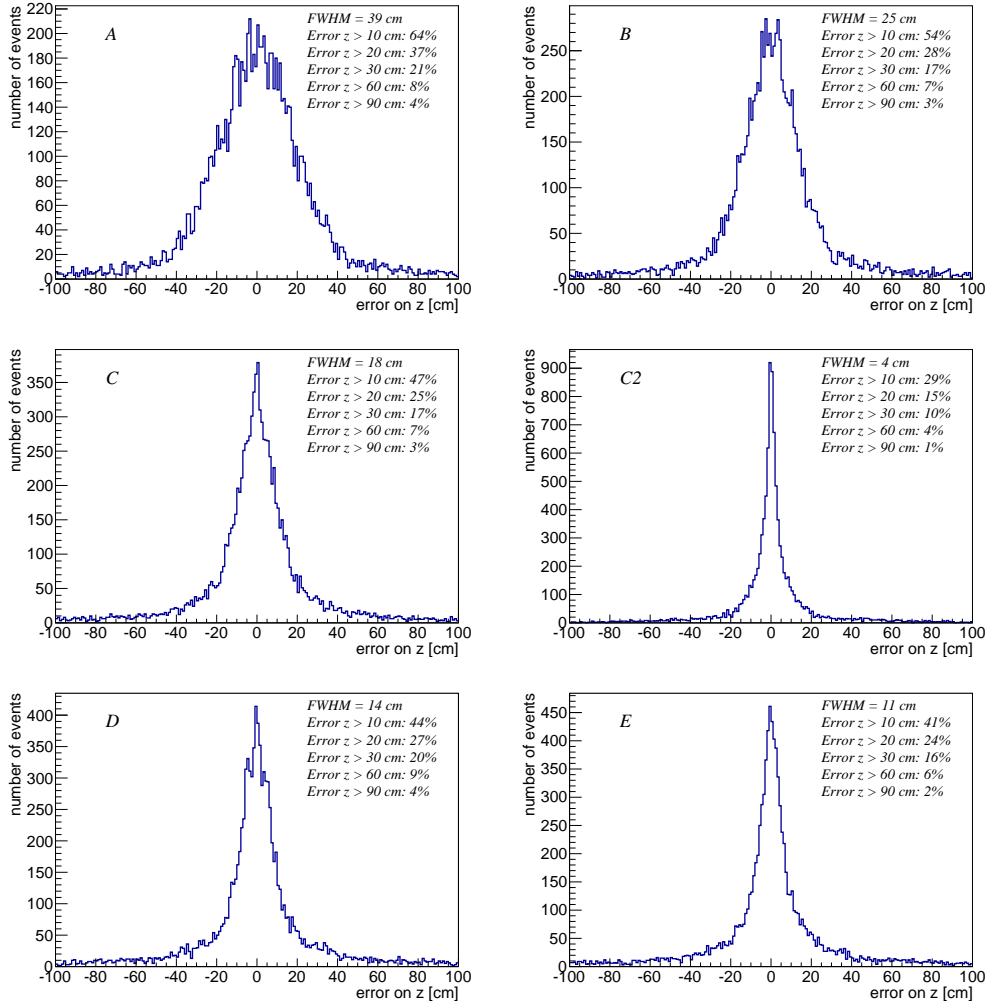


Figure 4.3: Evaluation of the precision on the localization of the correct position, along the beam direction z , for e.m. showers for the different PMT layouts. For the configuration C also the result obtained using only the PMTs with signal above 10 phe is shown (C2). The FWHM and the percentage of events localized with an error greater than 10, 20, 30 60 and 90 cm are indicated.

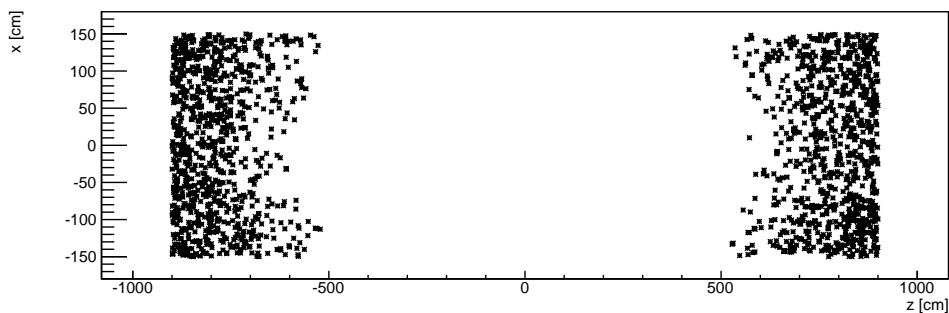


Figure 4.4: Actual position of the events localized with an error greater than 30 cm in the z direction.

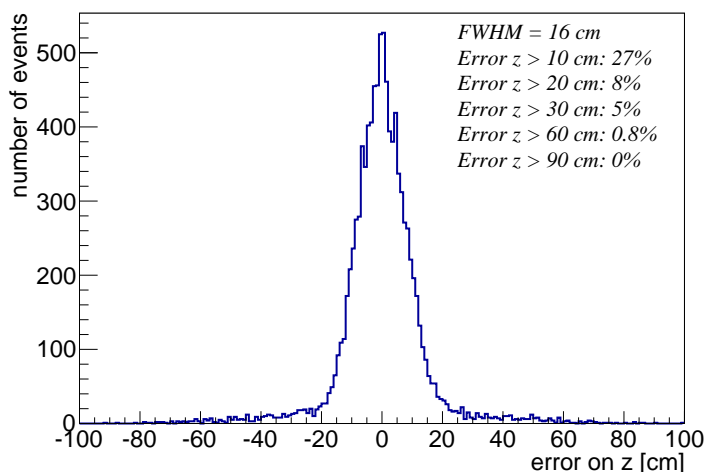


Figure 4.5: Evaluation of the precision on the localization of the correct position, along the beam direction z , for e.m. showers obtained with the fake PMTs algorithm. The FWHM and the percentage of events localized with an error greater than 10, 20, 30 60 and 90 cm are indicated.

straightforward: giving to PMTs a crescent weight going farther from the centre of the TPC, the improvement of the results, both in the central region and in the tail of the distribution, is evident (see Fig. 4.6).

All the presented results are obtained using both the fast and the slow component of the scintillation light. If only the fast component is considered, the precision of localization is only little affected, as can be seen in Fig 4.7.

Up to now PMTs have been considered as perfectly linear devices, with a signal proportional to the number of collected photons. However this is true only until a certain number of phe, depending on the PMT models. With devices linear up to ~ 400 phe, like those used in the previous phase of the ICARUS experiment [42], the possibility to obtain a good localization is ensured; however, if saturation occurs at the level of tens of phe (~ 30 -40 phe), the localization is seriously compromised. As an example the results obtained with saturation

4.3. Trigger definition

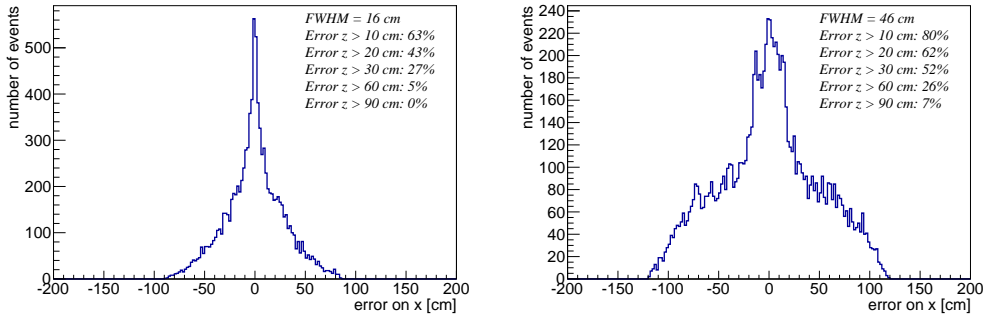


Figure 4.6: Evaluation of the precision on the localization of the correct position for e.m. showers, along the vertical direction x , with (left) and without (right) the PMTs weight correction. The FWHM and the percentage of events localized with an error greater than 10, 20, 30 60 and 90 cm are indicated.

occurring at 400 and 40 phe are shown in Fig. 4.8.

All the results reported before for the e.m. showers are valid also for the muons: for this kind of events, the localization is a bit less precise, due to their larger spacial development (see Fig 4.9). Muons generated from ν_μ CC interactions present the same characteristics than cosmic muons.

4.3 Trigger definition

The Monte Carlo simulation is also useful to give a first estimation of the trigger logic to be adopted in the experiment. The main purpose of any trigger system is to record all the physical events, discarding empty events produced by noise. In the future phase of the ICARUS experiment, the trigger will be given by a signal from the PMT system in coincidence with the beam gate. The idea is to start the trigger only if a certain number of PMTs gives a signal above a certain threshold, the value of which is sufficiently high in order not to collect low energy signal coming from ^{39}Ar background.

^{39}Ar is the main source of physical, i.e. not induced by the instrumentation, noise in a LAr TPC. It is a radioactive argon isotope that could produce an important noise due to beta-decay inside the sensitive volume. The measured activity of ^{39}Ar in LAr is 1.01 ± 0.08 Bq/kg of natural argon and a concentration of $(8.0 \pm 0.6) \times 10^{-16}$ g(^{39}Ar)/g(^{nat}Ar) is evaluated [65]; it is quite hard to further reduce such concentration in atmosphere-derived argon.

The decay of ^{39}Ar is a β^- decay, $^{39}\text{Ar} \rightarrow ^{39}\text{K} + e^- + \bar{\nu}_e$, with an end-point energy of 565 keV. ^{39}Ar induced events are simulated as point-like events, uniformly distributed in the active LAr volume, with an energy ranging from 100 keV to the end-point, according to the ^{39}Ar emission spectra. For the 81 m^3 ($1.5 \times 3 \times 18 \text{ m}^3$) of simulated LAr, a total activity of $\simeq 116$ kHz is calculated. As shown in Fig. 4.10, the probability that a noise event gives a signal above 2-3 phe in more than 2-3 PMTs is very low. On the contrary, the less intense

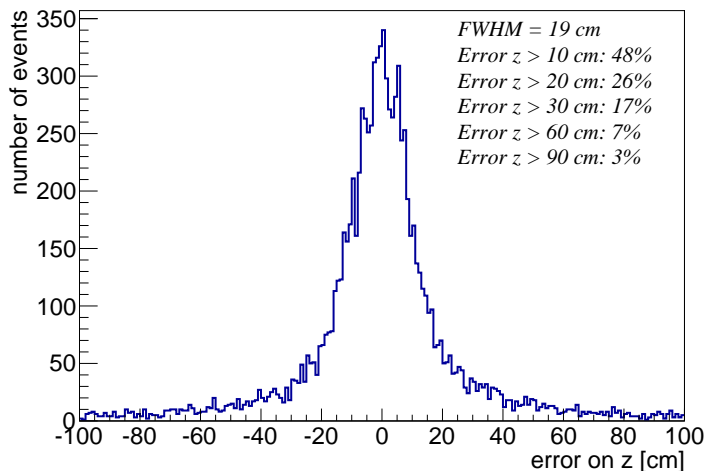


Figure 4.7: Evaluation of the precision on the localization of the correct position, along the beam direction z , for e.m. showers obtained using only the fast component of the light. The FWHM and the percentage of events localized with an error greater than 10, 20, 30 60 and 90 cm are indicated.

useful event class, i.e. 100 MeV events in proximity of the cathode, induces, with the 90 8''-PMTs layout, on more than 10 PMTs signal above 20 phe; the detection efficiency remains 100% for many combinations between PMT signal threshold and majority (see Fig. 4.11).

An estimation of the number of photo-electrons collected per MeV of deposited energy in a single TPC, gives an average value of about 15 phe/MeV, 9 phe/MeV for events close to the cathode.

4.4 Event identification

It would be very useful to fast discriminate between different event topologies, before the complete analysis of the wire collected charge. A preliminary discrimination, with the information obtainable from the light, will reduce the number of recorded events: if it would be possible to recognize the events triggered by cosmic muons, the amount of events to be analyzed will be greatly reduced. In order to understand if this classification can be performed with good success, the geometrical simulation previously described was used.

Each PMT unit provides, for each detected event, information about:

- the arrival time of the prompt photons: this can be derived, by interpolation, either by measuring the recorded signal leading edge, due to the fast component of the scintillation light, or by properly discriminating the PMT signal;
- the intensity of the light collected by the PMT, resulting from the fast component peak detection.

4.4. Event identification

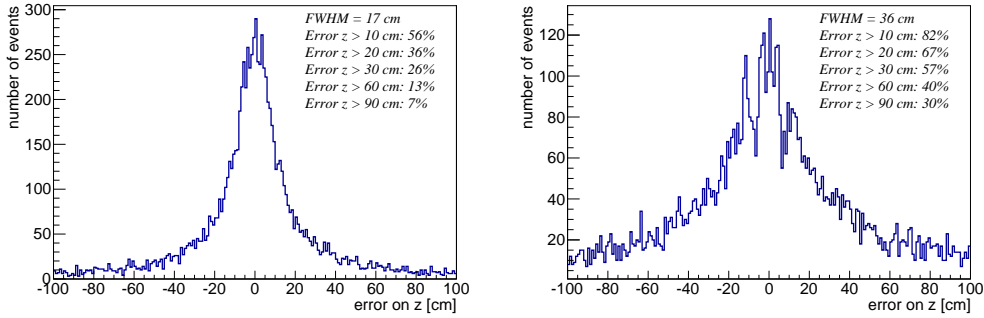


Figure 4.8: Evaluation of the precision on the localization of the correct position, along the beam direction z , for e.m. showers with PMTs saturation at 400 phe (left) and 40 phe (right). The FWHM and the percentage of events localized with an error greater than 10, 20, 30 60 and 90 cm are indicated.

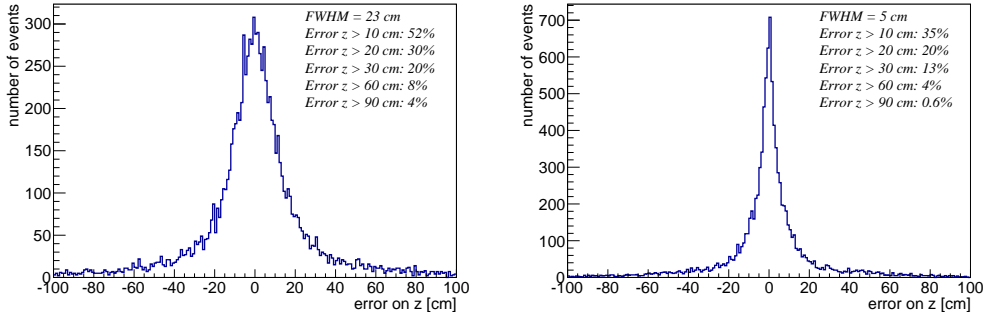


Figure 4.9: Evaluation of the precision on the localization of the correct position, along the beam direction z , with the 90 8''-PMTs layout, for muons, using all PMT signals (left) or only the PMTs with signal above 10 phe (right). The FWHM and the percentage of events localized with an error greater than 10, 20, 30 60 and 90 cm are indicated.

The use of the whole light collected, fast and slow component, is more difficult, due to the possible temporal superposition of the slow components of the different light pulses. Different event topologies present different characteristics, if seen in the parameter space given by arrival time and collected light intensity, as can be seen in Fig. 4.12.

Each event can be represented by a $2 \times N$ array, where N is the number of instrumented PMTs. In this way the identification of the event interaction class become a pattern recognition problem. Pattern recognition algorithms generally aim to provide a fast answer for all possible inputs and to perform "most likely" matching of the inputs, taking into account their statistical variation. Algorithms for pattern recognition depend on the nature of the problem; the present case falls in a particular class named "discriminative models" which include different learning methods, such as neural network. Artificial neural networks represent a common tool in high energy physics data analysis. They

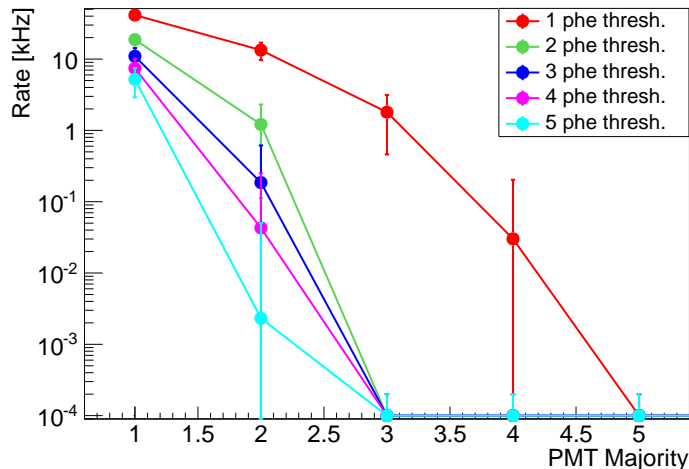


Figure 4.10: Residual ^{39}Ar rate as a function of the adopted phe threshold and PMT majority.

are included in the most common software packages, such as ROOT, whose implementation is based on the multilayers perceptrons (TMultiLayerPerceptron class).

The multilayer perceptron is a simple feed-forward network with the structure shown in Fig. 4.13. It is made of neurons characterized by a bias and weighted links between them, the so called synapses. The input neurons receive the inputs, normalize them and forward them to the first hidden layer. Each neuron in any subsequent layer first computes a linear combination of the outputs of the previous layer. The output of the neuron is then a f function of that combination, with f being linear for output neurons or a sigmoid for hidden layers.

To train this network there are different learning methods. The aim of all learning methods is to minimize the total error on a set of weighted examples. The network needs a number of test inputs with known output values, and it performs a series of learning on these training sets; each of these loops is called epoch.

Our neural network receives as input the information of light collected and arrival time from all PMT (90 $8''$ -PMTs layout). However, the use of all instrumented PMT, both activated or not, is useless or even damaging. At the same time, if only the activated PMT are used as input, the network must be trained with the PMTs coordinates also, doubling the initial input neurons without any advantages. Taking instead advantage of the precision obtained in the localization of events, it has been decided to divide the PMT plane in 8 different overlapping sections, 20 PMTs each. As it can be seen in Fig. 4.14, the PMT disposition is the same in all the sections, so that there is no need of the coordinates information.

The network inputs are then reduced from 180 (90 light collected + 90 arrival

4.4. Event identification

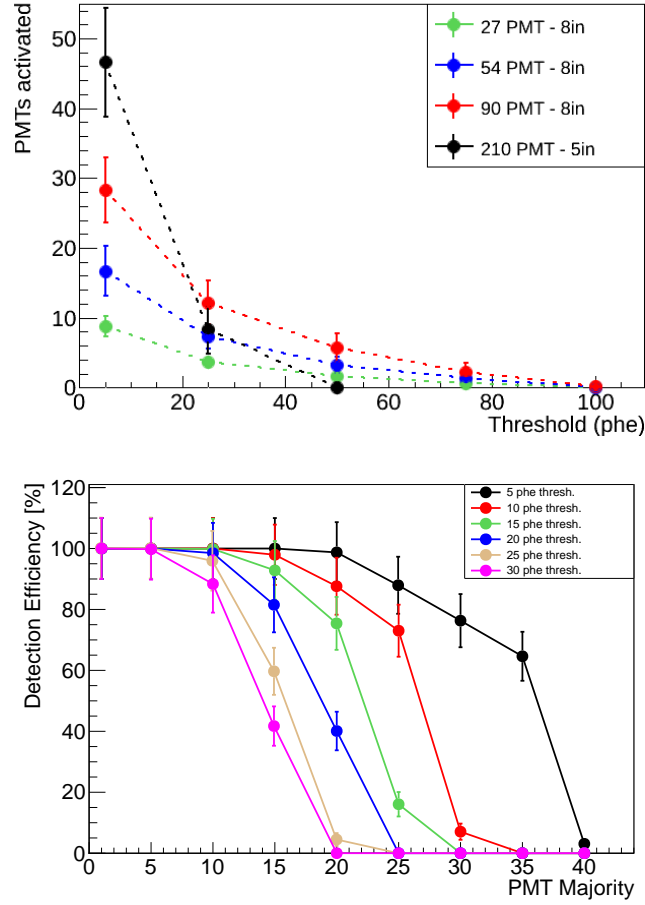


Figure 4.11: (Top) PMT activated from 100 MeV e.m. showers in proximity of the cathode, as a function of the adopted phe threshold, for the different PMT layouts. (Bottom) Detection efficiency for 100 MeV e.m. showers in proximity of the cathode, as a function of the phe threshold and PMT majority.

times) to 40, from the 20 PMT of the section where the event is localized in. Sections are 2 m wide to obtain an almost full containment of the events and are overlapping to avoid the presence of events in border zone between two sections. The network is designed as having 40 input neurons, two hidden layers, of 80 and 40 neurons each, and a single output. The output is binary: 1 means signal and 0 means background.

Network is trained with three different kind of events: crossing muons, e.m. shower, muons from ν_μ CC interactions. More precisely three networks have been developed, one for each physical event category. Each training is done on 10k signal events and 10k background events, with ~ 250 epochs. The number of epochs has been chosen by studying the evolution of the error as a function of the epochs. In this way three different function are obtained and each of them tries to recognize a different event topology:

- Crossing muons network: trained with 10k cosmic muons as signal, 5k

4. New light collection system: Monte Carlo study

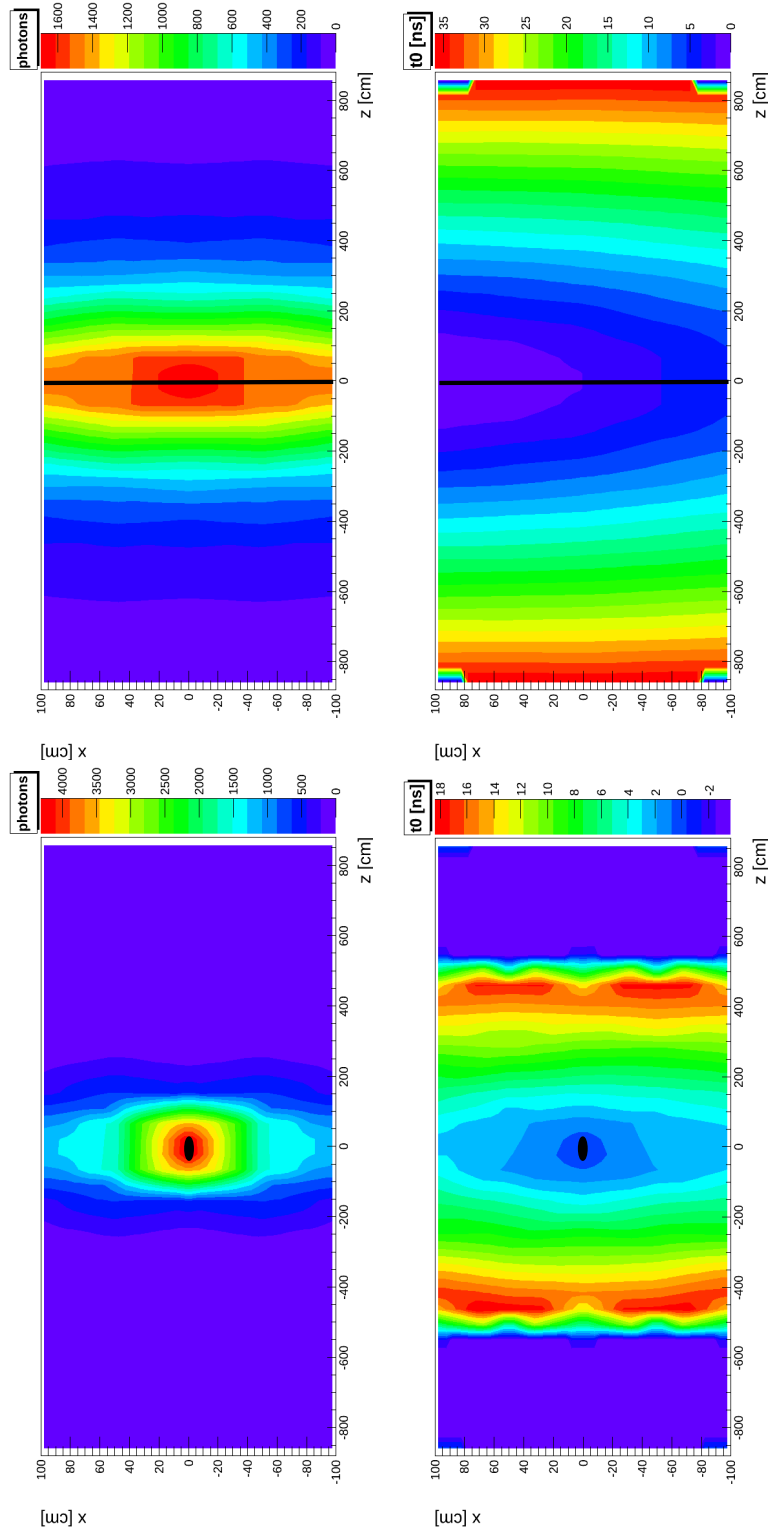


Figure 4.12: Light collected (left) and photons arrival time (right) patterns from a 200 MeV e.m. shower occurring in the centre of the TPC active volume (bottom) and for a vertical crossing muon again in the centre of the detector (top).

4.4. Event identification

e.m. showers and 5k ν_μ CC interactions as background. Setting 0.5 as threshold value, bad identified muons, i.e. with result <0.5 , are $\sim 4\%$, while misidentified noise, i.e. with result >0.5 , is $\sim 7\%$.

- E.m. showers network: trained with 10k e.m. showers as signal, 5k crossing muons and 5k ν_μ CC interactions as background. Setting 0.5 as threshold value, bad identified e.m. showers, i.e. with result <0.5 , are $\sim 11\%$, while misidentified noise, i.e. with result >0.5 , is $\sim 19\%$.
- ν_μ CC interactions network: trained with 10k ν_μ CC interactions as signal, 5k crossing muons and 5k e.m. showers as background. Setting 0.5 as threshold value, bad identified ν_μ CC interactions, i.e. with result <0.5 , are $\sim 19\%$, while misidentified noise, i.e. with result >0.5 , is $\sim 23\%$.

Results are shown in Fig. 4.17. The main purpose of the networks is the discrimination between cosmic muons and ν induced internal events: the results of 4% muons and 7% background misidentified is quite promising. Using the functions in sequence on each event, a better identification of the event topology can be obtained: defining a muon as an event with a result >0.5 for the muons network, <0.4 for the e.m. showers network and <0.25 for the ν_μ CC network, a misidentification of the level of $\sim 2\%$ is obtained.

These results demonstrate that the identification of events topologies using scintillation light information can be performed with good success. However a test has to be done with a full MC simulation, to understand if an event topology classification, performed with light information only, is realistically obtainable in the experiment. The full simulation will permit also to study a combined use of light and charge information: the most accurate and definitive particle identification will be always obtained with the charge collected by the TPC, but the light can accelerate this work and help to disentangle between overlapping events. The work on the neural networks is also ongoing, with the attempt of using dedicated software instead of ROOT packages.

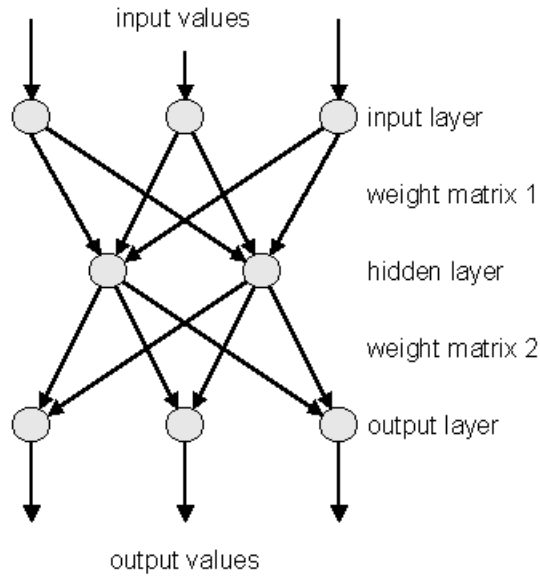


Figure 4.13: Schematic structure of a multilayer perceptron.

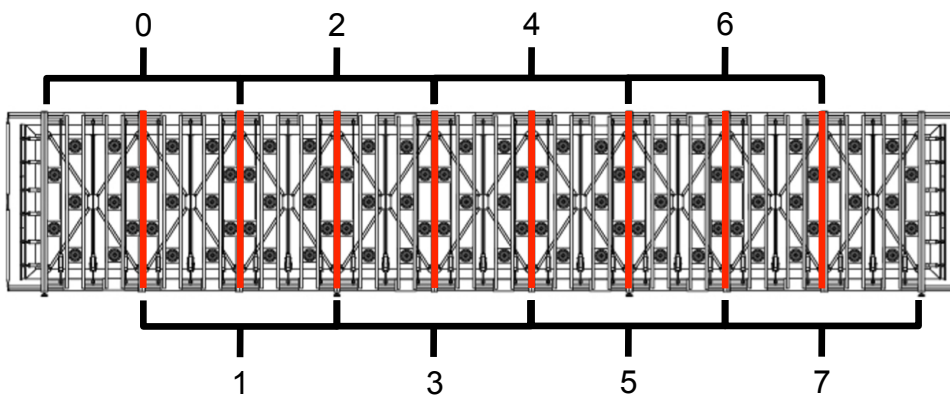


Figure 4.14: Subdivision of the PMT plane into 8 sections. Each section has the same PMT geometrical disposition. Red lines represent the centre of each section.

4.4. Event identification

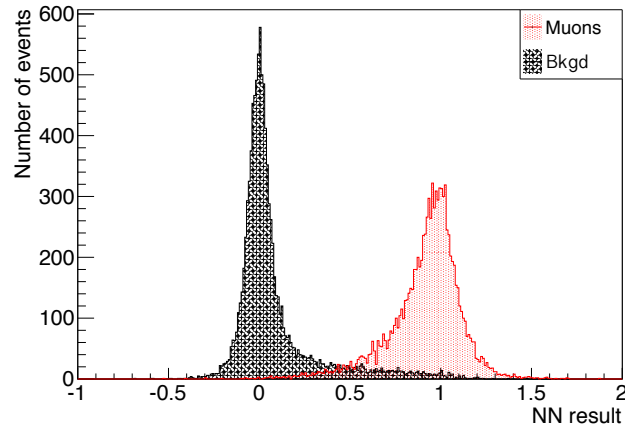


Figure 4.15: Result of the neural network trained with muons as signal. Setting 0.5 as threshold value, bad identified muons are $\sim 4\%$, while misidentified background is $\sim 7\%$.

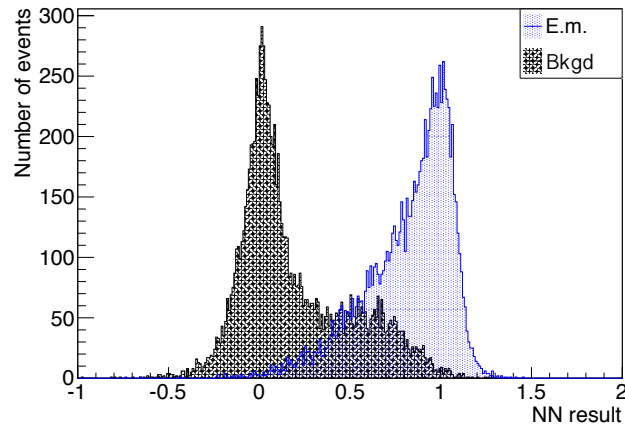


Figure 4.16: Result of the neural network trained with e.m. showers as signal. Setting 0.5 as threshold value, bad identified e.m. showers are $\sim 11\%$, while misidentified background is $\sim 19\%$.

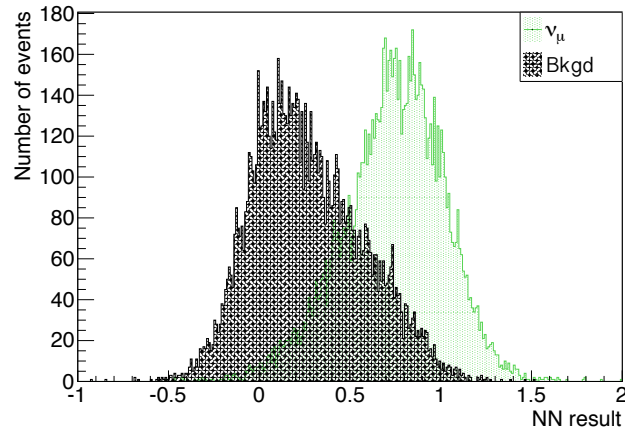


Figure 4.17: Result of the neural network trained with ν_μ CC interactions as signal. Setting 0.5 as threshold value, bad identified ν_μ CC are $\sim 19\%$, while misidentified background is $\sim 23\%$.

Chapter 5

New light collection system: hardware activity

As described in the previous chapter, the layout with 90 8"-PMTs permits a good localization of the events and also a preliminary event classification. However, to obtain these results, PMTs should present good performances in terms of cathode uniformity, signal linearity and temporal response. A set of defined characteristics are required to the PMTs to be installed in the T600 detectors:

- Dimension
 - Active window of 8" (20 cm) diameter.
 - Length fitting within the ICARUS detector mechanical structure (30 cm).
- Window
 - Glass window (borosilicate) with sand blasted surface.
 - Gauge pressure endurance above 5 bar at T=87 K.
- Photocathode type
 - Bialkali with platinum under-layer to properly operate at T=87 K.
 - Spectral response in the visible range (300-600 nm) with a peak Q.E. $\geq 15\%$ at room temperature.
 - Response deviations from uniformity lower than 10%.
- Mode of operation
 - Dynode stages to allow a gain $>10^7$ at cryogenic temperature.
 - 1700 V as max applied voltage for gain of 1.6×10^7 .

	R5912	R5912-02	ETL 9357 KFLB
Typical gain	10^7 at 1500 V	10^9 at 1700 V	10^7 at 1500 V
S.E. Rise Time	3.8 ns	4 ns	3.5 ns
TTS (FWHM)	2.4 ns	2.8 ns	4 ns
Transit time	55 ns	68 ns	65 ns
Dark current	50 nA	10^3 nA	10 nA
Q.E. at 390 nm	25%	25%	18%

Table 5.1: PMTs characteristics, from manufacturers data sheets.

- Single Electron Response (SER) peak-to-valley ratio higher than 2 for 10^7 gain.
- Response linearity up to 150 phe.
- Max dark count rate 5 kHz for 0.25 photoelectron threshold.
- Transit time spread better than 2.5 ns.

Tests carried on in order to choose the most suitable PMTs model and to reduce PMT induced noise on wire will be presented in section 5.1 and section 5.2. In section 5.3 brief descriptions of the foreseen acquisition system and time calibration system will be given.

5.1 Tests on PMTs

A set of tests were performed in order to choose the most suitable PMT model. Three new large area PMT models, Hamamatsu R5912 Mod and R5912-02 Mod, and ETL 9357 KFLB, have been characterized both at room and at cryogenic temperature [68][69]. Tested PMTs have, as requested, a 8" diameter window made of borosilicate glass and a bialkali photo-cathode (K_2CsSb) with platinum undercoating, in order to restore the photo-cathode conductivity at low temperature. Hamamatsu R5912 Mod and R5912-02 Mod PMTs have 10 and 14 dynodes, respectively, while the ETL 9357 KFLB has 12 dynodes. Their main characteristics, from manufacturer data sheets, are summarized in Table 5.1.

Temporal characteristics, photocathode uniformity, gain, linearity, dark count rate and Quantum Efficiency (Q.E.) for LAr scintillation light were evaluated.

For gain, linearity and uniformity measurements PMTs were illuminated with a 405 nm laser diode NICHIA NDV1413, using a pulse generator Avtech AVO-9A-C-P2-LARB and an optical fiber, 7 μ m core diameter, 3 m long. A proper support was used to maintain the fiber in a fixed orientation, normal to the PMT window, while allowing to move it in various positions on the window

itself. A pre-amp CANBERRA 2005 and an amplifier ORTEC-570 were used to form PMT signals, then acquired with a Multi Channel Analyzer (MCA) ORTEC-Easy-8k at 12 bit. For transit time and transit time spread (TTS) studies, PMTs signal passed through a Time-to-Amplitude-Converter (TAC) module, before being acquired by the MCA. The PMTs dark count rates were measured with a different acquisition system, i.e. with a discriminator CAEN V812 and a counter CAEN V560. The discrimination threshold was gradually increased from 1 to 255 mV, with 1 mV steps. Measures of signal shape and voltage peaks were carried out by means of a LeCroy WaveSurfer 44MXs-B oscilloscope (400 MHz, 2.5 GS/s).

To test PMTs at cryogenic temperature, they were directly immersed in liquid nitrogen ($T=77$ K), to obtain experimental conditions similar to those in the real apparatus. Measurements were carried out after ~ 3 days of rest in the cryogenic environment: this is the time necessary for the PMT characteristics to become stable [42]. The same set-up and acquisition system described before were used, with the fibre and the other cables allowed to enter by a proper feed-through, used to preserve darkness conditions and thermal insulation (see Fig. 5.1).

A different experimental setup was used to measure the Q.E. of the photocathodes in the VUV light region. In order to be sensitive to VUV light (LAr emission $\lambda=128$ nm), the PMT windows were coated with TPB, which presents isotropic emission and shifted light emission peak at 430 nm. The measured Q.E. is then the combination between the shifting efficiency of the TPB, a geometrical factor (at least half of the photons will be re-emitted in opposite direction with respect to the photocathode) and the Q.E. of the PMT for blue 430 nm light.

As shown in Fig. 5.2, the PMT under test was placed inside a steel chamber, optically connected to a VUV monochromator McPHERSON 234/302. The experimental setup included a scanner McPHERSON 789A-3, a Deuterium lamp McPHERSON 632, a rotating Al+MgF₂ mirror, a reference photo-diode AXUV-100 and collimating optics. The whole system was set under vacuum conditions, down to 10^{-4} mbar, to prevent ultraviolet light absorption. Thanks to the rotating mirror, the light spot was directed alternatively on the PMT surface or on the reference photo-diode. The Q.E. was obtained by comparing the current measured from the PMT with the same collected from the reference diode, keeping the illumination constant. Measurements were carried out by means of a picoammeter Keithley 6487E. The PMT signal was picked up directly from the photocathode, to have a gain equal to 1.

In the previous phase of the ICARUS experiment there was a single cable, connected at the anode, for both the PMT power supply and the collection of the signal. In order to avoid the use of decoupling capacitor, it was decided to use two cable, one for the high voltage, with negative bias and connected to the cathode, and one for the signal extraction, connected to the anode. The same scheme was used to test almost all the PMTs.

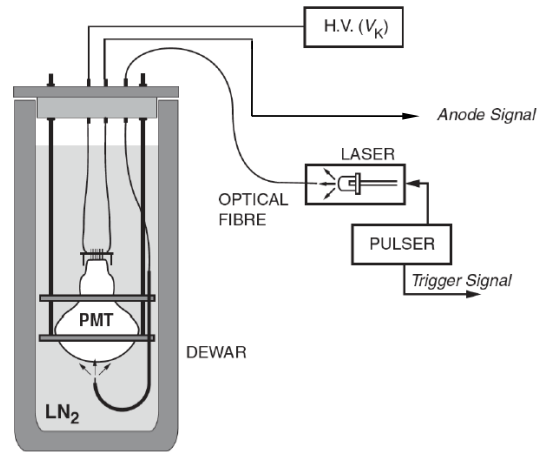


Figure 5.1: Experimental setup used for measurements at cryogenic temperature.

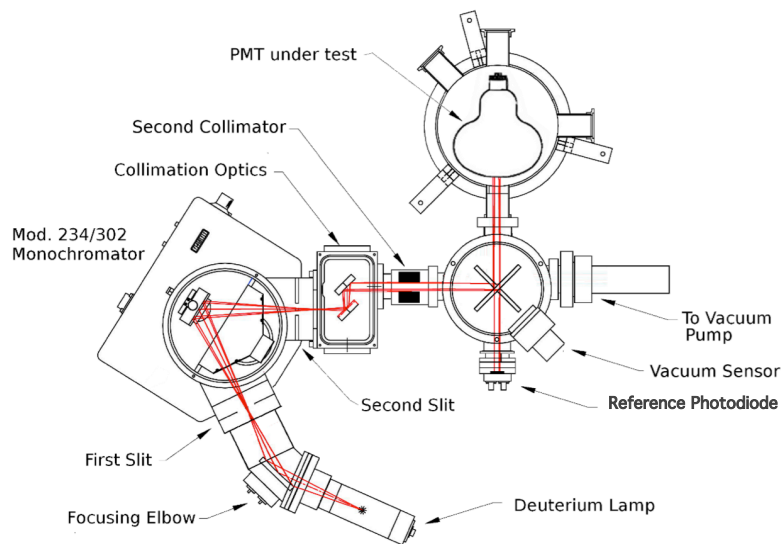


Figure 5.2: Experimental setup for the evaluation of the response of PMTs to the VUV light.

	R5912	R5912-02
Leading edge (ns)	3.8 ± 1.1	3.6 ± 0.9
Trailing edge (ns)	3.6 ± 1.2	3.5 ± 1.2
FWHM (ns)	4.4 ± 0.1	5.0 ± 0.8

Table 5.2: Leading edge, trailing edge and FWHM of Hamamatsu R5912 and R5912-02 at cryogenic temperature, measured in SER condition.

5.1.1 Hamamatsu R5912 Mod

Hamamatsu R5912 Mod is a 10 dynodes photomultiplier. To give the correct PMT biasing, cathode was set at negative HV, with anode grounded. The adopted voltage divider had the characteristics suggested by the manufacturer, with a total resistance of 20 M Ω (see Fig. 5.3). Measurements at room temperature were carried out with cathode at $V_c = 1450$ V, for a gain of 10^7 (see Fig. 5.4). Signal shape characteristics, measured at $T=77$ K, are reported in Table 5.2.

To test photocathode uniformity, Single Electron Response (SER) was studied, as a function of the position of the fibre along two perpendicular diameters. The mechanical support used for these measurements is shown in Fig. 5.5, while the results are presented in Fig. 5.6. The PMT shows a good uniformity, within 10%, till 10 cm from the tube axis, where a gain reduction occurs, probably due to the electric field non-uniformity in the peripheral region of the tube.

The same SER measurements were repeated with the PMT (parallel to the floor) in eight different orientations along the North, West, South, East directions, in order to study the dependence of the response on the Earth's magnetic field. Gain dependence is pronounced when fixing the fiber at the centre of the PMT window, up to 30%-35% (see Fig. 5.7), while electron transit time seems not to be affected by the Earth's magnetic field; its value is 55.1 ± 1.5 ns, compatible with what is reported by the manufacturer, when measured with the fiber in the centre of PMTs; it increases going further from the tube axis (see Fig. 5.8).

At cryogenic temperature, gain trend, linearity and dark rate counts were measured. Gain reduction, occurring with decreasing temperature and probably due to change of the resistances in the voltage divider, is evident: the gain at $T=77$ K is $\simeq 30\%$ of that at room temperature (see Fig. 5.4). However, an increase of 150 V in the power supply was sufficient to restore the nominal gain of 10^7 .

Linearity of the device was studied by illuminating its cathode with increasing light intensity. To perform this, a series of neutral density optical filters, calibrated with the same light used in the measurements and mounted

5. New light collection system: hardware activity

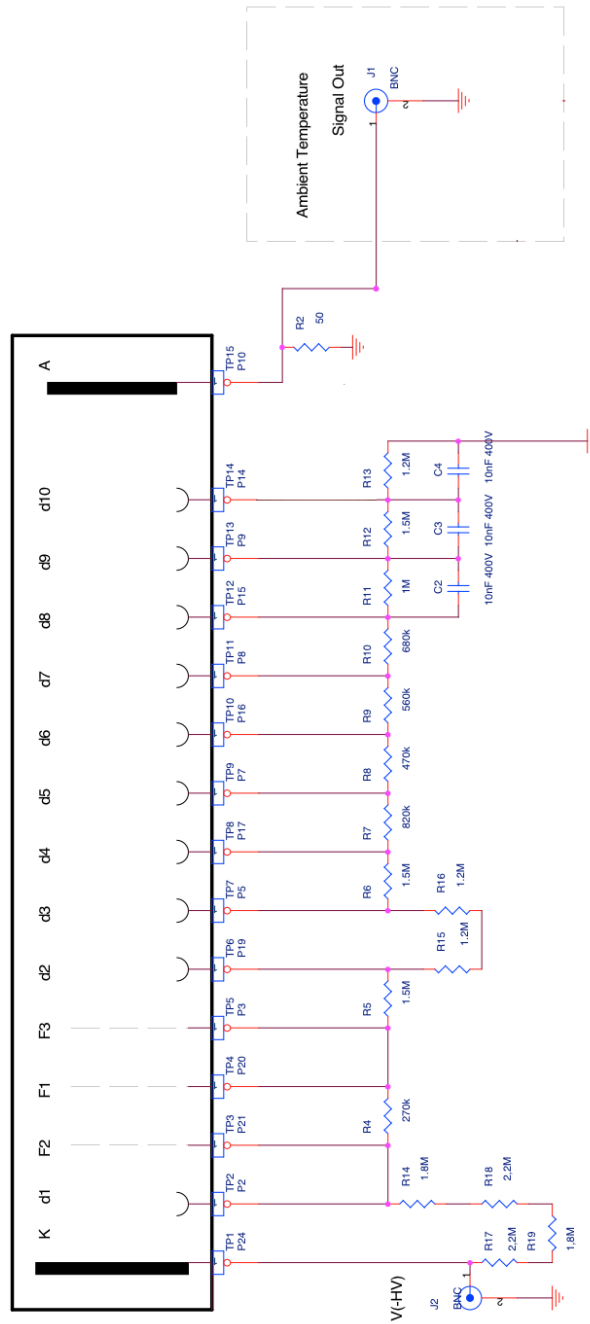


Figure 5.3: Voltage divider used to test the Hamamatsu R5912 Mod.

5.1. Tests on PMTs

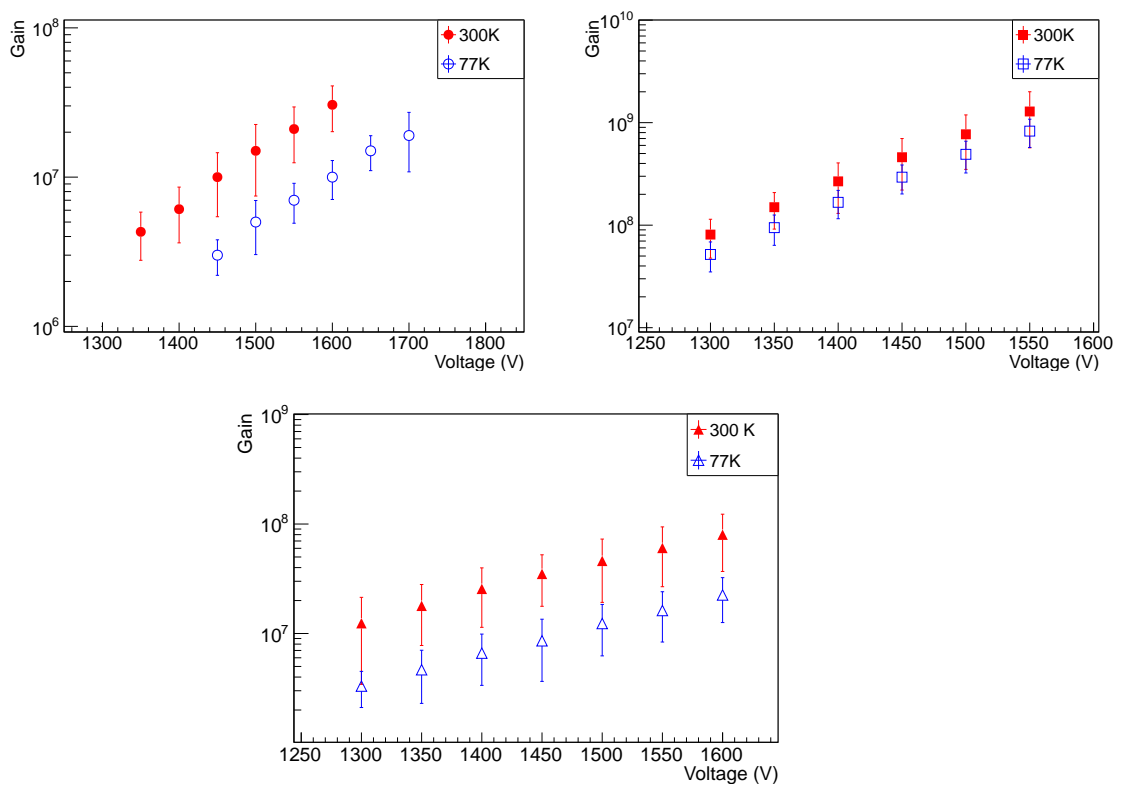


Figure 5.4: Gain trends for Hamamatsu R5912 Mod (left up), R5912-02 Mod (right up) and ETL 9357 KFLB (down) at room and cryogenic temperature.



Figure 5.5: Support system used for photocathode uniformity measurements.

Wheel 1	Wheel 2
11.0 ± 0.1	3.36 ± 0.04
31.9 ± 0.3	1.76 ± 0.02
109.9 ± 1.0	2.85 ± 0.30
	6.52 ± 0.06
	5515 ± 50

Table 5.3: Attenuation factors for 405 nm light of the used filters.

on two rotating supports (see Fig. 5.9), was used (see Tab. 5.3). Starting from the maximum attenuation it was possible to increase the illumination intensity and to study the linearity of the devices. Measurements were carried out with a pulsed light source (2 ns width) at a repetition rate of 20 Hz. Both the peak amplitude and the collected charge distribution were studied.

Hamamatsu R5912 Mod shows a very good linearity, up to 400 phe, both at room and at cryogenic temperature (see Fig. 5.10).

Dark count spectrum structure is characterized by a clear bump profile centered in the region around one photoelectron, caused mainly by the cathode dark noise. The rate increases with decreasing temperature; this is a well known effect, referred as non-thermal dark rate. While the source of this emission is found in the photocathode, its nature and features are not yet understood [70]: the reason could be ascribed to a decrease of the lattice-energy of the cathode material at low temperature, resulting in an increase of the electron escape probability [42]. For R5912 Mod dark count rate is rather high, both at room and cryogenic temperature, being ≥ 0.5 kHz till 0.7 phe of threshold and ≥ 2 kHz till 0.6 phe of threshold respectively (see Fig. 5.11). This increase should be lower for LAr, being the temperature higher than the LN_2 one.

A wavelength-dependent analysis, from 120 nm to 220 nm, was performed to measure the Q.E. of the PMT for VUV light (see Fig. 5.12); for LAr emission

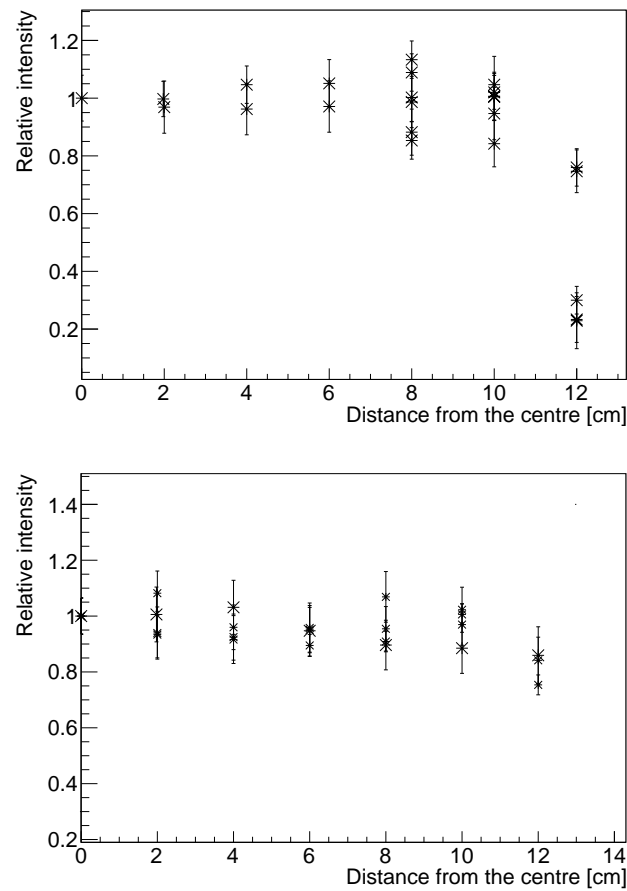


Figure 5.6: Relative response as a function of the distance from the centre of the window, along different diameters, for Hamamatsu R5912 Mod (up) and ETL 9357 KFLB (down). Several measurements were performed for each position: error bars represent the statistical errors.

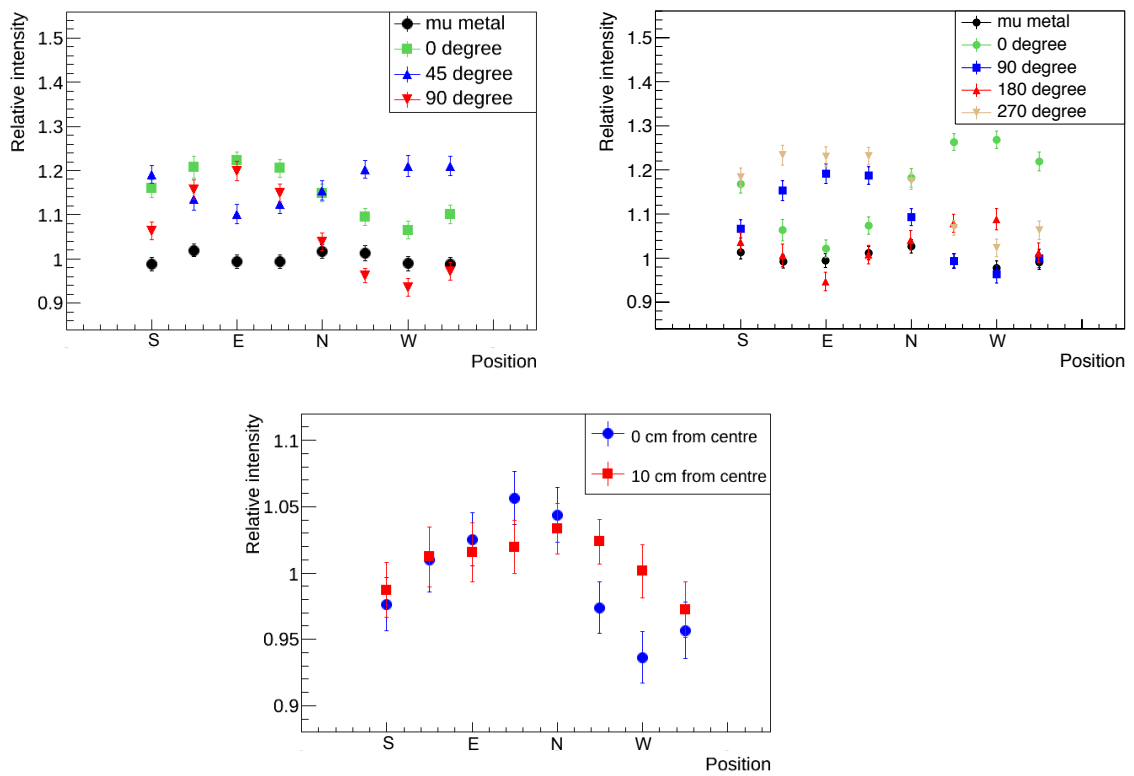


Figure 5.7: Relative response as a function of the orientation with respect to the Earth's magnetic field for Hamamatsu R5912 Mod (left up), R5912-02 Mod (right up) and ETL 9357 KFLB (down). The Hamamatsu PMTs were illuminated at the centre of the window, while ETL both at the centre of the window and 10 cm far from it.

5.1. Tests on PMTs

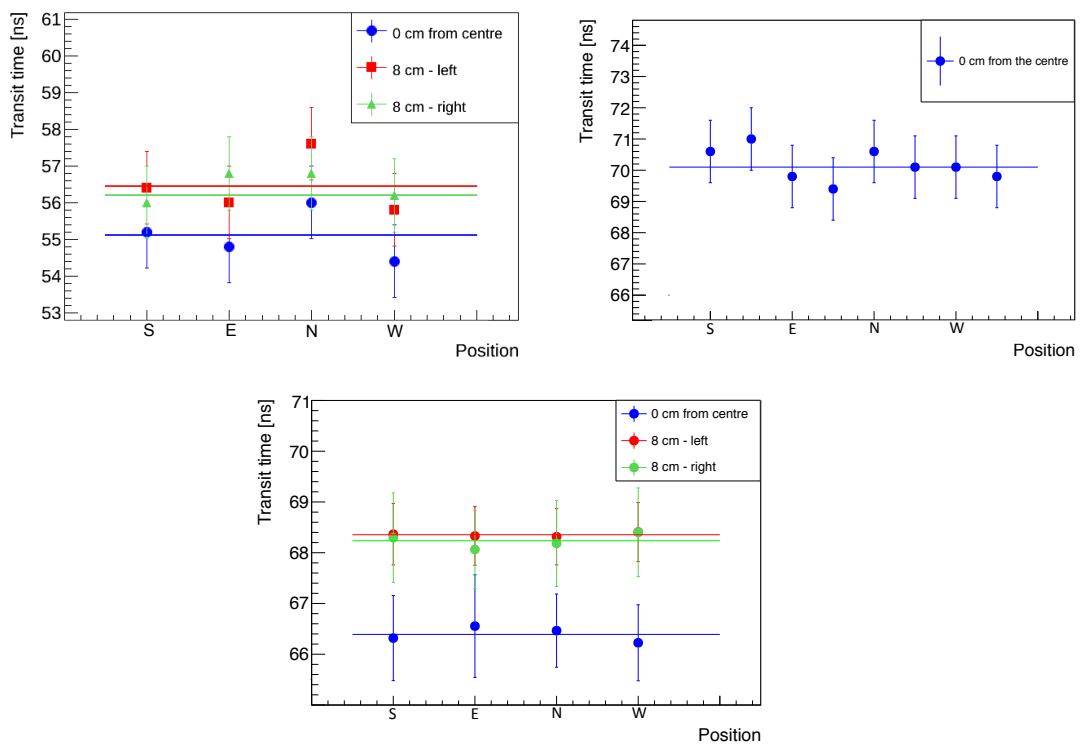


Figure 5.8: Electron transit time of Hamamatsu R5912 Mod (left up), R5912-02 Mod (right up) and ETL 9357 KFLB (down), as a function of the orientation with respect to the Earth's magnetic field.

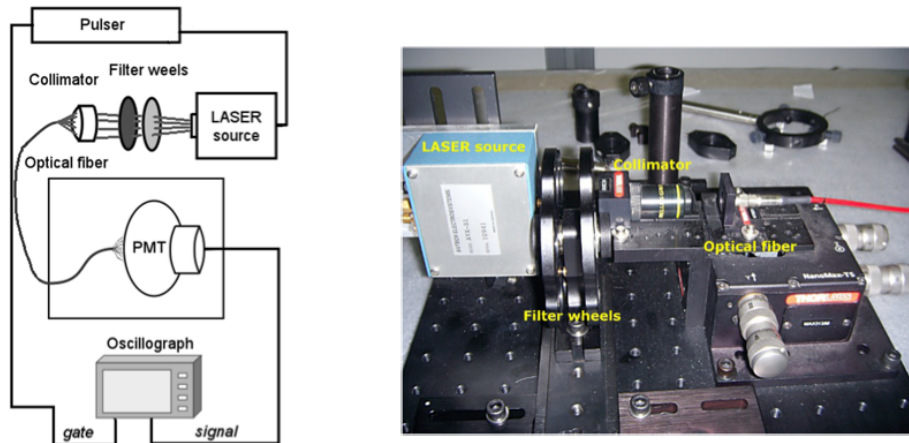


Figure 5.9: System for measurements of PMTs linearity. The acquisition system for the voltage mode measurements is also sketched.

peak, $\lambda = 128$ nm, Hamamatsu R5912 has Q.E. = $7.0\% \pm 0.6\%$.

5.1.2 Hamamatsu R5912 - 02 Mod

Hamamatsu R5912-02 Mod differs from R5912 Mod mainly for the number of dynodes, 14 instead of 10. The two PMT models have the same cathode structure, so photocathode uniformity and Q.E. present the same characteristics and values. The same power supply scheme used for R5912 was adopted. The voltage divider used, with a total resistance of $20 \text{ M}\Omega$, is shown in Fig. 5.13. Due to the high number of dynodes, Hamamatsu R5912-02 has a very high gain. Measurements at room temperature were carried out with cathode voltage $V_c = 1450 \text{ V}$, for a gain of $\sim 5 \times 10^8$ (see Fig. 5.4). Signal shape characteristics, measured at $T=77 \text{ K}$, are reported in Table 5.2.

Signal intensity dependence on the Earth's magnetic field is very pronounced (see Fig. 5.7), while the transit time, $70.1 \pm 2.0 \text{ ns}$, compatible with that same declared by manufacturer, seems to be not affected (see Fig. 5.8).

Gain decrease at cryogenic temperature is restrained, being the gain at $T=77\text{K} \simeq 70\%$ of that at room temperature (see Fig. 5.4); an increase of 50 V in power supply permitted to restore the gain of $\sim 5 \times 10^8$. The dark count rate is lower with respect to that of R5912 Mod, being lower than 0.4 kHz and than 2 kHz , at room and cryogenic temperature respectively, for all threshold values (see Fig. 5.11).

A big problem arose when studying the response linearity: both at room and at cryogenic temperature the PMT stops to be linear after $\sim 10 \text{ phe}$ (see Fig. 5.10). Same measurement was performed on other two devices of the same model, with the same result. This fact could seriously compromise the spa-

5.1. Tests on PMTs

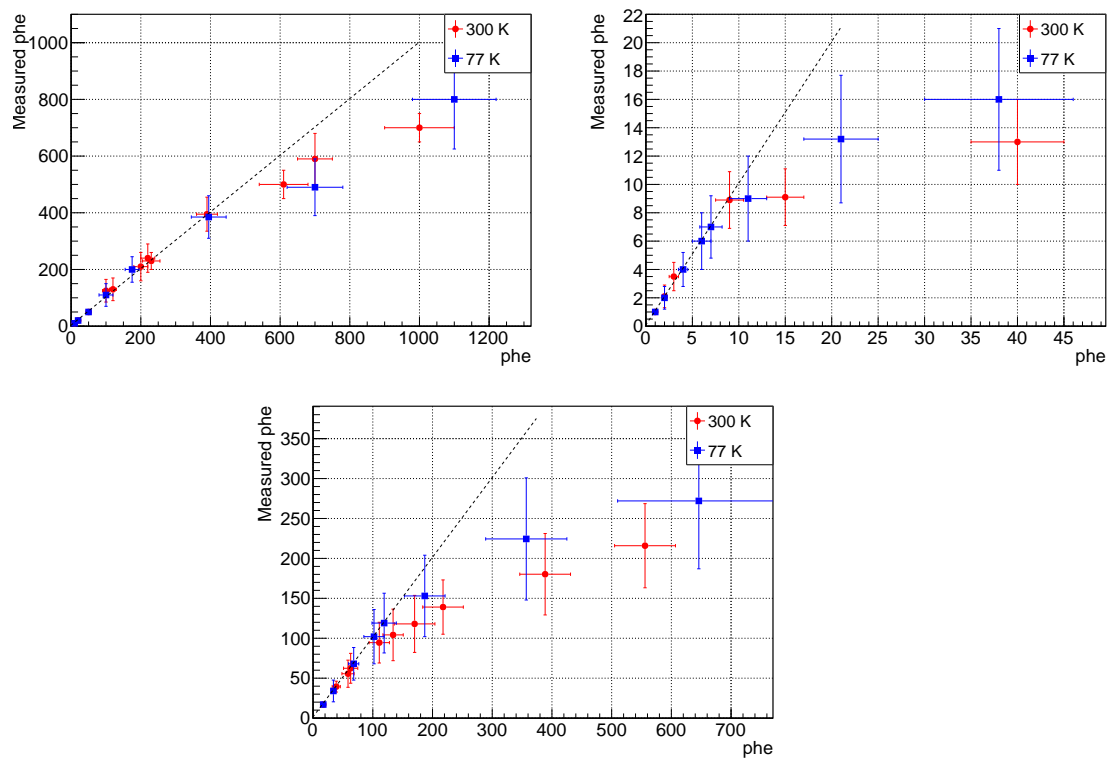


Figure 5.10: Linearity of Hamamatsu R5912 Mod (left up), R5912-02 Mod (right up) and ETL 9357 KFLB (down) at room and cryogenic temperature.

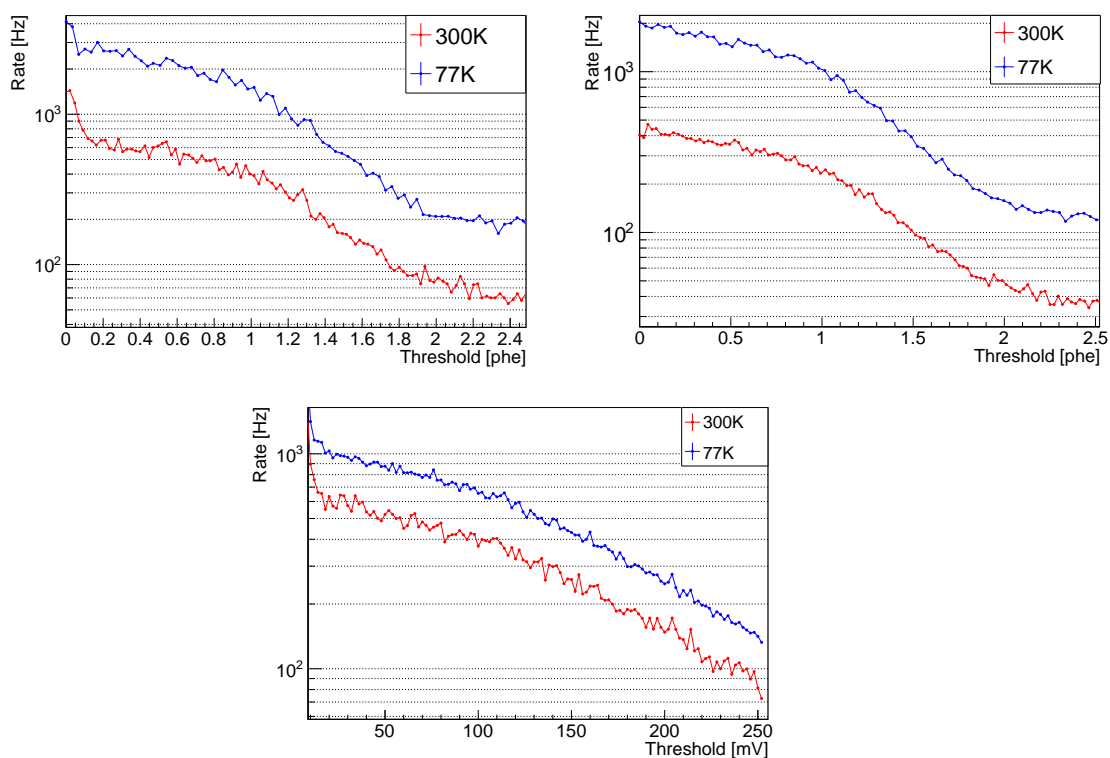


Figure 5.11: Dark count spectra for Hamamatsu R5912 Mod (left up), R5912-02 Mod (right up) and ETL 9357 KFLB (down) at room and cryogenic temperature.

5.1. Tests on PMTs

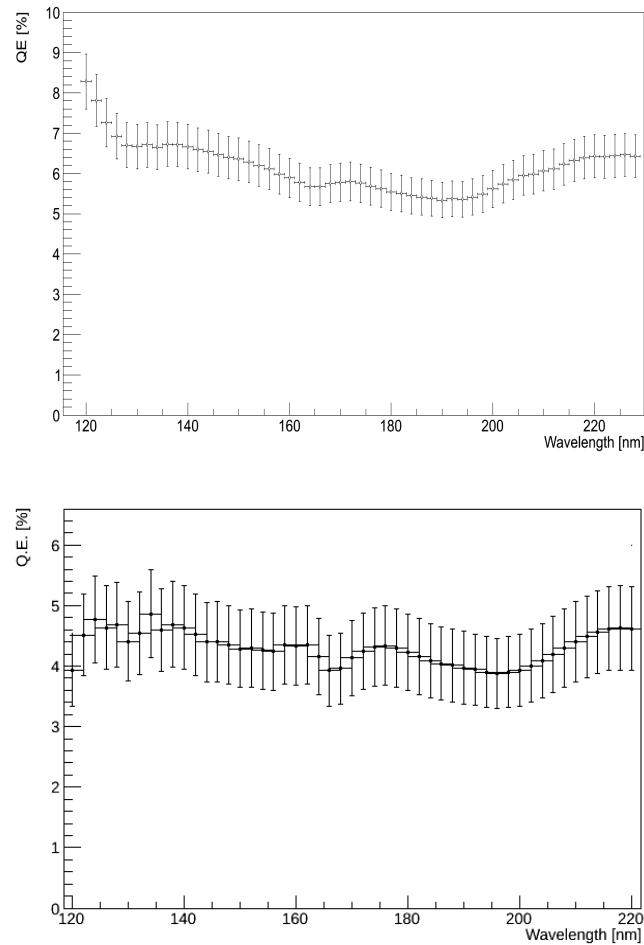


Figure 5.12: Quantum Efficiency for Hamamatsu R5912 (top) and ETL 9357 KFLB (bottom) for incident light wavelength from 120 to 220 nm. PMT windows were coated with TPB.

tial reconstruction capability of the new detector, when using the scintillation light. To better understand this linearity losses, additional dedicated tests were carried out, at room temperature.

A new set of resistors was used, with a total resistance of $6\text{ M}\Omega$, to drive a higher current value in the circuit. The divider design was again the standard one suggested by Hamamatsu: in this configuration the inter-dynode voltage is increased in the latter stages, as recommended to overcome space-charge effects and to recover linearity at high intensity illumination. The same saturation effect as before is observed, almost independently from the current drained by the divider. The linearity of the anode signal depends instead on the applied voltage, getting worse at high power supply values, as shown in Fig. 5.14.

In order to understand where, along the PMT multiplication stage, the amplification problems arose, the signals from the last dynodes (down to 8th electrode) were picked up: gain obtained from the different dynodes, for different values of the applied voltage on cathode, are presented in Fig. 5.15. Saturation effects

5. New light collection system: hardware activity

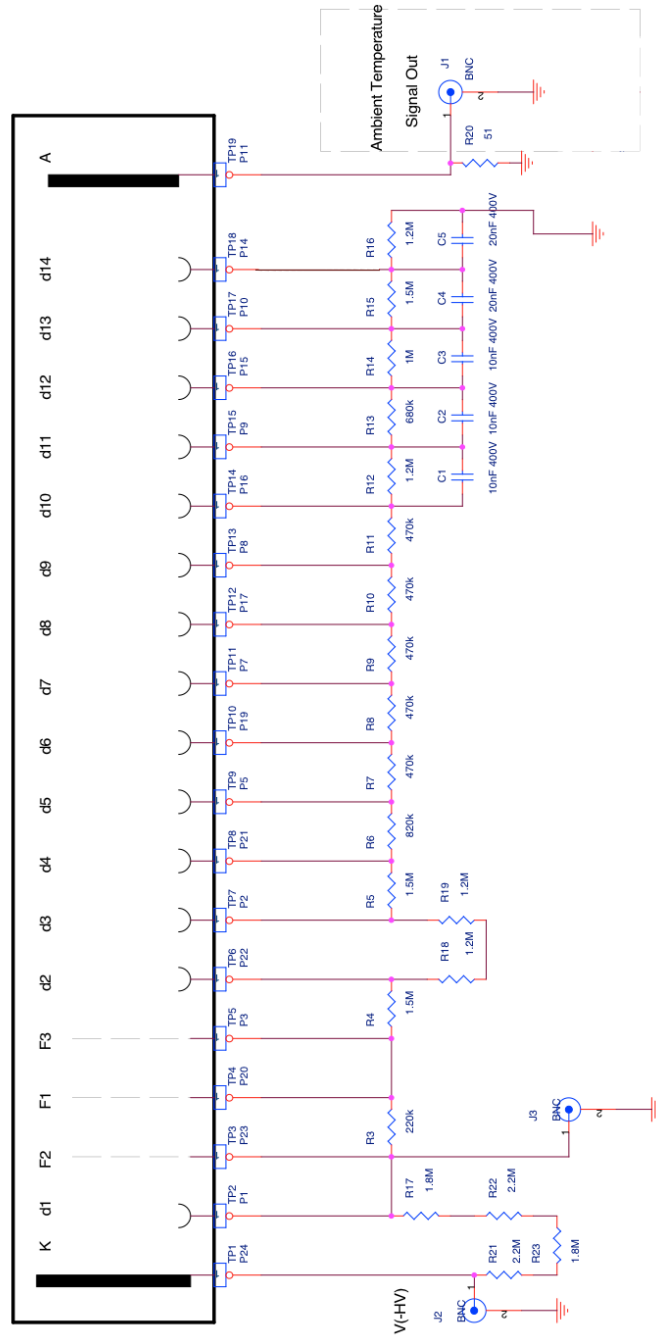


Figure 5.13: Voltage divider used to test the Hamamatsu R5912-02 Mod.

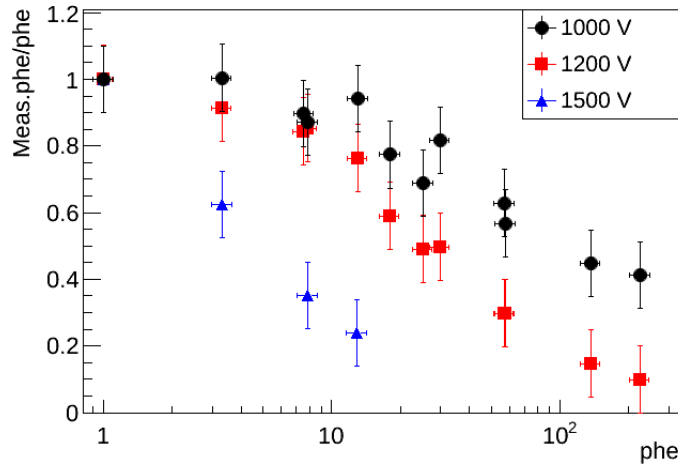


Figure 5.14: Linearity response of Hamamatsu R5912-02 for three different power supply. The anodic signal (Meas.phe) is normalized to the expected phe numbers for the ideal case (phe).

are still present in the dynode signals (see Fig. 5.16) and the behavior reproduces the anodic non-linearity; it can be argued that the saturation problems occur in the first stages of the amplification chain.

As last attempt, the resistors of the base circuit were substituted in order to have the same voltage drop all along the dynode chain, with the exception of the focusing electrodes. In this way the PMT operated with a lower gain (about a factor 10 lower than the same with the standard voltage divider). Any linearity improvement were registered.

On the bases of the described tests, it is possible to affirm that:

- saturation problems are connected to the PMT gain, suggesting induced effects by the dynode chain;
- the cause of the observed linearity loss is not localized in the last part of the amplification stage (above 8th dynode).
- a linearization of the voltage distribution on the whole amplification stage, with the exception of the focusing electrodes, has no positive effects.

The linearity/saturation problem does not seem to be related to the dynode biasing, but it appears connected to the internal design of the amplification stage. The use of this PMT model with 14 dynodes seems to be unsuitable if a high dynamic range of illumination is expected, as in our experiment.

5.1.3 ETL 9357 KFLB

ETL 9357 KFLB is a 12 dynodes photomultiplier. To test this device a different power supply configuration was used: cathode set at fixed negative HV (V=-

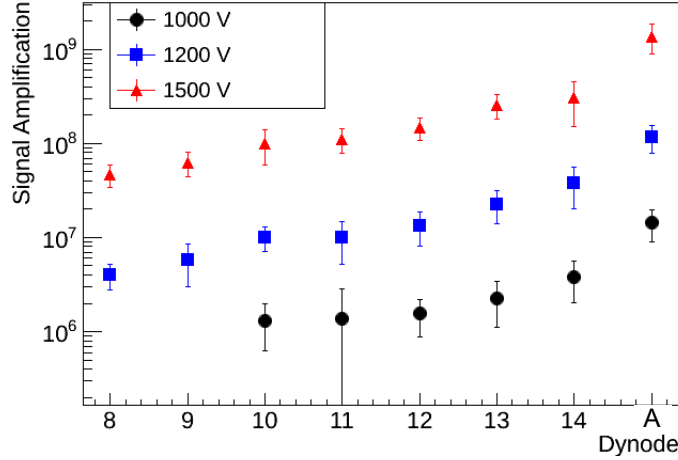


Figure 5.15: Gain of the R5912-02 with the low resistance voltage divider, for signal extracted from anode and last amplification stages (from 8th dynode).

600 V), with first dynode grounded and anode at variable positive HV, as suggested by the manufacturer. The voltage divider used had a total resistance of 13.5 M Ω and it is shown in Fig. 5.17. Measurements at room temperature were carried out with $V = 1350$ V between cathode and anode, obtaining a gain of $\sim 2 \times 10^7$ (see Fig. 5.4).

As shown in Fig. 5.6, ETL 9357 KFLB presents a very good response uniformity, within 10%, in all the region of the photo cathode. For what regards the signal intensity dependence on the Earth magnetic field, it was studied the different behavior between light signals from the centre and the peripheral regions of the PMTs. Going further from PMT axis, signal seems to be less affected by the Earth magnetic field, probably due to the strongest focusing action of the electric field in the edge of the photo cathode with respect to the centre (see Fig. 5.7). Again, the transit time is unaffected by Earth magnetic field, being compatible in all orientation with that measured with the μ -metal, 66.4 ± 2.2 ns (see Fig. 5.8).

Gain reduction, occurring at cryogenic temperature, is evident, being the gain at $T=77$ K $\simeq 35\%$ of that at room temperature (see Fig. 5.4); with an 225 V increase in the voltage drop between anode and cathode the gain of $\sim 2 \times 10^7$ was restored. For what concern the linearity, ETL 9357 KFLB shows a good response, up to 200 phe, both at room and at cryogenic temperature (see Fig. 5.10).

ETL 9357 KFLB linearity was measured taking into account the device charge response only. The PMT presents in fact a very unstable signal shape, without the possibility to obtain a good voltage peak (see Table 5.4). This compromises the possibility of setting good threshold for the dark noise measurements (see Fig. 5.11), and, above all, a precise threshold for the PMT activation in the real experiment. Dark count spectra of 9357 KFLB does not present the single

5.1. Tests on PMTs

	T = 300K	T = 77K
Leading edge (ns)	3.97 ± 0.80	3.98 ± 1.98
Trailing edge (ns)	3.61 ± 1.77	9.67 ± 3.22
FWHM (ns)	4.71 ± 0.98	6.43 ± 3.20

Table 5.4: Leading edge, trailing edge and FWHM of the ETL 9357 KFLB at room and cryogenic temperature, measured in SER condition. All these characteristics presents high instability.

phe bump; the dark rate is lower with respect to these of Hamamatsu PMTs, being lower than 1 kHz for almost all threshold both at room and at cryogenic temperature. As shown in Fig. 5.12, the Q.E. of ETL 9357 KFLB is lower with respect to Hamamatsu PMTs, being Q.E. = $4.7\% \pm 0.7\%$ for LAr light emission peak.

5.1.4 PMT model final choice

Given the results of the tests, Hamamatsu R5912 PMT was chosen. It presents all the characteristics required:

- window of 8" diameter and length fitting the ICARUS mechanical structure;
- peak Q.E. of 25% at 390 nm, resulting in a Q.E. of $7.0\% \pm 0.6\%$ for 128 nm light when coated with TPB;
- photocathode uniformity within 10% till 10 cm from the centre of the window;
- gain of 10^7 with 1450 V and 1600 V applied voltage at T=300 K and T=77 K respectively;
- SER peak clearly visible (peak-to-valley ratio > 2) both in charge and in voltage measurements;
- response linearity up to ~ 400 phe;
- dark count rate lower than 4 kHz for all detection threshold (1.5 kHz at 1 phe) at T=77 K;
- TTS of 1.5 ns.

All the presented tests, both at room and at cryogenic temperature, will be repeated on a pre-series of 20 PMTs, first batch of the full 400 PMTs order, to check the stability of the measurements on a significative sample. On the remaining series production, only the complete set of test at room temperature will be carried out, as a mechanical integrity check at cryogenic temperature will be performed by the manufacturer.

5.2 PMTs induced noise

In the previous phase of the experiment, it was observed on the wires planes a PMT induced noise correlated to the scintillation light produced by the interactions (see Fig. 5.18). However, due to the small number of devices and the absence of cosmic muon background, this did not imply big problems in the reconstruction of event energy or in their classification.

In this new phase the total number of PMTs in the detector will be 5 times higher than in LNGS runs and there will be many light signals for each charge image: the problem could arise more seriously. To find a solution, a proper support was used to put in front of the PMT window a small wire surfaces, to simulate the experimental condition. Tests were done at room temperature, without the use of a small TPC, to easily and rapidly change the mutual configuration between PMT and wires. The used PMT model was the Hamamatsu R5912 Mod, at the nominal gain of 10^7 (1450 V bias voltage). Measures were carried out with the oscilloscope.

A first attempt was done by completely screening the PMT with a Faraday cage, set in contact with the PMT ground: if the HV biased PMT cathode is the cause of the noise, this solution should remove it. However no change in the noise induced by the PMTs on the wire could be noticed (see Fig. 5.19); the same happened if a copper screen, set at different voltages, was placed between the PMT, screened by the Faraday cage, and the wires. It can be deducted that no spurious charge is induced on the wires by PMT cathode and dynode chain.

Reason for the noise must be searched in recovery current of the PMT, that induces, through cable shield, noise on the wires. Common ground does not represent a good screen for high frequency induced signals. In the experiment configuration particular attention has to be used to diversify the grounds, to avoid these effects. However, in order to reduce the effect of the recovery current, an attempt was done by doubling, from 10 to 20 nF, the capacity of the capacitors on the last stages of the PMT (see Fig. 5.3). The noise induced on the wire almost disappeared (see Fig. 5.20). Other tests were performed at CERN, with the PMT mounted into a small LAr-TPC. In front of the device a grid and a wire plane to better simulate the real experimental conditions. The results of our first tests were confirmed.

In the design of the PMT voltage dividers to be mounted in the detector, this behavior is taken into account. A series of capacitors, to obtain 40 nF of total capacitance, will be used. In addition, the dielectric of these capacitors will be C0G, whose characteristics are little affected by temperature variations. The total resistance of this scheme is $\sim 5 \text{ M}\Omega$ (see Fig. 5.21).

5.3 PMT acquisition and calibration system

The input dynamics must permit the recording of the scintillation light fast component pulses and, at the same time, of the single photons arriving from the slow component de-excitation. The ADC sampling frequency should be sufficiently high, in order to allow a time resolution of about 1 ns, with a buffer size long enough to collect all the events occurring during the acquisition windows (~ 1 ms). This possibility is offered, for example, by the CAEN V1730 Waveform Digitizer, housing a 16 Channel 14-bit 500 MS/s Flash ADC with 2 Vpp input dynamics and up to 5.12 MS/c memory size (~ 10 ms).

Timing measurements from each PMT are affected by individual channel delays due to thermal excursion of signal cables, PMT transit-time drift and other effects: to obtain a proper ~ 1 ns timing these delays have to be eliminated. Equalization of single channel can be obtained by analyzing crossing muons or, with more accuracy, by routinely delivering a fast laser pulse to each PMT.

In the T600, the equalization of all the channels will be performed by splitting the signal from a fast laser diode (typical FWHM ~ 30 ps, peak power ~ 1 W) to all the PMTs, set in common STOP, and to a reference fast photodiode, used as START. The system will be made by fused fibre splitters, optical switches and optical patch-cords, in a way similar to the calibration system proposed in [71]. In particular, the system will include a fast laser diode, a $1 \times N$ optical switch and $N=25$, 1×16 , or $N=50$, 1×8 , fused optical splitters, in addition to the necessary optical feed-throughs and patch-cords. To guarantee an optimal and simple injection of the light from the laser source, large core multimode fibers with 100 or 200 μm radius will be used.

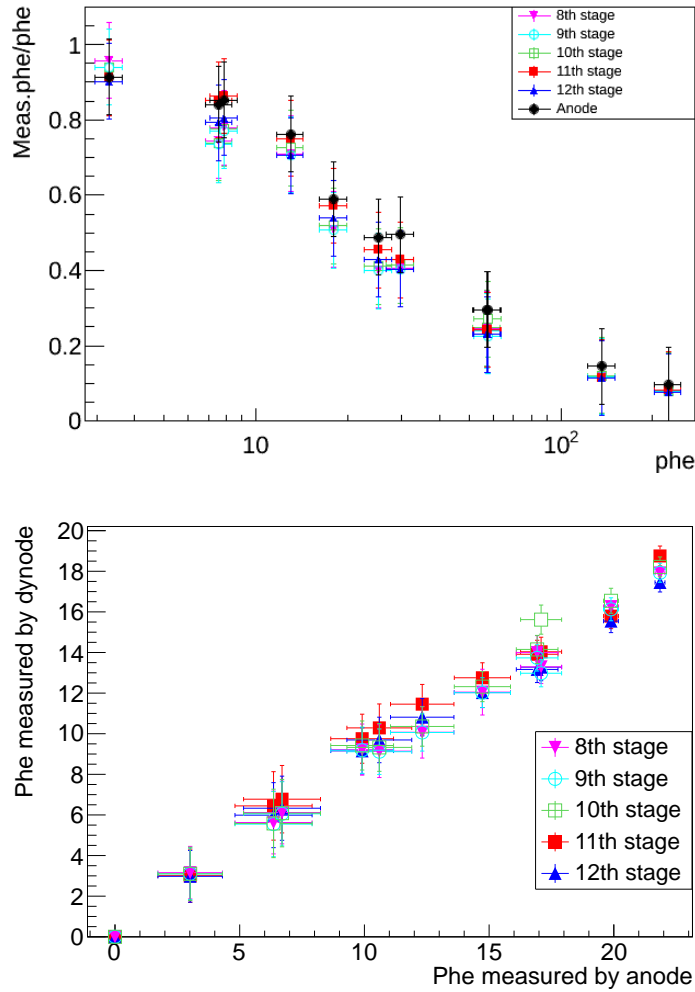


Figure 5.16: Linearity response of Hamamatsu R5912-02 for gain $\sim 10^8$ at the anode. Signals were picked up both from the anode and from the last multiplication electrodes (down to the 8th dynode). Left: Response signals (Meas.phe) are normalized to the expected phe numbers for the ideal case (phe). Right: The relation between dynode signals and the corresponding response at the anode is presented.

5.3. PMT acquisition and calibration system

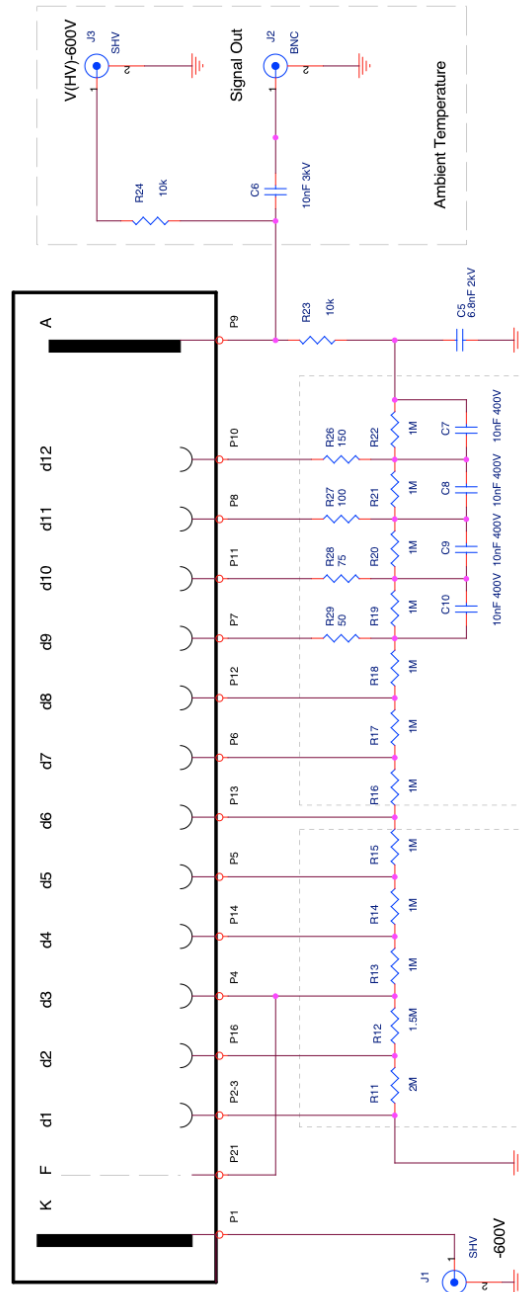


Figure 5.17: Voltage divider used to test the ETL 9357 KFLB.

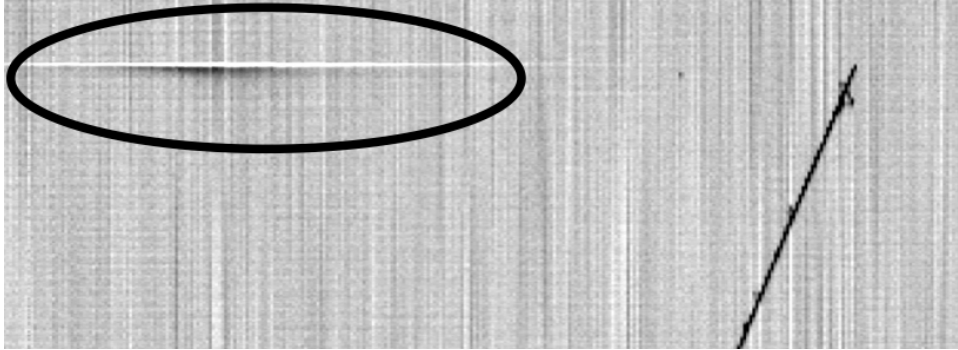


Figure 5.18: Example of noise induced on wires by PMTs in LNGS run of T600 detector.

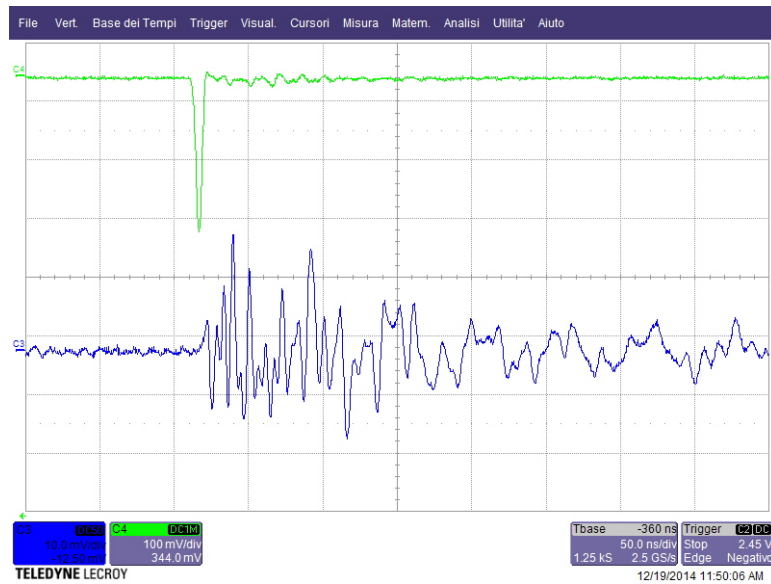


Figure 5.19: Noise signal (blue line) induced on the wire grid by the PMT signal (green line) with the PMT screened by a Faraday cage.

5.3. PMT acquisition and calibration system

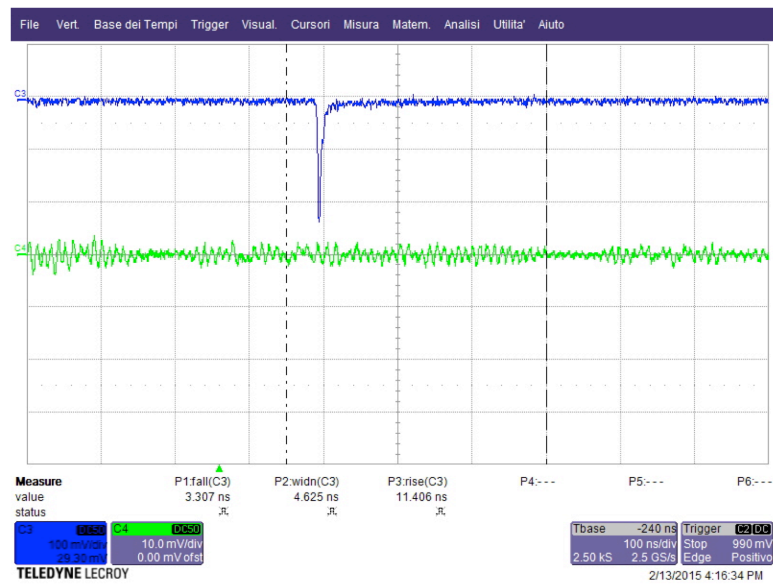


Figure 5.20: Noise signal (green line) induced on the wire grid by the PMT signal (blue line) with the PMT not screened by the Faraday cage but with 20 nF instead of 10 nF capacitor on the voltage divider (see Fig. 5.3).

5. New light collection system: hardware activity

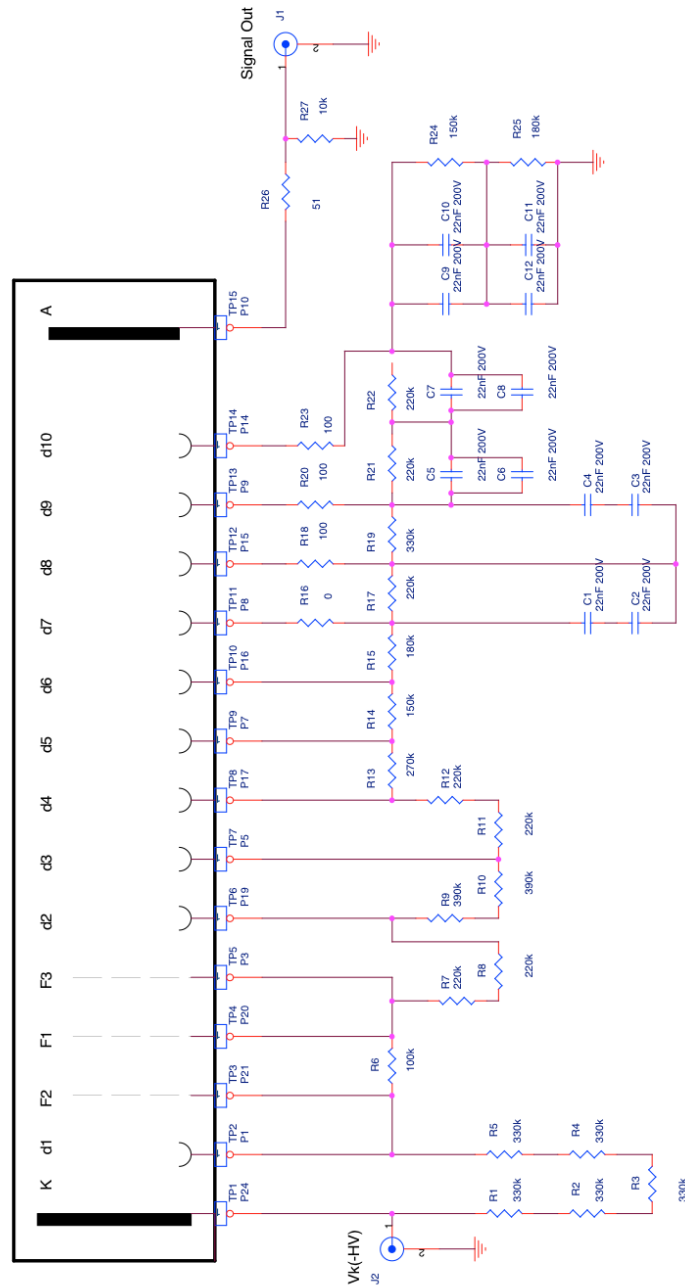


Figure 5.21: Voltage divider to be mounted on the R5912 for the installation in the detector.

ICARUS T600 with magnetic field

After the short baseline experiment at Fermilab, one of the possibility for a further use of the T600 detector could be as a near detector for the Deep Underground Neutrino Experiment (DUNE). It is a proposed long baseline experiment, with a multi-kiloton (~ 40 kton) modular LAr TPC as main far detector, placed deep underground in the Homestake Mine (South Dakota), at 1300 km from the beam source at FNAL [72].

In this hypothesis the T600 should be equipped with an intense magnetic field, in order to obtain a precise particle momentum measurement. Some preliminary simulations have been already produced and will be presented in section 6.1. The presence of the magnetic field will rule out the use of PMTs. A possible solution is the use of Silicon PhotoMultipliers (SiPM); first test carried out on these devices will be showed in section 6.2.

6.1 Magnetic field simulation

A first simulation of a magnetic field for the T600 detector have been performed with the COMSOL Multiphysics[®] software; it is a general-purpose software platform, based on finite elements numerical methods, for modeling and simulating physics-based problems.

To achieve recognition and momentum measurement of charged particles, the best configuration is to have a magnetic field perpendicular both to the beam (x coordinate in the following) and to the drift (y coordinate) direction. The desired intensity of the magnetic field inside the argon volume is ~ 1 T. The purpose of the simulation is to evaluate the uniformity of the field inside the LAr volume and also to have an idea of the intensities of the forces to which the structures are exposed. A Helmholtz coil configuration is proposed, with one or two sets of coils. The first configuration, with a single set of coils is showed in Fig. 6.1.

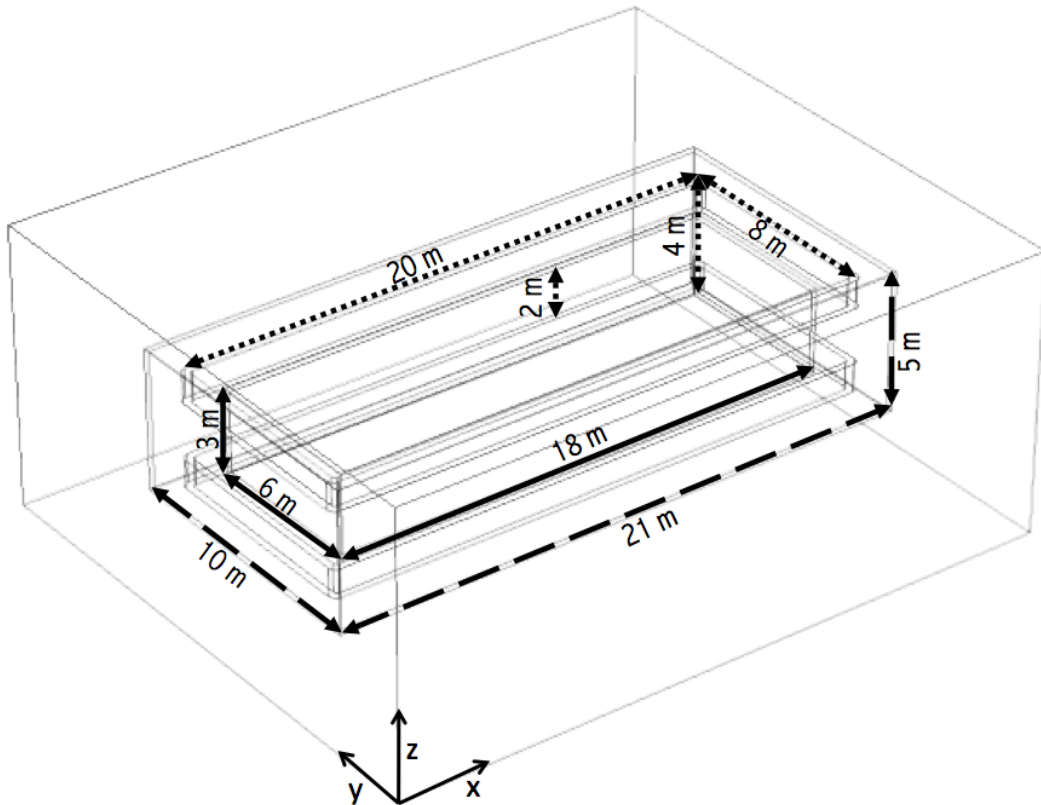


Figure 6.1: Simulation of the configuration with a single set of coils. Full lines refer to the dimension of the active argon volume, dotted lines to the dimension of the coils, while dashed lines to the dimension of the iron yoke.

The simulated geometry is composed by an inner detector, a conductive Helmholtz coils and an iron yoke. The inner detector is simulated as a single parallelepipedal volume, filled with LAr; its dimensions are $3 \times 6 \times 18 \text{ m}^3$, as the whole T600 active volume. The coils are simulated as made of a perfect superconductive material; 400 turns per coil are assumed, with no force between the different turns. The coils have rectangular section ($1 \times 0.25 \text{ m}^2$); the section shape seems not to affect significantly the result of the simulation, so the less computing time consuming geometry is chosen. Coils are 1 m distant from the active volume and, in order to obtain the wanted magnetic field of $\sim 1 \text{ T}$, the current value i is set to 20 kA.

The iron yoke is used to have a contained return path and to significantly lower the magnetic field in the region around the detector. An increase of the field inside the active argon volume is found, as expected. The yoke is simulated as a 20 cm thick shell of soft iron surrounding both the detector and the coils, distant 1 m from the coils in the y direction and 0.5 m in the x and z directions. The thickness of the yoke is not sufficient to contain the magnetic field; in the real experiment a structure with multiple thinner layer will be used.

6.1. Magnetic field simulation

The real joke configuration implies a huge increase of the calculation time, without no effect on the conditions inside the joke, those of interest in this simulation. However, the presence of a huge magnetic field outside the joke will permits the comparison, in terms of field confinement, between the single set of coils configuration described and the one with two set of coils that will be exposed later.

The maps of the absolute value $|B|$ and of the vertical component B_z of the magnetic field, in the planes of symmetry parallel and perpendicular to the ones of the coils, are shown in Fig. 6.2. Mean intensities in the active LAR volume are $|B| = 0.92 \pm 0.12$ T and $B_z = 0.92 \pm 0.12$ T, with a spread of 13%; the vertical component represents almost all the B field.

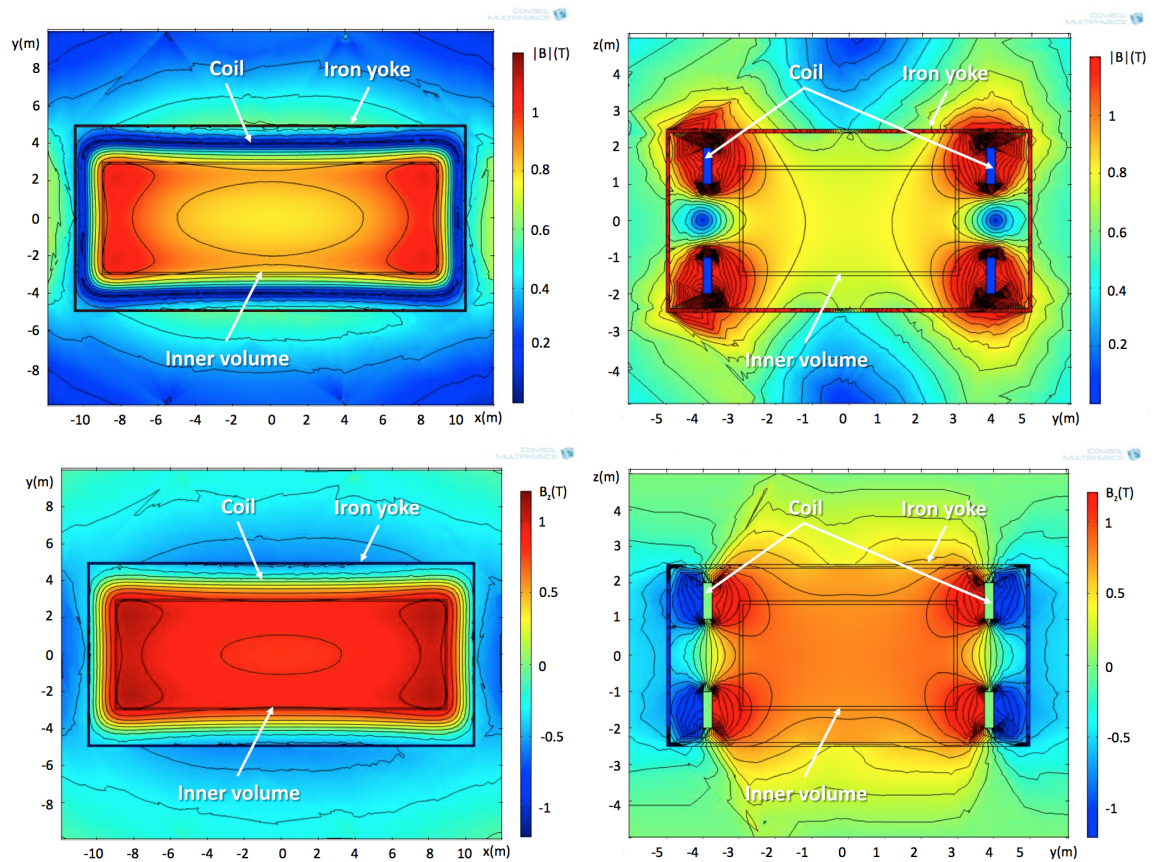


Figure 6.2: Maps of the absolute value $|B|$ (up) and of the vertical component B_z (down) of the magnetic field, in the planes of symmetry parallel (left) and perpendicular (right) to the ones of the coils, in the configuration with a single set of coils. Mean values in the active argon volume are $|B| = 0.92 \pm 0.12$ T and $B_z = 0.92 \pm 0.12$ T, with a spread of 13%.

The forces to which the structures will be exposed are only roughly calculated, to understand if they could become too intense for standard support structure. The calculation is made taking into account the presence of the iron yoke which modifies the force field, both in intensity and in direction. The coils are

assumed to be made by a single conductor: the interactions between different turns are not considered. The evaluation is made, for both short and long sides of the coils, with the Ampere formula $F = (i \cdot B) \cdot L$, where L is the length of the coil segment. As it can be seen in Fig. 6.3, forces on the coils are $\sim 10^7$ N/m, supposed to be manageable with standard support structure. This value can be further reduced if the iron yoke is arranged farther from the coils.

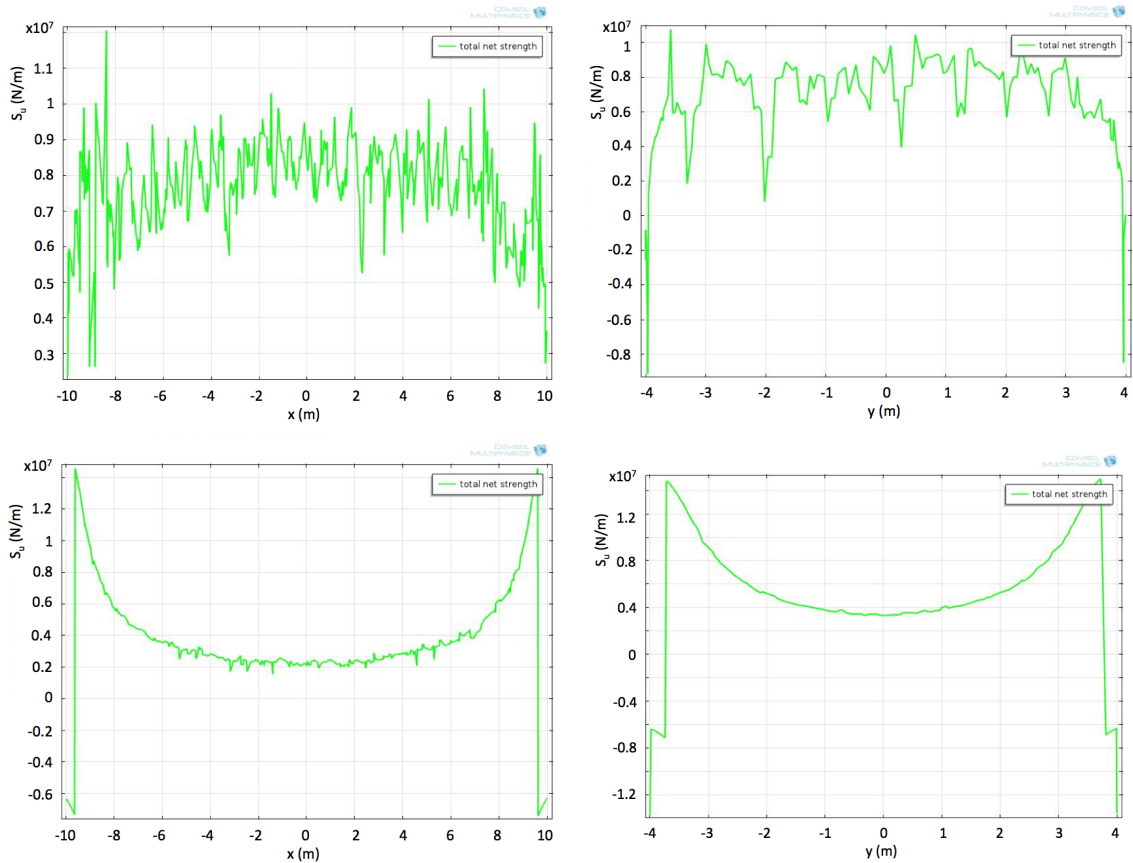


Figure 6.3: Vertical (up) and horizontal (down) component of the force on long (left) and short (right) sides of the coils. Both the components point to the outside, due to the presence of the iron yoke. The irregularity of the force values are due to the finite elements structure of the software.

The second simulated configuration has two separate sets of coils, one for chamber (see Fig. 6.4), with the aim to improve the magnetic field confinement, without losing in field uniformity. In this configuration the electric current flow with opposite direction in the two pairs of coils; the magnetic field has so opposite orientation for the two chambers and about half of the force lines close inside the detector. The active argon is now simulated as two volumes, $3 \times 3 \times 18$ m³ each, separated by 1 m of space, surrounded at 0.5 m by two pairs of coils, with rectangular section and 400 turns per coil; i is again 20 kA. The distance between the coils and the iron yoke, 20 cm thick, is the same as before.

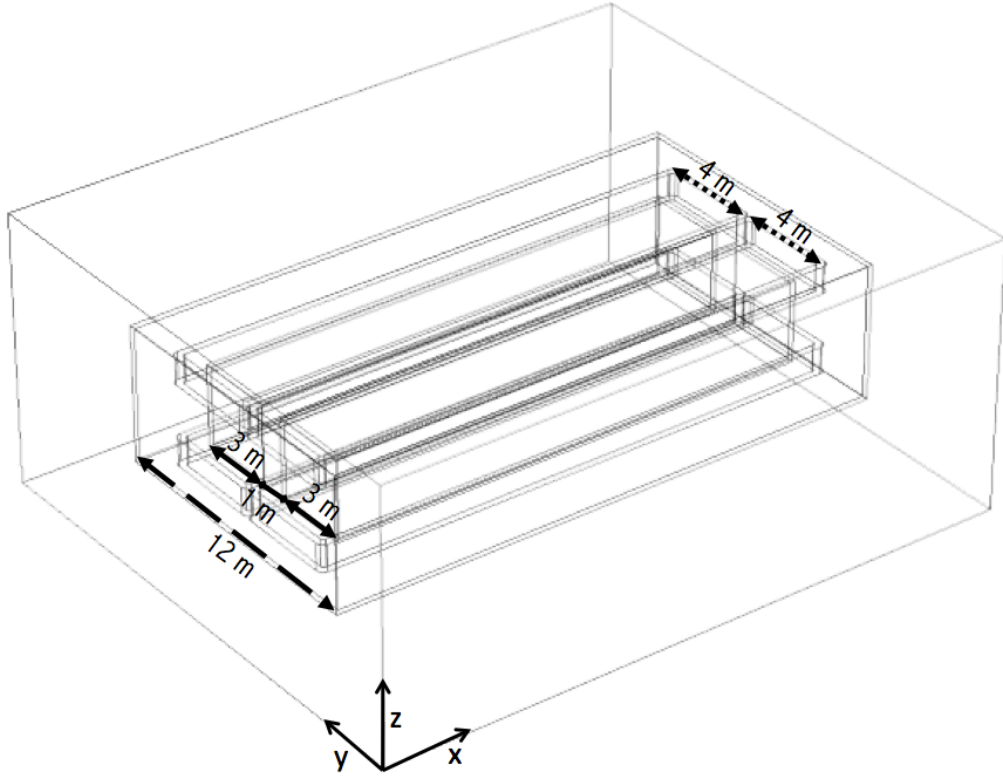


Figure 6.4: Simulation of the configuration with two set of coils. For clarity, only the lengths of components modified with respect to previous configuration are shown. Full lines refer to the dimension of the active argon volume, dotted lines to the dimension of the coils, while dashed lines to the dimension of the iron yoke.

The maps of the vertical component B_z of the magnetic field, in the planes of symmetry parallel and perpendicular to the ones of the coils, are shown in Fig. 6.5. Mean intensities in the active argon volume are $|B| = 1.23 \pm 0.16$ T and $|B_z| = 1.22 \pm 0.15$ T in both chambers, with the spread remaining at the level of 13%. The forces on the structure changes as the field intensity, remaining however manageable with standard support structure.

As it can be seen both in Fig. 6.5 and in more detail in Fig. 6.6, the intensity of the magnetic field outside the iron yoke is drastically reduced with this new configuration.

6.2 Tests on SiPMs

Silicon Photo-Multipliers (SiPMs) are silicon single-photon sensitive devices built from an avalanche photodiode (APD) array on a common Si substrate.

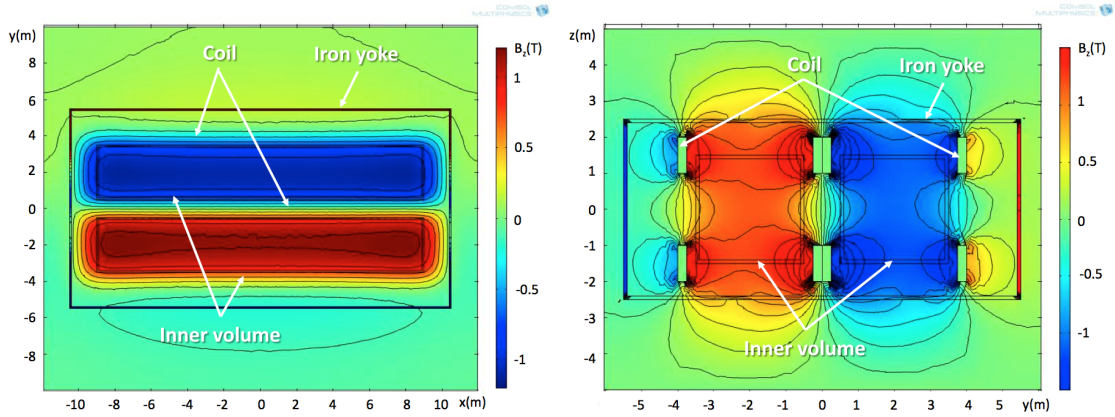


Figure 6.5: Maps of the vertical component B_z of the magnetic field, in the planes of symmetry parallel (left) and perpendicular (right) to the ones of the coils, in the configuration with two sets of coils. Mean intensities in the active argon volume are $|B| = 1.23 \pm 0.16$ T and $|B_z| = 1.22 \pm 0.15$ T in both chambers, with a spread of 13%.

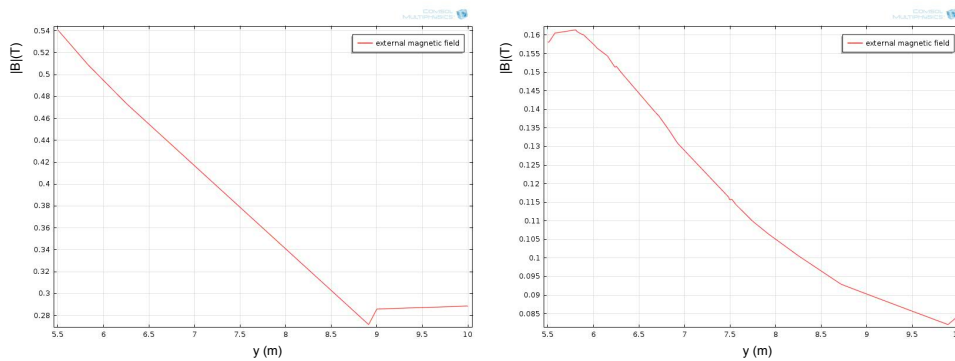


Figure 6.6: Intensity of the magnetic field outside the iron yoke for the configurations with one (left) and two (right) sets of coils. At distance $d=0$ from the yoke the residual field is $|B| = 0.54$ T and $|B| = 0.16$ T respectively, while at $d=2$ m these values decrease to $|B| = 0.38$ T and $|B| = 0.12$ T.

The idea behind this device is the detection of single photon events in sequentially connected Si APDs (see Fig. 6.7). The dimension of each single APD can vary from 10 to 100 μm , and their density can be up to ~ 1000 per mm^2 . Every APD in SiPM operates in Geiger-mode (G-APD) and is coupled with the others by a polysilicon quenching resistor, to stop the avalanche and to re-activate the cell in short time (tens of ns). Although the single devices work in digital/switching mode, the SiPM is almost an analog device because all the micro cells are read in parallel making it possible to generate signals within a dynamic range from a single photon to 1000 photons, from just a single square millimeter area device (for more information on SiPm see [74]).

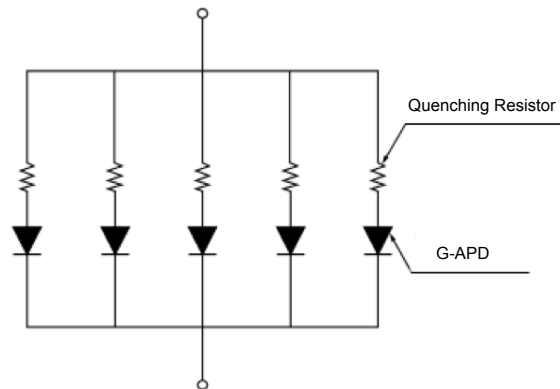


Figure 6.7: Schematic structure of a SiPM.

SiPMs are mostly insensitive to magnetic field, thus being suitable to be deployed in the possible future phase of the experiment. Their main drawback is their small collection surface with respect to the PMTs, in addition to their non sensitivity in the VUV light region, where emission spectrum of the noble gases scintillation are peaked. As for PMTs, a wavelength shifter can be used to overcome this problem [75]; however, SiPMs dedicated to ultraviolet light detection have been recently developed, with Photon Detection Efficiency (PDE) peaked around 200-300 nm, and sensible, with lower PDE, till 130-140 nm.

The performance of two of these new SiPMs, AdvanSiD ASD-NUV-SiPM 3S-P and Hamamatsu 3x3 MM-50UM VUV2, have been tested both at room (300 K) and at liquid nitrogen (77 K) temperature: breakdown voltage, quenching resistance, dark counts rate (DCR), signal shape and its dependence on voltage have been studied as function of temperature. The response of the devices to ultra-violet light have been also studied [73]. The SiPMs under study are both 3x3 mm^2 P-on-N devices, with 3600 square cells ($50 \times 50 \mu\text{m}^2$) each. AdvanSiD SiPM is sensible to the light in the NUV (near ultraviolet) region; Hamamatsu device is made for VUV light detection: in fact it is sensible up to ~ 130 nm.

Devices were lightened by a 405 nm Laser Diode, pulsed with a pulse generator HP 8161A (rate 1 kHz, width 6 ns and variable amplitude), through

a quartz optical fibre of 100 μm core width, single mode and 1 m long. A proper support was used, in order to fix the relative position of the fibre and the SiPM; the SiPM under analysis was placed in front of the fibre, at 1 cm, to obtain a constant enlightenment of the device. To test them at cryogenic temperature, SiPMs were directly immersed in liquid nitrogen, with the same support used before. The fibre and other cables were allowed to pass by a proper feed-through, to preserve darkness conditions and thermal insulation. SiPM waveforms were acquired directly by an oscilloscope Lecroy 104Xi-A, with 8 bit resolution, 1 GHz bandwidth and 5 GS/s acquisition speed, while the DC current responses were measured with a picoammeter Keithley 6487E (see Fig. 6.8). Acquisition was automatized through Labview[®] programs and data were then analyzed with Matlab[®] and ROOT packages.

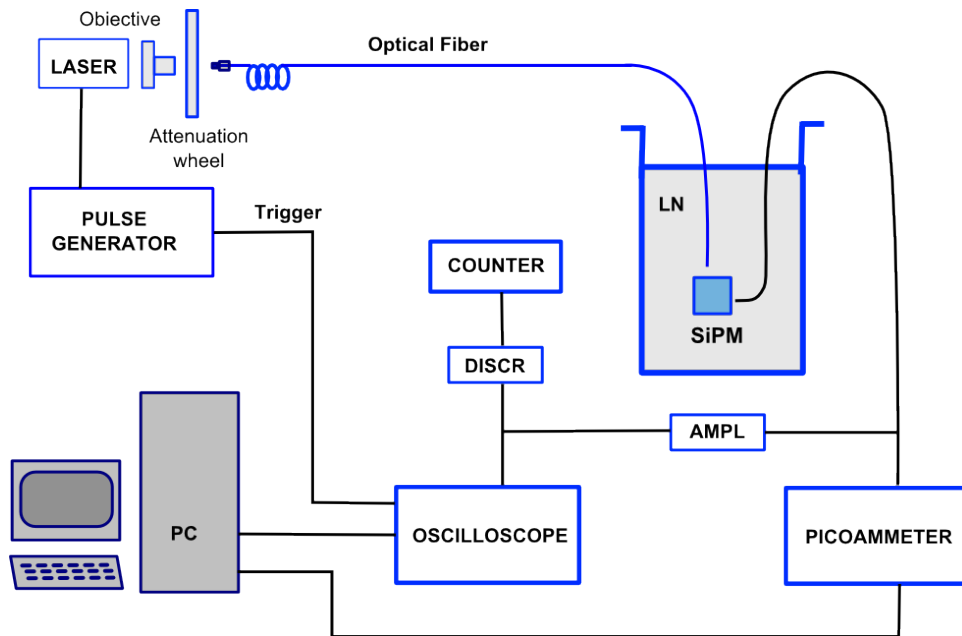


Figure 6.8: Layout of the acquisition system used to test SiPMs in cryogenic environment.

6.2.1 Breakdown voltage

Breakdown voltage (V_{BD}) is a very important parameter of SiPMs and can be measured by reverse biasing the device [76]; it is defined as the voltage at which the second derivative of the logarithm of the I-V curve reaches its maximum value. At room temperature the thermally generated pulses (dark noise) were enough to allow the measurement of the reverse current. Up to V_{BD} , the current increases linearly due to the surface leakage, as expected [77]; above V_{BD} , the breakdown current rises with quadratic dependence on the over-voltage (see Fig. 6.9).

At 77 K the dark noise was not enough to allow short integration time and the measurement had to be done by enlightening the SiPM by means of the fibre, emitting pulses with a constant optical power, controlled with the pulse generator. Up to V_{BD} , reverse current increase again linearly; above V_{BD} , it rises faster with respect to room temperature in dependence on the over-voltage (see Fig. 6.9). The temperature coefficients of V_{BD} are for both devices lower than what declared by the manufacturers (see Tab. 6.1), suggesting a non linear $D=\Delta V_{BD}/\Delta T$ relation at cryogenic temperatures.

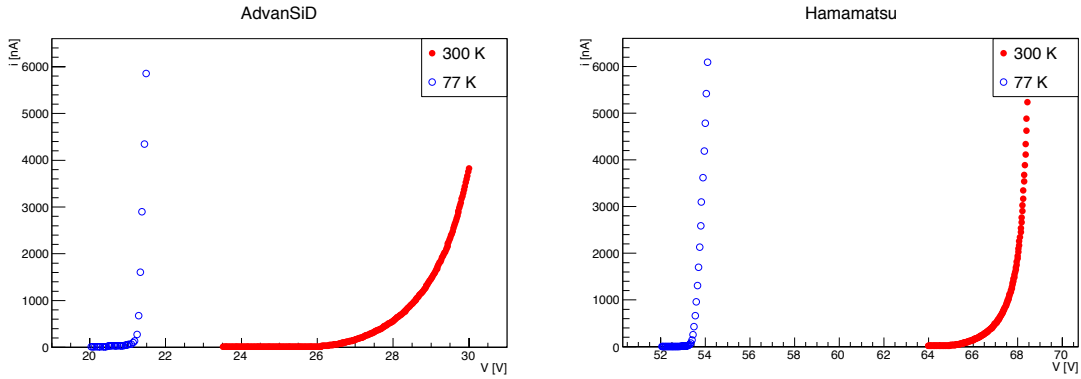


Figure 6.9: I-V reverse characteristic curves for the AdvanSiD (left) and Hamamatsu (right) devices at room and cryogenic temperature.

SiPM	300 K	77 K	D given	D meas.
AdvanSiD	25.7 V	21.2 V	26 mV/K	20 mV/K
Hamamatsu	64.8 V	53.2 V	56 mV/K	52 mV/K

Table 6.1: Breakdown voltage, at room and cryogenic temperature, and $D=\Delta V_{BD}/\Delta T$ relation for the two devices.

6.2.2 Quenching resistance

The quenching resistor (R_q) is the protection resistor of the SiPM; it contributes also to determine the decay time constant of the device. R_q can be measured by directly biasing the SiPM cells array and calculating the inverse of the slope of the I-V curve in the linear region. The retrieved value is then multiplied by the array cell number to obtain the single cell quenching resistance. Quenching resistance values increase by decreasing temperature (see Tab. 6.2), as expected [77]. Hamamatsu device has a quenching resistance about one order of magnitude lower than the AdvanSiD, less dependent on the temperature.

SiPM	300 K	77 K	$\Delta R_q/\Delta T$
AdvanSiD	2.6 M Ω	80 M Ω	-347 k Ω/K
Hamamatsu	321 k Ω	453 k Ω	-600 Ω/K

Table 6.2: Quenching resistance, at room and cryogenic temperature, and trend of R_q with temperature for the two devices.

6.2.3 Over-voltage dependence

By studying the absolute signal amplitude, the trends of the response of SiPMs at different over-voltages V_{OV} ($V_{OV}=V-V_{BD}$) were evaluated. Measurements were performed automatically, using a Matlab[®] routine and the oscilloscope, with SiPMs lightened with pulses of constant optical power. To be insensitive to the correlated noise, the laser signal was used as trigger.

Signal amplitudes, as a function of the over-voltage, seem to be little affected by temperature (see Fig. 6.10): in the Hamamatsu device it decreases a bit at 77 K, while in AdvanSiD one it is constant as function of temperature.

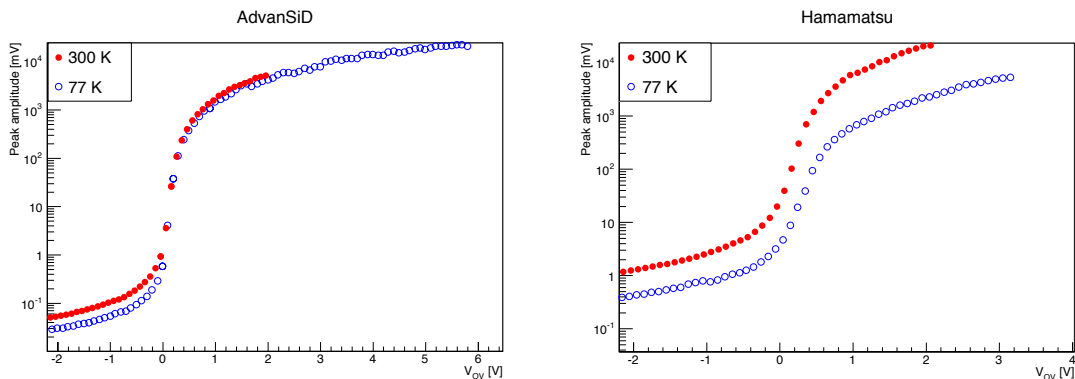


Figure 6.10: Absolute amplitude of the peak as a function of the over-voltage for the AdvanSiD (left) and Hamamatsu (right) devices, at room and cryogenic temperature.

6.2.4 Dark counts rate

The Dark Counts Rate (DCR) is one of the most problematic characteristics of SiPM, when working at room temperature. DCR is mainly due to in-silicon thermally generated pulses and thus it lowers at cryogenic temperatures [76]. Measurements were carried out using a digital counter, with a fixed 0.2 phe threshold.

At 77 K DCR is reduced of ~ 5 orders of magnitude with respect to the value measured at 300 K, reaching order of tens of Hz (see Fig. 6.11). From these measurements, DCR doubles every 13.4 $^\circ$; according to Shokley-Reed-Hall equation [78], for silicon, DCR should double every 8 $^\circ$. Difference can be

due to a non-linear behavior for very low temperature.

DCR has almost the same value for both devices, and the ratio between DCR at room and at cryogenic temperature decreases with the over-voltage.

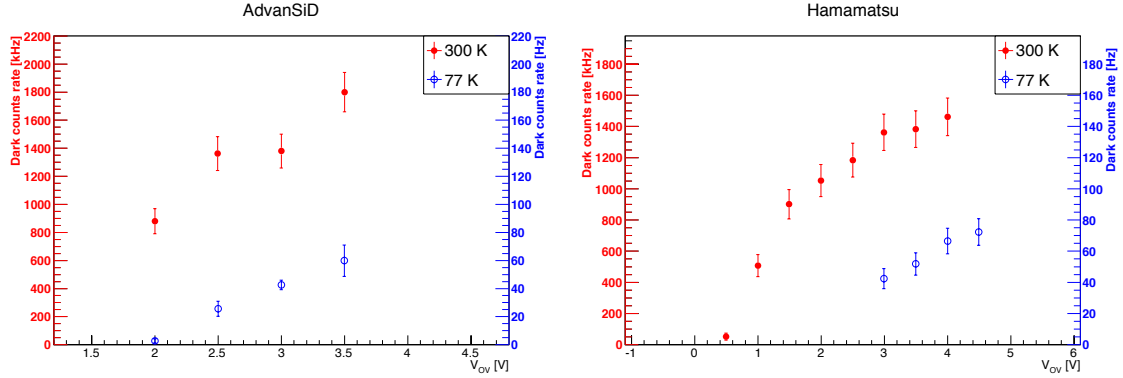


Figure 6.11: DCR at room and cryogenic temperature for the AdvanSiD (left) and Hamamatsu (right) devices. Errors are statistical.

6.2.5 Signal shape

The signal formation in SiPMs can be understood in terms of their equivalent-circuit [79]. Signal results as a linear combination of two pulses (slow and fast) with a common sharp rising edge and exponentially falling slow and fast edges. Leading edge, trailing edge, defined as the time taken by a signal to change from 10% (90%) to 90% (10%) of its peak value, and FWHM were measured for both devices, at room and cryogenic temperature (see Tab. 6.3).

The shape of the signal presents different characteristics according to the operation temperature for the AdvanSiD SiPM. In particular, at LN₂ temperature, the slow time decay component seems to disappear. The reason of this behavior can be found in the considerable increase of R_q , going down with temperature decrease. Instead, for Hamamatsu SiPM the shape, as the R_q , seems to be less affected by temperature (see Fig. 6.12).

6.2.6 SiPM response to VUV light

A different experimental set-up was used to evaluate the response of the SiPMs at VUV light, the same used to measure the Q.E. of PMTs (see section 5.1).

This was a preliminary analysis, to understand which wavelength the devices are sensible to. As expected, the two SiPMs are sensitive to different regions of the light spectrum (see Fig. 6.13): the Hamamatsu SiPM give response from ~ 120 nm, with a peak around 150 nm, while the AdvanSiD one starts to be sensible from ~ 140 nm, and then exhibits a constant increase.

	AdvanSiD	Hamamatsu
Leading edge		
300 K	2.5 ± 0.1 ns	2.0 ± 0.1 ns
77 K	3.5 ± 0.1 ns	3.2 ± 0.1 ns
Trailing edge		
300 K	11.5 ± 0.5 ns	37 ± 1 ns
77 K	8.4 ± 0.5 ns	12.6 ± 0.9 ns
FWHM		
300 K	11.5 ± 0.2 ns	16.2 ± 0.8 ns
77 K	$9.8 \text{ ns} \pm 0.1$	16.5 ± 0.8 ns

Table 6.3: Leading edge, trailing edge, defined as the time taken by a signal to change from 10% (90%) to 90% (10%) of its peak value, and FWHM for the two devices at room and cryogenic temperature.

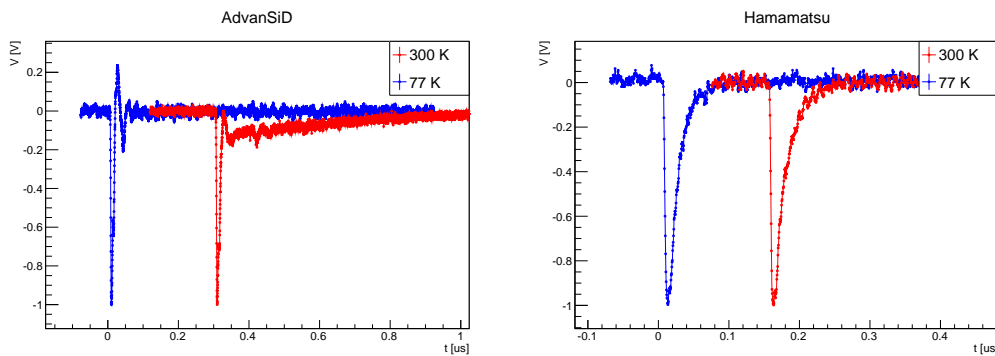


Figure 6.12: Superposition of signals of the AdvanSiD (left) and Hamamatsu (right) devices recorded at 300 K and 77 K: for easier comparison the signals are normalized to their peak value. SiPMs are biased at 1 V of over-voltage.

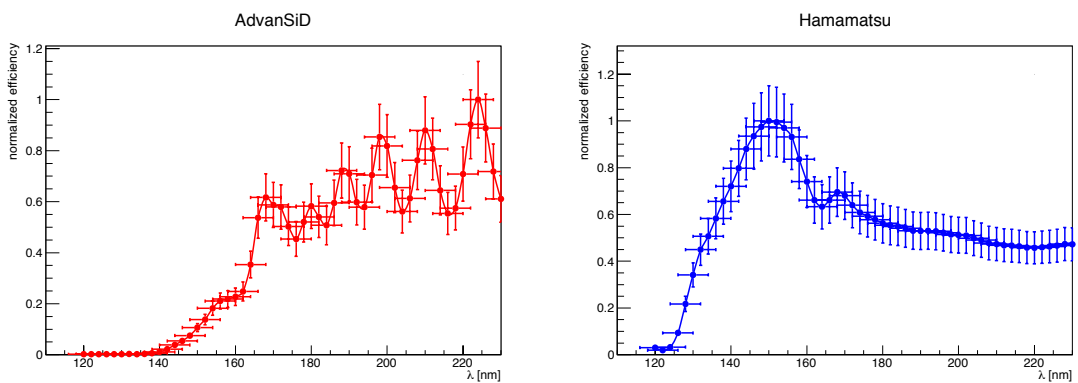


Figure 6.13: Responses of the AdvanSiD (left) and Hamamatsu (right) SiPMs to the VUV light, normalized to their maximum.

Conclusions

The results presented in this work concern three different moments of the ICARUS T600 detector experimental life. I started my Ph.D. work when the detector was installed at Gran Sasso Laboratory and exposed to the CNGS beam, to study primarily the oscillation $\nu_\mu \rightarrow \nu_\tau$, but also $\nu_\mu \rightarrow \nu_e$. In this phase, I was involved in the data analysis: ionizing tracks collected by the detector were visually classified. The first classification allowed to distinguish between:

- muons from the rock, i.e. μ from ν_μ CC interaction with the rock around the detector;
- residual of ν interactions with vertex outside the instrumented volume;
- neutrino interactions:
 - ν_μ CC candidates;
 - ν_e CC candidates;
 - NC candidates.

A more refined analysis was performed on the 2650 collected neutrino events, to identify the electrons from ν_e CC interactions. Seven electrons have been found, in good agreement with the expectation of 8.4 ± 1.1 electron events from conventional sources: the result is so compatible with the absence of a LSND anomaly. ICARUS result strongly limits the window of parameters for the LSND anomaly to a very narrow region with $\Delta m^2 \simeq 0.5 \text{ eV}^2$ and $\sin^2(2\theta) \simeq 0.005$.

To give a definitive answer to the LSND problem, the ICARUS T600 detector will be moved to Fermilab, where it will become the Far Detector of a series of three, for the Short Baseline Neutrino experiment. The detector will be placed at ~ 600 m from the source of a $\sim \text{GeV}$ energy ν_μ ($\bar{\nu}_\mu$) beam, in the ideal position to study the LSND anomaly. Although the T600 is already well fitted to work at Fermilab, some changes are required, in particular for the different location with respect to the LNGS: at FNAL the detector will work at shallow depth, with an high cosmic ray background.

In fact, for each beam events, the detector will collect, during the ~ 1 ms readout window, ~ 10 crossing muons: each track has to be associated to its own light signal, in order to set the right t_0 for the neutrino events. To do this, a new light collection system will be implemented, to localize events along the beam direction. A Monte Carlo simulation has been created to select the best PMT configuration for this purpose. Different event topologies was simulated: electromagnetic showers, crossing cosmic muons and ν_μ CC interaction.

Different PMT layouts were tested, with both 8" and 5" diameter window PMTs. Without changing the existing T600 mechanical structure, it is quite easy to reach a number of PMTs till 90 8" devices; using instead 5" tubes, configuration with almost the same cost and the same cathode coverage were exploited. A configuration with 90 8"-PMTs was chosen: it permits to localize events, simply averaging on PMT signals, with an error smaller than 20 cm in the beam direction, thus allowing to assign the right t_0 to all the collected events. The localization can be further improved refining the algorithm, reaching an error of ~ 5 cm, with almost no events localized with an error greater than 30 cm. Also along the vertical x direction an error smaller than 20 cm can be achieved.

The simulation was also useful for a first definition of the trigger strategy. The idea is to trigger an event if, in a single TPC, a certain number of PMTs has a signal above a certain threshold. Many combinations between PMT signal threshold and PMT majority permit to have a 100% detection efficiency for events with energy above 100 MeV, rejecting ^{39}Ar induced noise.

With the Monte Carlo simulation, an attempt of event classification using the light information was also performed: recognizing the events triggered by the cosmic rays interaction, it would be possible to reduce of a factor ~ 4 the number of events to be analyzed. Three different neural networks were implemented, to identify the three simulated event topologies. Quite promising results were obtained:

- Crossing muons network: trained with 10k cosmic muons as signal, 5k e.m. showers and 5k ν_μ CC interactions as background. Setting 0.5 as threshold value, bad identified muons, i.e. with result < 0.5 , are $\sim 4\%$, while misidentified background, i.e. with result > 0.5 , is $\sim 7\%$.
- E.m. showers network: trained with 10k e.m. showers as signal, 5k crossing muons and 5k ν_μ CC interactions as background. Setting 0.5 as threshold value, bad identified e.m. showers, i.e. with result < 0.5 , are $\sim 11\%$, while misidentified background, i.e. with result > 0.5 , is $\sim 19\%$.
- ν_μ CC interactions network: trained with 10k ν_μ CC interactions as signal, 5k crossing muons and 5k e.m. showers as background. Setting 0.5 as threshold value, bad identified ν_μ CC interactions, i.e. with result < 0.5 , are $\sim 19\%$, while misidentified background, i.e. with result > 0.5 , is $\sim 23\%$.

Using the networks in sequence on each event, a better identification of crossing muons can be obtained: defining a muon as an event with a result >0.5 for the muons network, <0.4 for the e.m. showers network and <0.25 for the ν_μ CC network, a misidentification of $\sim 2\%$ is obtained.

Once selected the PMT configuration, many tests were performed to choose the best PMT model, between different 8 inches diameter ones. Three different models were tested: Hamamatsu R5912 and R5912-02, and ETL 9357 KFLB, both at room temperature and immersed in a cryogenic bath (liquid nitrogen, $T=77$ K), to simulate the real experimental condition. Photocathode uniformity, quantum efficiency, when coated with TPB, for 128 nm liquid argon scintillation light, signal shape stability, transit time and transit time spread, trends of gain, linearity and dark count rate with temperature were studied. From test results, Hamamatsu R5912 PMT was selected. Its characteristics resulted to be optimal for its use in the experiment:

- window of 8" diameter and length fitting the ICARUS mechanical structure;
- peak Q.E. of 25% at 390 nm, resulting in a Q.E. of $7.0\% \pm 0.6\%$ for 128 nm light when coated with TPB;
- photocathode uniformity within 10% till 10 cm from the centre of the window;
- gain of $\sim 10^7$ with 1450 V and 1600 V of applied voltage at $T=300$ K and $T=77$ K respectively;
- SER peak clearly visible (peak-to-valley ratio >2) both in charge and in voltage measurements;
- response linearity up to ~ 400 phe;
- dark count rate lower than 4 kHz for all detection threshold (1.5 kHz at 1 phe) at $T=77$ K;
- TTS of 1.5 ns.

R5912-02, on the contrary, is linear only up to tens of phe, while 9357 KFLB shows a huge signal shape instability. Tests were carried on also to reduce the noise induced by the PMTs on the wire plane: a new PMT base configuration was designed to reduce at a minimum level this kind of inconvenience.

The choice of the PMTs as light detection devices is forced by the lack of other devices able to collect light in large area detector. However, PMTs present the disadvantage of not to work in presence of an intense magnetic field. This could be a problem for the proposed far future experiment DUNE, where the ICARUS T600 detector could be involved; in this hypothesis the use of magnetic field for a precise particle momentum measurements is forecast.

A first simulation was performed to study two possible configurations of the magnetic field, with one or two sets of Helmoz coils surrounding the detector. For both the configurations, a magnetic field of ~ 1 T can be obtained, with a spread of 13%. The configuration with two sets of coils, one for each module, permits a better confinement of the magnetic field, with same magnetic field spread.

Also tests on new light collection devices, the Silicon Photo-Multipliers (SiPM), were performed. These detectors are not sensible to the magnetic field, but they present some drawbacks, as small area, insensitivity to the VUV light and so on. Measurements of breakdown voltage, quenching resistance, signal dependence on the over-voltage and signal shape, dark count rate and response to VUV light were performed for two 3×3 mm³ area devices.

To summarize, I carried out both hardware and software activities related to the ICARUS T600 detector. In particular, I focused my work on the light detection system to be used in the SBN experiment, whose implementation represents the most important activities of the detector refurbishing. The simulations and the tests performed will permit to exploit the LAr scintillation light for the rejection of the cosmic background and a first event classification, making it possible an efficient data analysis.

Bibliography

- [1] Fundamentals of neutrino physics and astrophysics - C.Giunti, C.W.Kim (2007).
- [2] B. Pontecorvo, Sov. Phys. JETP 6, 429 (1958). Sov. Phys JETP 7, 172 (1958).
- [3] S. L. Glashow, Nucl. Phys. 22, 579 (1961).
- [4] S. Weinberg, Phys. Rev. Lett. 19, 1264 (1967).
- [5] A. Salam, Proc. of the 8th Nobel Symposium on Elementary particle theory, relativistic groups and analyticity, Stockholm, Sweden, 1968, edited by N. Svartholm, p.367-377, (1969).
- [6] S. M. Bilenky and B. Pontecorvo, Sov. J. Nucl. Phys., 24, 316–319 (1976). S. M. Bilenky and B. Pontecorvo, Phys. Rep., 41, 225 (1978). S. M. Bilenky and B. Pontecorvo, Nuovo Cim. Lett., 17, 569 (1976).
- [7] S. Eliezer and A. R. Swift, Nucl. Phys., B105, 45 (1976).
- [8] H. Fritzsch and P. Minkowski, Phys. Lett., B62, 72 (1976).
- [9] L. Wolfenstein, Phys. Rev. D17, 2369 (1978).
- [10] S. P. Mikheev and A. Y. Smirnov, Nuovo Cim. C9, 17 (1986).
- [11] Particle Data Group, updated May 2014 by Nakamura, K. and others.
- [12] <http://hitoshi.berkeley.edu/neutrino/>
- [13] F. Capozzi, et al., Phys. Rev. D 89, 093018 (2014).
- [14] ALEPH, DELPHI, L3, OPAL, and SLD Collaborations, and LEP Electroweak Working Group, and SLD Electroweak Group, and SLD Heavy Flavour Group, Phys. Reports 427, 257 (2006).
- [15] N. Said et al., Phys.Rev. D88, 023513 (2013).

- [16] C. Athanassopoulos et al. (LSND Collaboration), Nucl. Instrum. and Meth. A, 388, 149 (1997).
- [17] A. Aguilar et al. (LSND Collaboration), Phys. Rev. D 64, 112007 (2001).
- [18] G. Drexlin et al. (KARMEN Collaboration), Nucl. Instrum. and Meth. A, 289, 490 (1990).
- [19] B. Armbruster et al. (KARMEN Collaboration), Phys.Rev. D65, 112001 (2002).
- [20] A. Aguilar-Arevalo et al. (MiniBooNE Collaboration), Nucl. Instr. and Meth. A, 599, 28 (2009).
- [21] A. Aguilar-Arevalo et al. (MiniBooNE Collaboration), Phys.Rev.Lett. 102, 101802 (2009).
- [22] A. Aguilar-Arevalo et al. (MiniBooNE Collaboration), Phys.Rev.Lett. 105, 181801 (2010).
- [23] W. Hampel et al. (GALLEX Collaboration), Phys.Lett. B420, 114 (1998).
- [24] J. Abdurashitov et al. (SAGE Collaboration), Phys.Rev. C59, 2246 (1999).
- [25] C. Giunti and M. Laveder, Phys.Rev. C83, 065504 (2011).
- [26] K. Nakamura et al. (Particle Data Group), J.Phys.G G37, 075021 (2010).
- [27] T. Mueller et al., Phys.Rev. C83, 054615 (2011).
- [28] G. Mention et al., Phys.Rev. D83, 073006 (2011).
- [29] Gariazzo, S. et al., Light sterile neutrinos, arXiv:1507.08204v1.
- [30] F.J. Hasert et al., Phys. Lett. B46, 121 (1973); Phys. Lett. B46, 138 (1973).
- [31] C. Rubbia, The liquid-argon time projection chamber: a new concept for neutrino detector,CERN-EP-77-08 (1977).
- [32] P. Benetti et al. (ICARUS Collaboration), Nucl. Instr. and Meth. A, 332, 395 (1993).
- [33] P. Cennini et al. (ICARUS Collaboration), Nucl. Instr. and Meth. A, 345, 230 (1994).
- [34] F. Arneodo et al. (ICARUS Collaboration), Nucl. Instr. and Meth. A, 449, 36 (2000).

BIBLIOGRAPHY

- [35] P. Cennini et al. (ICARUS Collaboration), Nucl. Instr. and Meth. A, 432, 240 (1999).
- [36] F. Arneodo et al. (ICARUS Collaboration), Nucl. Instr. and Meth. A, 498, 293 (2003).
- [37] C. Rubbia et al. (ICARUS Collaboration), JINST 6 P07011 (2011).
- [38] M. Antonello et al. (ICARUS Collaboration), JINST 9 P08003 (2014).
- [39] M. Antonello et al. (ICARUS Collaboration), JINST 9 P12006 (2014).
- [40] S. Amoruso et al. (ICARUS Collaboration), Nucl. Instr. and Meth. A, 523, 275 (2004).
- [41] A. Zani, Advances in High Energy Physics, 2014, 205107, (2014).
- [42] A. Ankowski et al. (ICARUS Collaboration), Nucl. Instr. and Meth. A, 556, 149-157 (2006).
- [43] P. Benetti et al. (ICARUS Collaboration), Nucl. Instr. and Meth. A, 505, 89 (2003).
- [44] G. Aquistapace et al., CERN 98-02., INFN/AE-89-05 (1998).
- [45] R. Bailey et al., CERN-sl799-034 (DI), INFN/AE-99/05 Addendum (1999).
- [46] E. Gschwendtner et al., CERN-ATS-2010-153 (2010).
- [47] A. Cesana et al., Status report of the 2010-11 CNGS data processing, Tech. Rep. ICARUS-TM 12-06 (2012).
- [48] F. Boffelli et al., Advances in 2010-12 CNGS data processing and preliminary results, Tech. Rep. ICARUS-TM 13-04 (2013).
- [49] F. Boffelli v, Final update of 2010-12 CNGS data processing, Tech. Rep. ICARUS-TM 15-0X (2015).
- [50] S. Amerio et al. (ICARUS Collaboration), Nucl. Instr. and Meth. A, 527, 329 (2004).
- [51] M. Antonello et al. (ICARUS Collaboration), Advances in High Energy Physics, 260820 (2013).
- [52] M. Antonello et al. (ICARUS Collaboration), Eur. Phys. J. C 73, 2345 (2013).
- [53] M. Antonello et al. (ICARUS Collaboration), Eur. Phys. J. C 73, 2599 (2013).

-
- [54] F. Capozzi et al., Phys. Rev. D 89, 093018 (2014).
- [55] J. Beringer et al. (Particle Data Group), Phys. Rev. D86, 010001 (2012).
- [56] G.J. Feldman and R.D. Cousins, Phys. Rev. D57, 3973 (1998).
- [57] N. Agafonova et al. (OPERA Collaboration), New J. Phys.13, 053051 (2011)
- [58] C. Rubbia, for the ICARUS Collaboration, Using the beam bunch-structure with the T600 detector, internal SBN report (2014).
- [59] R. Acciari et al., A Proposal for a Three Detector Short-Baseline Neutrino Oscillation Program in the Fermilab Booster Neutrino Beam, arXiv:1503.01520.
- [60] S. Kubota et al., Phys. Rev. B , 20, 3486 (1979).
- [61] T. Doke et al., Nucl. Instr. and Meth. A, 291, 617 (1990).
- [62] M. Suzuki et al., Nucl. Instr. and Meth. A, 327, 67 (1993).
- [63] S. Kubota et al., 1978, Phys. Rev. B , 17, 2762 (1978).
- [64] C. Amsler et al., JINST, 3, P02001 (2008).
- [65] P. Benetti et al., Nucl. Instr. and Meth. A, 574, 83 (2007).
- [66] M. Antonello et al. (ICARUS Collaboration), Nucl. Instr. and Meth. A, 516, 348–363 (2004).
- [67] A. Aguilar-Arevalo et al. (MiniBooNE Collaboration), Phys. Rev. D 79, 072002 (2009).
- [68] A. Falcone et al., Nucl. Instr. and Meth. A, 787, 55-58 (2015).
- [69] P. Agnes et al., JINST, 9, C03009 (2014).
- [70] H.O. Meyer, Dark Rate of a Photomultiplier at Cryogenic Temperatures, arXiv:0805.0771v1.
- [71] M. Bonesini et al., TIPP 2014, PoS 263.
- [72] J. Huber and K. Jepsen, "The dawn of DUNE", Symmetry Magazine, March 2015.
- [73] A. Falcone et al., Nucl. Instr. and Meth. A, 787, 216-219 (2015).
- [74] D. Renker, Nucl. Instr. and Meth. A, 567, 48-56 (2006).
- [75] N. Yahlali et al., JINST, 8, C01003 (2013).

BIBLIOGRAPHY

- [76] D. Renker and E. Lorenz, *JINST*, 4, P04004 (2009).
- [77] G. Collazuol et al., *Nucl. Instrum. and Meth. A*, 628, 389–392 (2011).
- [78] S. Sze and K. Ng, *Physics of Semiconductor Devices*, 3rd Edition, Wiley-Interscience (2006).
- [79] F. Corsi et al., *Nucl. Instrum. and Meth. A* 527, 416–418 (2007).

ISBN: 978-88-95767-89-5



9 788895 767895